

THESIS FOR THE DEGREE OF DOCTOR OF PHILOSOPHY

Electrode Degradation in Proton Exchange Membrane Fuel Cells

LINNÉA STRANDBERG

Department of Physics
CHALMERS UNIVERSITY OF TECHNOLOGY
Gothenburg, Sweden, 2025

Electrode Degradation in Proton Exchange Membrane Fuel Cells

LINNÉA STRANDBERG
ISBN 978-91-8103-190-4

© LINNÉA STRANDBERG, 2025

Doktorsavhandlingar vid Chalmers tekniska högskola
Ny serie nr 5648.
ISSN 0346-718X

Department of Physics
Division of Chemical Physics
Chalmers University of Technology
SE-412 96 Göteborg,
Sweden
Telephone: +46(0)31 772 1000

Cover:

Artistic illustration depicting the degradation of platinum nanoparticles on a carbon support.

Printed by Chalmers Digitaltryck,
Gothenburg, Sweden 2025.

“Research is what I’m doing when I don’t know what I’m doing.”
- *Wernher von Braun*

Electrode Degradation in Proton Exchange Membrane Fuel Cells

LINNÉA STRANDBERG

*Department of Physics
Chalmers University of Technology*

Abstract

To mitigate the climate crisis and reduce carbon emissions from sectors such as transport and energy, hydrogen has been proposed to be used as an environmentally friendly alternative energy carrier. Proton exchange membrane fuel cells (PEMFCs), which are well suited as power sources for several types of vehicles, use hydrogen as a fuel to create electricity with the only by-products being water and heat. However, for successful commercialisation of PEMFCs, some aspects need to be improved. Lifetime, in particular, is a limiting factor due to harsh operation conditions. To improve lifetime, the mechanisms by which the materials in PEMFCs degrade must first be better understood.

In this thesis, I investigate the behaviour and degradation of platinum (Pt) thin films and Pt/carbon-based PEMFC electrodes under various conditions in both half-cell setups and single-cell PEMFCs. Part of the work concerns the behaviour of Pt thin films in acidic and alkaline environments studied using electrochemical quartz crystal microbalance (EQCM) to measure the mass changes of Pt during electrochemical cycling and assess dissolution rates. Additionally, I present three studies on the feasibility of implementing identical location (IL) electron microscopy to follow cathode catalyst degradation under different operating conditions. These studies demonstrate how IL electron microscopy can be used to distinguish between various types of degradation phenomena during realistic operation conditions, opening up new possibilities for further research on the behaviour of catalyst layers during application relevant conditions. Finally, I present a study on the degradation of membrane electrode assemblies (MEAs) during voltage cycling at intermediate temperatures up to 120 °C. This study investigates how elevated temperatures impact the ageing of catalyst layers, motivated by the increasing demand for PEMFC applications that require a broader operational temperature range. Together, these studies explore different aspects of catalyst degradation, introduce new methods for tracking degradation under application-relevant conditions, and enhance our understanding of the performance of current state-of-the-art catalyst materials under new operational conditions.

Keywords: Fuel cells, Platinum stability, Catalyst degradation, Membrane electrode assembly, Identical location electron microscopy, Electrochemical quartz crystal microbalance, Accelerated stress test, Intermediate temperature operation.

List of Publications

Appended publications

This thesis is based on the following publications:

Paper I

V. Shokhen*, **L. Strandberg***, M. Skoglundh and B. Wickman
“Impact of Accelerated Stress Tests on the Cathodic Catalytic Layer in a Proton Exchange Membrane (PEM) Fuel Cell Studied by Identical Location Scanning Electron Microscopy”
ACS Applied Energy Materials
vol. 5, no. 9, pp. 11200–11212, 2022
*equal contribution

Paper II

L. Strandberg, V. Shokhen, M. Luneau, G. Lindbergh, C. Lagergren and B. Wickman
“Comparison of Oxygen Adsorption and Platinum Dissolution in Acid and Alkaline Solutions Using Electrochemical Quartz Crystal Microbalance”
ChemElectroChem
vol. 9, no. 22, p. e202201030, 2022

Paper III

V. Shokhen*, **L. Strandberg***, M. Skoglundh and B. Wickman
“Fuel Cell Electrode Degradation Followed by Identical Location Transmission Microscopy”
Journal of Materials Chemistry A
vol. 11, no. 39, pp. 21029–21035, 2023
*equal contribution

Paper IV

L. Strandberg*, V. Shokhen*, M. Skoglundh and B. Wickman
“Carbon Support Corrosion in PEMFC Followed by Identical Location
Electron Microscopy”

ACS Catalysis

vol. 14, no. 11, pp. 8494–8504, 2024

*equal contribution

Paper V

L. Strandberg, G. Toth, G. Göransson, V. Shokhen, and B. Wickman
“PEMFC Catalyst Layer Degradation at Intermediate Temperatures (80,
100, and 120 °C)”

Under Review

Other publications

The following publications were published during my PhD studies. However, they are not included in this thesis as their contents are not directly related to the thesis.

- [a] M. Luneau, **L. Strandberg**, G. Montserrat-Sisó, V. Shokhen, R. Mohan, H. Grönbeck, B. Wickman
“Fundamental insight into enhanced activity of Pd/CeO₂ thin films in hydrogen oxidation reaction in alkaline media”
Journal of Materials Chemistry A
vol. 11, no. 30, pp. 16370-16382, 2023
- [b] V. Roth, M. Valter-Lithander, **L. Strandberg**, M.R. Bilesan, J. Järlebark, J. Jamroz, B. Wickman
“On the Mechanism and Energetics of Electrochemical Alloy Formation Between Mercury and Platinum for Mercury Removal from Aqueous Solutions”
Electrochimica Acta
vol. 507, p. 145137, 2024
- [c] B. Lönn, **L. Strandberg**, V. Roth, M. Luneau, B. Wickman
“Fuel Cell Catalyst Layers with Platinum Nanoparticles Synthesized by Sputtering onto Liquid Substrates”
ACS Omega
vol. 9, no. 43, pp. 43725–43733, 2024

Author Contributions

Paper I

I performed part of the electrochemical measurements, SEM imaging, and analysis. I contributed to preparing the first draft of the manuscript and finalised the manuscript together with the co-authors.

Paper II

I designed the experiment, prepared the samples, performed the EQCM measurements and analysed the data. I prepared the first draft of the manuscript and finalised the manuscript together with the co-authors.

Paper III

I contributed to developing the methodology and preparing the samples. I performed parts of the TEM imaging and the corresponding image analysis. I performed parts of the electrochemical characterisation and analysis. I contributed to preparing the first draft of the manuscript and finalised the manuscript together with the co-authors.

Paper IV

I contributed to developing the methodology and preparing the samples. I performed the SEM imaging and the corresponding data analysis, I performed part of the electrochemical measurements and the corresponding analysis, and part of the TEM analysis. I prepared the first draft of the manuscript and finalised the manuscript together with the co-authors.

Paper V

I prepared the samples, performed the measurements, analysed the data, and prepared the first draft of the manuscript. I finalised the manuscript together with the co-authors.

List of Abbreviations

AEMFC	Anion exchange membrane fuel cell
AFC	Alkaline fuel cell
AST	Accelerated stress test
BEV	Battery electric vehicle
BOL	Beginning of life
BSE	Backscattered electrons
CA	Chronoamperometry
CCL	Cathode catalyst layer
CCM	Catalyst coated membrane
CCS	Catalyst coated substrate
CE	Counter electrode
CL	Catalytic layer
COR	Carbon oxidation reaction
CV	Cyclic voltammetry/voltammogram
CP	Chronopotentiometry
E-beam	Electron beam
ECSA	Electrochemical available surface area
EOL	End of life
ePTFE	Expanded polytetrafluoroethylene
EQCM	Electrochemical quartz crystal microbalance
FCV	Fuel cell vehicle
FFPM	Perfluorinated elastomer
GDL	Gas diffusion layer
GHG	Greenhouse gas
HDV	Heavy-duty vehicle
HFR	High frequency resistance
HHV	Higher heating value
HOR	Hydrogen oxidation reaction
IL	Identical location
IT	Intermediate temperature
LDV	Light-duty vehicle
LHV	Lower heating value
LSV	Linear scan voltammetry
MEA	Membrane electrode assembly
MPL	Microporous layer

OCV	Open circuit voltage
ORR	Oxygen reduction reaction
PEM	Proton exchange membrane
PEMFC	Proton exchange membrane fuel cell
PEEK	Polyetheretherketone
PFAS	Per- and Polyfluoroalkyl Substances
PFSA	Perfluorinated sulfonic acid polymer
PGM	Platinum group metal
Pt	Platinum
Pt/C	Platinum on carbon
PTFE	Polytetrafluoroethylene
QCM	Quartz crystal microbalance
RDE	Rotating disc electrode
RE	Reference electrode
RH	Relative humidity
RHE	Reversible hydrogen electrode
SE	Secondary electrons
SEM	Scanning electron microscopy
SHE	Standard hydrogen electrode
SUSD	Start-up/shutdown
TEM	Transmission electron microscopy
UPD	Underpotential deposition
UPL	Upper potential limit
WE	Working electrode

Contents

Abstract	iii
List of Publications	v
Author Contributions	viii
List of Abbreviations	xi
1 Introduction	1
1.1 Scope of this Thesis	7
2 Catalysis & Electrochemistry	9
2.1 Catalysis	9
2.2 Electrochemistry	13
2.2.1 Redox Reactions	14
2.2.2 Electrocatalysis	18
3 Fuel Cells	19
3.1 Applications, Challenges and Future Prospects	19
3.2 Proton Exchange Membrane Fuel Cells: Working Principles and Components	22
3.2.1 Proton Exchange Membrane	23
3.2.2 Catalytic Layers	27
3.2.3 Gas Diffusion Layers	30
3.2.4 Membrane Electrode Assemblies	31
3.2.5 Flow-Fields and Current Collectors	31
3.2.6 Humidification	33
3.2.7 Additional Fuel Cell Stack Components	34
3.3 ORR and HOR Reaction Pathways	35
3.4 Performance Metrics and Efficiency Factors in PEMFCs	36
3.4.1 Cell Voltage and Efficiency	37
3.4.1.1 Voltage Losses	39
3.4.1.2 Effects of Partial Pressure of H ₂ and O ₂	43
3.5 Fuel Cell Degradation	44
3.5.1 Catalyst Dissolution	45

3.5.2	Start-Up/Shutdown and Cell Reversal	46
3.5.3	Temperature Cycling	50
3.5.4	Humidity Cycling	50
3.5.5	Pinholes	51
3.5.6	Chemical Damage and Poisoning	51
3.5.7	Mitigation Strategies	52
4	Experimental Techniques	53
4.1	Electrochemical Measurements	53
4.1.1	Set-Ups	53
4.1.1.1	Liquid Half-Cells	53
4.1.1.2	Electrochemical Quartz Crystal Microbalance	54
4.1.1.3	Fuel Cell Test Station	56
4.1.1.4	A Note on the Difference Between Fuel Cell and Half-Cell Measurements	57
4.1.2	Electrochemical Methods	59
4.1.2.1	Cyclic Voltammetry	60
4.1.2.2	Electrochemical Surface Area	61
4.1.2.3	H ₂ Crossover	63
4.1.2.4	Polarisation Curves	64
4.1.2.5	Electrochemical Impedance Spectroscopy	65
4.1.2.6	Activation Procedures and Recovery	66
4.1.2.7	Accelerated Stress Tests	67
4.2	Electron Microscopy	68
4.2.1	Identical Location Microscopy	69
4.3	Sample Preparation	72
4.3.1	Thin Film Fabrication	74
4.3.2	Preparation of Cross Sections	74
5	Results & Discussion	77
5.1	Mass Response and Dissolution of Pt Thin Films	77
5.2	Identical Location Electron Microscopy	82
5.2.1	Method Verification	83
5.2.2	Pt Dissolution and Particle Growth	85
5.2.3	Carbon Support Degradation	91
5.3	Intermediate Temperature Operation	101
6	Conclusions & Outlook	113
	Acknowledgement	115
	Bibliography	117

Chapter 1

Introduction

During the last two centuries, humanity has experienced a remarkable surge in living standards, largely through the use of technological innovations. From the industrial revolution in the 18th and the 19th century, to the start of the digital age in the end of the 20th century, each epoch has brought groundbreaking inventions that have reshaped our way of life. Unfortunately, these technological advances have come at a cost: a surge in greenhouse gas (GHG) emissions with a concurrent rise in global temperatures (see Figure 1.1), leading us down a path of global warming and extreme weather events [1], and the GHG emissions have continued to increase into to 21st century. The global average temperature has already risen to 1.1 °C above pre-industrial temperatures [1], which, if no action is taken, risks continuing to increase to well above the 2 °C target set by the Paris agreement [2].

From this, the question arises: What measures can and should be implemented to reduce GHG emissions and mitigate the impact of climate change? How can we move towards a sustainable future that ensures not only good living standards for the current generation but also for the generations to come? In response to these questions, the United Nations established an action plan, Agenda 2030, with 17 goals for sustainable development, each designed to address pressing global challenges while ensuring sustainable progress for humans and nature. Central to this effort is goal number 7, which calls for universal access to affordable and reliable energy, with a strong emphasis on increasing the use of renewable energy [5].

Sweden aims to be at the forefront of renewable energy production, setting and reaching goals well above the minimum requirements for EU member states [6, 7]. More than 60% of Sweden's energy production comes from renewable resources [8], which is made possible by good access to hydro and wind power, as well as the use of biomass co-generation [9]. With nuclear power included, 98% of Sweden's energy production uses carbon-free sources [10]. However, electricity must be produced at the moment it is consumed. Although Sweden has a yearly overproduction of energy and is a net exporter of electricity [10],

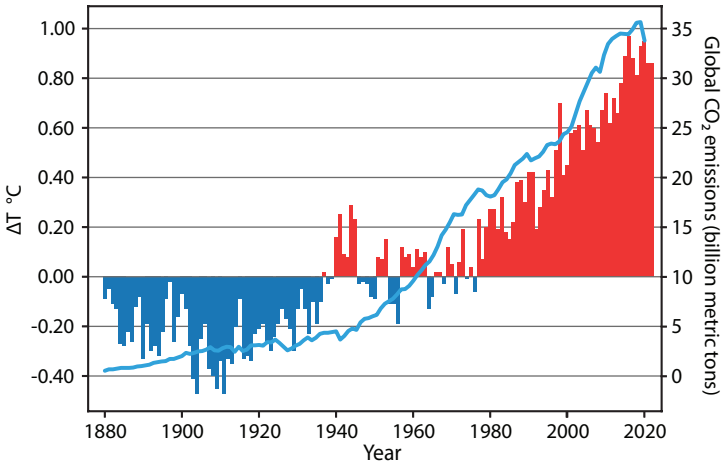


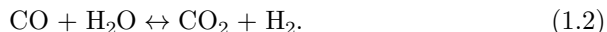
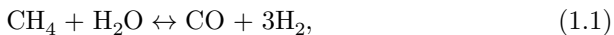
Figure 1.1: Change in average global temperature from 1880 to 2021, compared to the average temperature 1910–2000, and annual global emissions of CO_2 . Data from [3, 4]. The data for CO_2 emissions has been converted from metric tons of carbon to metric tons of CO_2 by multiplying it with a factor of 3.664.

the intermittent nature of many renewable energy sources means that Sweden needs to import electricity from neighbouring countries that use, e.g., coal and oil, when the hydro-plants are drying up or the wind turbines are not producing enough to satisfy demand. To fully utilise our resources and stop our dependence on fossil fuel, energy must somehow be stored during surplus production, to later be used to supply for our energy consumption during low production.

In addition to the energy sector, another large sector that needs to be decarbonised is the transport sector. Today, transportation accounts for approximately one-fifth of total greenhouse gas emissions globally [11]. To reach net zero emissions, everything from light-duty vehicles (LDV), such as small trucks and passenger cars, to heavy-duty vehicles (HDV), such as long-haul transportation and heavy machinery used in industry, need alternative energy solutions based on GHG-free technology if the goals of the Paris agreement are to be met. Although battery electric vehicles (BEVs) have taken a considerable part of the market when it comes to LDV [12], the technology is not optimal for many HDV applications where aspects such as large energy capacity, weight limitations, long operation times/ranges and fast refuelling/recharging times are crucial [13–16].

Part of the solution to reduce greenhouse gas emissions could be a large-scale implementation of hydrogen in our energy system. Hydrogen, which is the most abundant element in the universe, can be found and extracted from many sources on Earth. Depending on the source of hydrogen, and what methods are used to refine it, hydrogen can be classified as either grey, blue or green. Grey hydrogen is produced using hydrocarbon reforming, often with methane

as feedstock, in a process known as steam reforming. Globally, 76% of H₂ production comes from steam reforming [17]. In steam reforming, methane is mixed with water in the form of steam and a mixture of hydrogen with small amounts of CO is created over a catalyst [18],



This gas mix is also known as syngas. CO₂ is produced during the steam reforming process and, if no further steps are taken, this CO₂ is emitted into the atmosphere. If steam reforming is combined with carbon capture and storage techniques, thus reducing CO₂ emissions during production, the hydrogen is instead called blue hydrogen [19].

Green hydrogen is hydrogen produced using electrolysis [20]. In electrolysis, electricity is used to split water into its constituents hydrogen and oxygen,



If the electricity used for this process comes from renewable energy sources, such as wind, hydro, or solar energy, green hydrogen production does not cause GHG emissions. In addition, green hydrogen has a high purity, which is important in many applications sensitive to, e.g., CO-poisoning. Unfortunately, green hydrogen only represents about 2% of the current global hydrogen production [17].

Green hydrogen offers a promising solution to balance an energy system based on renewable sources [17]. During excess electricity production, electrolyzers can quickly be started to produce hydrogen, which can then be stored, for example, in the form of liquid hydrogen or as pressurised gas [21]. The hydrogen can later be converted back to electricity, when energy production is low, using fuel cells, helping to balance the intermittent supply of energy in the power grid [22]. A fuel cell works like an electrolyser in reverse, combining hydrogen with oxygen to produce water,



This process releases energy that can be collected in the form of electricity, with the only by-products being pure water and heat, thus having negligible adverse environmental impact. By implementing electrolyzers powered by renewable resources together with fuel cells, hydrogen can become an important energy vector in a sustainable energy system with zero greenhouse gas emissions [23–25], illustrated in Figure 1.2.

In addition to having the possibility of being a GHG-free energy carrier, hydrogen has several other advantages and benefits. For one thing, the resources

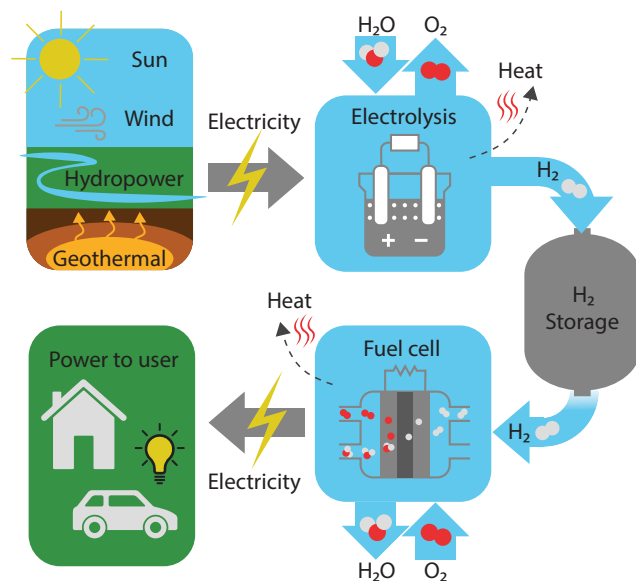


Figure 1.2: Schematic of a GHG-emission free energy system utilising hydrogen as an energy vector.

needed for green hydrogen production, i.e., water, is readily available all over the planet, and thus hydrogen can in many cases be produced locally where it is needed, which could help many nations reduce their dependency on importing resources such as oil and gas. The technologies involved are also very versatile, adaptable, and scalable. Hydrogen can be produced and used in everything from small-scale domestic appliances requiring less than 10 W of power, to large-scale power plants that produce 10 to 100 MW of power [26].

Hydrogen solutions such as fuel cell vehicles (FCVs) are often compared to battery-based solutions such as BEVs, as both are GHG-free alternatives to conventional vehicles that use internal combustion engines. Among the advantages of FCVs over BEVs is a very high energy density per hydrogen mass compared to, e.g., lithium, see Figure 1.3. Thus, hydrogen-based systems can be significantly lighter than equivalent battery systems. For comparison, hydrogen has a gravimetric energy density, i.e., energy per mass, of almost 140 MJ kg^{-1} , while diesel and gasoline have about a third of that at ca 45 MJ kg^{-1} , and batteries only have an energy capacity of $0.1\text{--}2 \text{ MJ kg}^{-1}$ [27]. In particular, when considering large high-power systems, the weight factor becomes a crucial consideration. As battery systems tend to have substantially higher weights compared to equivalent fuel cell systems, this gives fuel cells a considerable advantage in systems where weight limits are stringent, such as within the aviation industry or long-haul transportation. However, hydrogen gas has a low volumetric energy density, i.e., energy per volume, even when

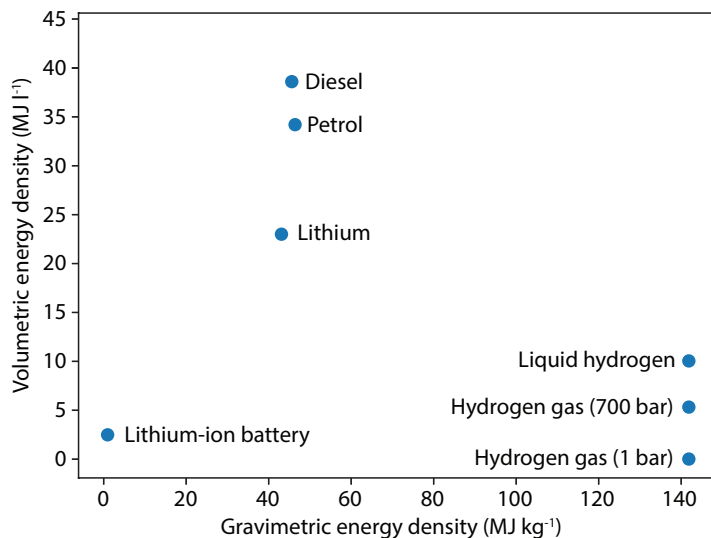


Figure 1.3: Volumetric vs. gravimetric energy density of hydrogen (at 1 bar, at 700 bar and in liquid form), diesel, petrol, lithium, and lithium-ion batteries. Data from [27, 28].

compressed, with hydrogen compressed to 700 bar having a volumetric energy density of 5.3 MJ l^{-1} . Thus, if volume is constrained, other means of storing hydrogen, such as liquid organic hydrogen carriers or metal hydrides, might need to be explored [28–31].

At shorter distances, BEVs can have advantages over FCVs, for example, in terms of cost. However, in heavy-duty machinery and long-distance transportation, FCVs are expected to be a good competitor, as FCVs have operating ranges and fuelling times comparable to those of conventional internal combustion engine vehicles, and the possibility of scaling up fuel cells with a much smaller weight penalty compared to batteries [16]. Nevertheless, fuel cell technology is still immature compared to the much more well-established battery technologies and has hitherto mostly been used in niche market tests. Furthermore, large-scale implementation of FCVs requires a build-up of infrastructure of the hydrogen supply chain and a large increase in production capability of (green) hydrogen to meet the anticipated increase of demand.

Some of the biggest barriers to successful commercialisation of fuel cells today are considered to be the cost of production and the lifetime [32]. Much of the production cost of a fuel cell stack comes from the need to use expensive raw materials. For fuel cells to work efficiently, they need catalysts that enable the chemical reactions to occur at a reasonable rate. Due to the harsh conditions of a fuel cell, such as highly acidic environments and high and varying potentials, platinum (Pt), or other platinum group metals (PGMs) and PGM-alloys are the state-of-the-art catalysts for fuel cells. Unfortunately, these materials tend to be scarce and expensive, and the cost of the catalyst in large-scale production

is estimated to be more than 40% of the total production cost [33]. Figure 1.4 shows a breakdown of the relative cost contribution of the different fuel cell components at different production volumes.

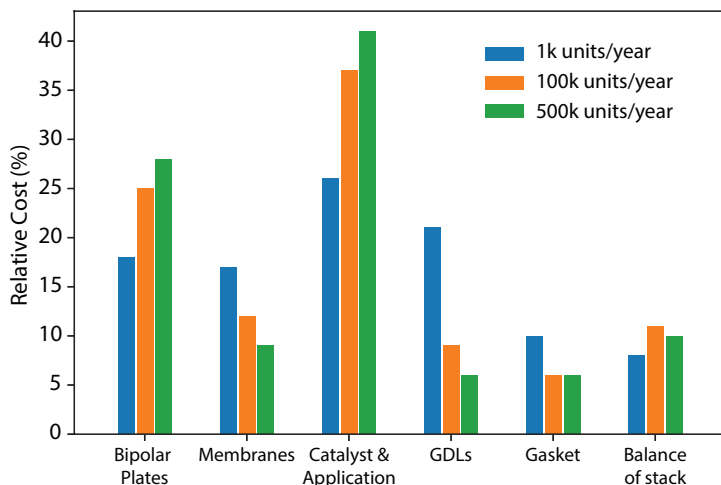


Figure 1.4: Estimated relative cost of proton exchange membrane fuel cell components per yearly production volume. Data from [33].

The United States Department of Energy has set several targets for fuel cells to be reached by 2025, such as an 8 000 h lifetime for LDV with less than 10% loss of initial performance, a target cost of 30 \$ kW⁻¹ and a loading of 0.10 g_{PGM} kW⁻¹ [32, 34, 35]. For reference, a lifetime of 8 000 h is an average of approximately 1 h of use per day for more than 20 years, and a loading of 0.10 g_{PGM} kW⁻¹ would give a total loading of around 10 g_{PGM} for a system suitable for an LDV, which is comparable to the 7–10 g_{PGM} used in the catalytic converter of modern diesel vehicles [36, 37]. The European initiative Clean Hydrogen Joint Undertaking has adopted similar targets, with the aim of achieving lifetimes of 30 000 h for HDVs by 2030 [38]. While there are examples of fuel cells that have been successfully operated for well over 30 000 h [39], more development is still needed to reach all targets simultaneously. To reduce production cost, efforts have been put into maximising the use of materials, e.g., by using nanostructured materials [40–45], or reducing the load of PGM by using PGM alloys with transition metals or rare earth metals [46–50]. Furthermore, research needs to be done on the degradation mechanisms of fuel cell components, so that more durable materials and better driving routines can be developed to achieve longer lifespans. Preventive measures against degradation of PEMFCs that have been shown to be beneficial in reducing degradation include using Pt-alloys such as Pt-Co [51, 52], reinforcing the membranes and including radical scavengers [53–55], integrating PEMFC and battery systems for hybrid power solutions [56], and using appropriate gas purging of the system during start-up and shutdown [57, 58].

1.1 Scope of this Thesis

This thesis aims to contribute to the development of fuel cell technologies for a sustainable and emission-free society. It does so by providing insight into how fuel cells, and in particular the Pt catalyst and carbon support in proton-exchange membrane fuel cells, degrade during various operational conditions. This thesis is based on previous work published by the author [59].

Chapter 2 presents the basics of catalysis and electrochemistry to establish a foundation for further discussion. Chapter 3 explores the theory and practical construction of proton exchange membrane fuel cells, along with the challenges and limitations associated with their components, to contextualise the research and give a broader understanding of fuel cell technology.

Chapter 4 provides an overview of the key methodologies employed in the studies included within this thesis. Chapter 5 presents the key findings from Papers I–V, shedding light on the significant results and their implications. Finally, Chapter 6 summarises the conclusions of this thesis and proposes recommendations for further work.

Chapter 2

Catalysis & Electrochemistry

Before delving into the subject of fuel cell systems, we need to start with a fundamental understanding of catalysis and electrochemistry, as these are crucial to understand the principles of fuel cells.

2.1 Catalysis

Catalysis is the act of increasing or modifying the rate of a chemical reaction by the addition of a substance, called a catalyst, without the catalyst itself being consumed in the process. Catalysis is immensely important for our society, and it plays a pivotal role in various industries. It is estimated that approximately 90% of industrial chemicals are manufactured through catalytic processes [60], which includes products such as fertilisers [61], petroleum cracking products [62], polymers [63, 64], and hydrogen from steam reforming [65, 66], and catalysis is also highly important for the use in exhaust cleaning [67–70]. All modern petrol- and diesel-fueled cars have catalytic converters to reduce the amount of harmful and toxic emissions in the exhaust gas such as NO_x , CO and hydrocarbons emitted during the combustion process. Thus, it can hardly be overstated how immensely integral catalysis is in our society.

A catalyst does not affect the equilibrium and although only thermodynamically favourable reactions can be catalysed, the addition of a catalyst can drastically increase reaction rates—often by many orders of magnitude—thus increasing output. Furthermore, in reactions with multiple possible products, addition of a well-chosen catalyst can increase selectivity and thereby favourably alter the ratio of desired end-product to undesired by-products, reducing the energy and resources spent on parasitic reactions and reducing the energy consumed to separate out the desired products. In short, catalysis is exceptionally important for a sustainable society with low carbon emissions and more environmentally

friendly and energy efficient chemical processes.

Catalysis can be divided into two main categories: Homogeneous and heterogeneous. Homogeneous catalysis occurs when both the reactant and the catalyst exist in the same phase, such as gaseous or liquid. Heterogeneous catalysis, on the other hand, involves catalysts in a different phase from the reactants. Typically, in heterogeneous catalysis, the catalyst is in a solid phase while the reactants may be either in a liquid or gaseous phase. Consequently, the reactions occur at the interface between the catalyst surface and the gas/liquid phase. The rest of this thesis will only deal with heterogeneous catalysis.

Figure 2.1 illustrates possible energy pathways of a chemical reaction with, and without, a catalyst present. The catalyst can stabilise intermediate species, thus providing alternative pathways with lower energy barriers than the uncatalysed reaction [71, 72]. The reaction rate of a specific reaction step can be described by

$$r = kC, \quad (2.1)$$

where k is the rate constant and C is the concentration of the reactant. The rate constant, and thereby the reaction rate, is correlated to the energy barrier E_a associated with that reaction step via the Arrhenius equation

$$k = A \exp \frac{-E_a}{RT}, \quad (2.2)$$

where A is a pre-exponential factor, R is the universal gas constant and T is the absolute temperature [72, 73]. From Eq. 2.2, it is clear that lower energy barriers leads to higher reaction rate. Lower energy barriers are simply easier to overcome, and thus a specific catalysed reaction pathway with lower associated energy barrier is more likely to occur than the uncatalysed reaction pathway. This is the working principle which enable catalysts to function [71]. It is important to note that the energy states of the reactants and products will be the same regardless of whether the reaction is catalysed or not, and that catalysis does not shift the overall thermodynamics or equilibrium point.

The catalysed reaction can generally be divided into a sequence of elementary steps. First, the reactants diffuse to the surface of the catalyst and adsorb. Subsequently, the reactants diffuse on the surface and undergo reactions on the surface, often involving multiple intermediate steps. Finally, the products desorb from the surface and diffuse away, leaving the catalytic site free for the process to repeat with a new reactant adsorbing on the surface. Each elementary step has its own associated activation energy barrier, and some reactions have a clear rate determining step, which is an elementary reaction that controls the overall reaction rate.

A good tool for screening new catalysts is the Sabatier principle. It states that the reactant or intermediates should bind neither too strongly nor too weakly to the catalyst [74], but instead, should have a binding energy somewhere in

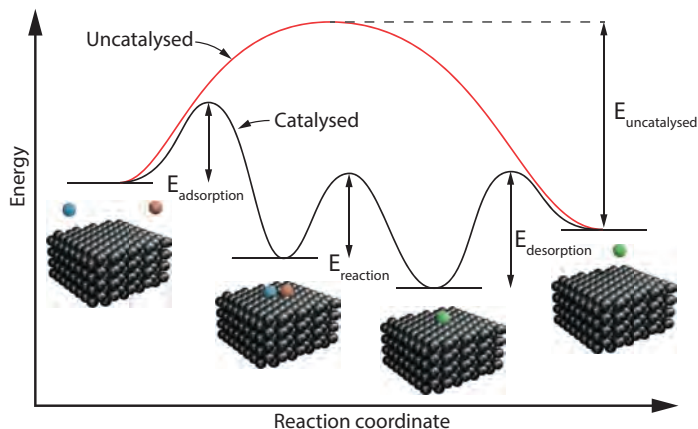


Figure 2.1: Energy diagram of a reaction with and without a catalyst present. The catalyst stabilises intermediate species thus providing an alternative pathway with lower energy barriers.

the middle. If the reactants bind too strongly to the surface, the reactants will not desorb from the surface, and will physically block further reactants from binding to the surface, and the desorption of products will be the rate-limiting step. On the other hand, if the binding strength between the reactants and the catalyst is too weak, the reactants will not interact with the surface strong enough, and the adsorption of the reactants will be the rate-limiting step [71]. The Sabatier principle can be illustrated graphically with a so-called Volcano plot, aptly named after its triangular shape. Figure 2.2 shows the activity of different metals for the oxygen reduction reaction (ORR) as a function of the binding strength between oxygen and the catalyst. The activity follows a volcano-shaped pattern [46]. The top of the volcano gives the optimal binding energy, and a deviation from this peak sees a decline in activity on both sides. In addition to considering the binding energy of reactants and products, the mass activity of a catalyst—quantified by the number of reactions per mass per time unit—is inherently limited by the available active sites on its surface. To fully utilise all catalyst material, the surface-to-mass ratio should be maximised.

With these two concepts in mind, two key strategies for tuning and improving the catalytic activity emerge: the catalytic activity can be increased either by tuning the binding energy to reactants, products and intermediate species to increase the intrinsic catalytic activity, and/or by maximising the available active sites on the catalyst surface. The binding energy can be tuned by doping the catalyst material with other elements, which affects the electronic binding energy by either changing the energy levels of the electrons (ligand effect) or by inducing strain in the catalyst (strain effects). The binding energy and surface area of a catalyst can also be maximised by carefully designing nanostructured materials. Nanostructured materials offer enhanced activity providing a range of different sites such as edges, defects or specific crystal planes, or simply by

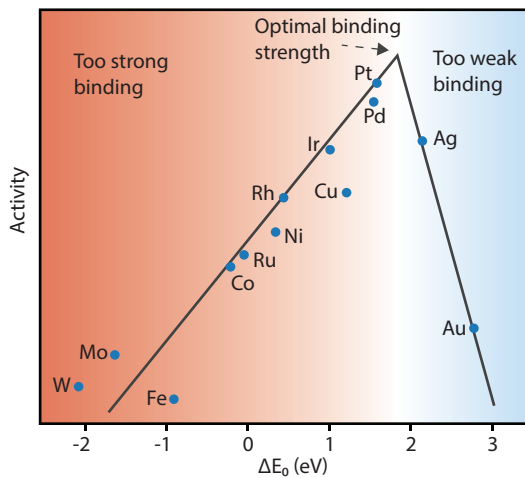


Figure 2.2: Volcano plot of activity vs. oxygen binding energy for the ORR on different metals. Pt is located circa 0.1 eV below the optimal binding energy. Data from [46].

providing greater surface area per unit mass.

2.2 Electrochemistry

Electrochemistry is a branch of science that deals with the relation between electrical potential and chemical reactions, and the conversion between electrical and chemical energy. The field has a long history dating back to the 18th century. In the later part of the 1780s, Luigi Galvani discovered bioelectricity when he found that the muscles of a dead frog twitched when they were connected to two pieces of metal in a circuit [75]. From this, Galvani concluded that living beings had an innate vital force that he named ‘animal electricity’. Galvani’s fellow scientific colleague Alessandro Volta rebutted this idea and realised that the electricity came not from the frog legs but from the two different metals in connection with each other. Volta built on those ideas further, demonstrating in 1794 that an electric current is produced when two sheets of metals and brine-soaked cardboard or cloth are arranged in a circuit [76]. This became the Voltaic pile, which was the first electrical battery. The Voltaic pile was soon after used by William Nicholson and Anthony Carlisle in 1800 to discover electrolysis of water, where an electrical potential is used to drive the non-spontaneous process of splitting water into hydrogen and oxygen, by connecting a Voltaic pile to a water-filled tube via two platinum wires, at which they noticed that bubbles were formed on either wire [77, 78].

The opposite reaction of water electrolysis—producing electricity by combining hydrogen and oxygen—was first demonstrated in 1839 by Sir William Robert Grove, who created a crude version of a fuel cell using Pt foils and dilute sulfuric acid [79]. Despite its early start, it would take almost a century until a practical version of a hydrogen fuel cell was developed, when Francis Thomas Bacon created a 5 kW alkaline fuel cell (AFC) in 1932. The AFC technology was later used to generate both power and drinking water for astronauts in the Apollo programme by NASA in the 1960s [80]. The AFC has since been replaced by proton exchange membrane fuel cells (PEMFC), which is the leading fuel cell technology today. Ongoing research also explores alternative options to PEMFCs, such as anion exchange membrane fuel cells (AEMFC).

Today, electrochemistry plays a vital role in many aspects of our life and society, from batteries in our cell phones to electroplating of metals and in large-scale industrial production of many indispensable chemicals. Together with the rise of electrification within our energy systems, and the shift away from using fossil fuels as energy carriers, electrochemical solutions like batteries, electrolyzers and fuel cells are exceptionally important.

Electrochemical reactions take place at the interface between an electrode, which is an electrically conductive material, and an electrolyte, which contains ions. Electrochemical reactions can be either spontaneous processes, where chemical energy is converted to electrical energy in a galvanic cell, or non-spontaneous processes, where externally provided electrical energy is used to drive chemical reactions in an electrolytic cell.

2.2.1 Redox Reactions

A redox reaction is a chemical reaction in which electrons are transferred from one species to another [81]. Every electrochemical reaction is also a redox reaction. A redox reaction can be divided into its two half-reactions, which can be physically separated in space and studied independently. In its simplest form, a redox reaction involves an oxidised species Ox that accepts n electrons to be reduced to species Red ,



A redox reaction can be characterised by the quotient Q , which is the ratio between the activity a of the reduced species and the oxidised species. Q can, if the activities are close to unity, be approximated by the quotient between the molar concentration of the respective species:

$$Q = \frac{a_{Red}}{a_{Ox}} = \frac{[Red]}{[Ox]}, \quad (2.4)$$

where $[]$ is used to denote the concentration. Thermodynamics gives us that the change in Gibbs free energy ΔG at a given state is related to the Gibbs free energy under standard conditions ΔG^\ominus and Q by

$$\Delta G = \Delta G^\ominus + RT \ln Q_r. \quad (2.5)$$

A redox reaction can be classified as either spontaneous, if ΔG is negative, i.e., energy is expelled, or non-spontaneous if ΔG is positive, i.e., energy has to be added for the reaction to occur. In electrochemistry, a spontaneous reaction correlates to a galvanic cell and a non-spontaneous reaction corresponds to an electrolytic cell. ΔG is then either the maximum amount of work that can be recovered from the reaction or the minimum work required to drive the reaction. In an electrochemical cell, the electrical work performed by the cell is correlated with the cell potential E by

$$W_{\text{electrical}} = -nFE, \quad (2.6)$$

where F is the Faraday constant and n is the number of electrons exchanged in the process. If all work from an electrochemical reaction is converted to electrical work, it follows that

$$\Delta G = W_{\text{electrical}} = -nFE, \quad (2.7)$$

$$E = -\frac{\Delta G}{nF}. \quad (2.8)$$

Combining Eq. 2.5 with Eq. 2.8 gives the Nernst equation of the half reaction:

$$E^0 = E^\ominus - \frac{RT}{nF} \ln Q = E^\ominus - \frac{RT}{nF} \ln \frac{[Red]}{[Ox]}, \quad (2.9)$$

where E^0 is the equilibrium potential at a given state and E^\ominus is the equilibrium potential under standard conditions [81].

In a cell based on two specific half-reactions, the total cell voltage will simply be the difference between the equilibrium potentials of each half-cell reaction,

$$E_{\text{Cell}}^0 = E_1^0 - E_2^0 \quad (2.10)$$

$$= E_1^\ominus - E_2^\ominus - \left(\frac{RT}{nF} \ln \frac{[Red_1]}{[Ox_1]} - \frac{RT}{nF} \ln \frac{[Red_2]}{[Ox_2]} \right) \quad (2.11)$$

$$= E_{\text{Cell}}^\ominus - \frac{RT}{nF} \ln \frac{[Red_1][Ox_2]}{[Red_2][Ox_1]}, \quad (2.12)$$

where E_{cell}^0 is the equilibrium cell voltage in the given state, E_{cell}^\ominus is the equilibrium cell voltage under standard conditions, and the indices $_1$ and $_2$ mark each redox reaction involved in the complete cell reaction. The Nernst equation gives the cell voltage under thermodynamical equilibrium conditions, i.e., when no net current is flowing through the electrodes and the reductive and oxidative currents are equal.

When the electrode potential deviates from the equilibrium potential, current will start to flow through the electrode. The current density j through an electrode is related to the overpotential η , which is a measurement of how much the half cell potential deviates from the equilibrium ($\eta = E - E^0$).

Assuming the mass transport rate to the surface is much greater than the consumption of reactants, i.e., that the concentration at the surface is practically the same as in the bulk and that the charge transfer step is the rate limiting step, the current density can be described by the Butler-Volmer equation,

$$j = j_0 \left(e^{\frac{(1-\alpha)nF\eta}{RT}} - e^{\frac{-\alpha nF\eta}{RT}} \right), \quad (2.13)$$

where j_0 is the exchange current density, n is the number of electrons transferred in the reaction, and α is a transfer coefficient [82]. At high overpotentials,

$|\eta| \gg 0$, one term in Eq. 2.13 goes to zero and can be neglected. This leads to two different cases depending on if $\eta \gg 0$ or $\eta \ll 0$, representing anodic and cathodic currents, respectively;

$$\text{Anodic :} \quad j = j_0 e^{\frac{(1-\alpha)nF\eta}{RT}}, \quad (2.14)$$

$$\text{Cathodic :} \quad j = -j_0 e^{\frac{-\alpha nF\eta}{RT}}. \quad (2.15)$$

Taking the common logarithm of Eq. 2.14 and Eq. 2.15 gives

$$\text{Anodic :} \quad \log j = \log j_0 + \frac{(1-\alpha)nF\eta}{2.303RT}, \quad (2.16)$$

$$\text{Cathodic :} \quad \log |j| = \log j_0 - \frac{\alpha nF\eta}{2.303RT}. \quad (2.17)$$

Rewriting Eq. 2.16 and 2.17 and isolating η on the left-hand side gives the Tafel equation.

$$\text{Anodic :} \quad \eta = \frac{2.303RT}{\alpha nF} \log j_0 + \frac{2.303RT}{(1-\alpha)nF} \log j, \quad (2.18)$$

$$\text{Cathodic :} \quad \eta = \frac{2.303RT}{(1-\alpha)nF} \log j_0 - \frac{2.303RT}{\alpha nF} \log |j|, \quad (2.19)$$

or, in its simplified form,

$$\eta = a + b \log |j|, \quad (2.20)$$

where b is known as the Tafel slope. The Tafel slope is found by plotting η vs $\log j$ (Figure 2.3) and taking the slope of the curve in the linear Tafel region. The Tafel slope shows how much the overpotential needs to be increased to have a ten-fold increase of current. For a good estimation of the Tafel slope, the plot should be linear over at least two orders of magnitude, and the slope should be measured above a large overpotential ($\eta > 120$ mV) [83], which can be difficult in systems highly limited by mass transport even at low current densities. The transfer coefficient α can be calculated from the Tafel slope, and the exchange current density j_0 is found by extrapolating the line and finding the intersection with the x-axis. The Tafel slope, in combination with modelling and simulations, is an indicator of what type of reaction mechanisms are dominating and what elementary steps are rate limiting in a reaction. The exchange current density is the rate of backward and forward reaction at equilibrium and measures the intrinsic reaction rate of the electrode. A high

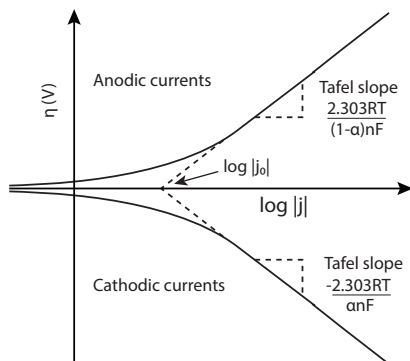


Figure 2.3: Tafel plot showing anodic and cathodic currents for $\alpha = 0.5$. The Tafel slope is calculated from the linear portion of the plot, and the exchange current j_0 is found at the intersection of the slope with the x-axis.

exchange current density is desirable for good electrode performance with low overpotentials.

Another important concept for the study of electrochemical systems derived from the Nernst equation is the Pourbaix diagram, which shows the pH dependence for the equilibrium potential of different reactions and shows which species are stable at the respective potential. For water (H_2O) at pH 0, the Pourbaix diagram indicates that the stability window lies between 0 and 1.23 V vs. the standard hydrogen electrode (SHE), as shown in Figure 2.4a [84]. At potentials of around 1.23 V vs. SHE and above, water undergoes oxidation to produce $\text{O}_2(\text{g})$, and below 0.0 V vs. SHE water undergoes reduction to generate $\text{H}_2(\text{g})$. According to the Nernst equation (Eq. 2.12), at higher pH these potential limits shift by

$$E = E_0 - \frac{2.303RT}{F} \log [H^+] = E_0 - \frac{2.303RT}{F} \text{pH}, \quad (2.21)$$

where E_0 is the redox potential at pH 0, R is the gas constant, T is the temperature, F is the Faraday constant, and $2.303RT/F \approx 59$ mV at 25 °C. However, the potential difference between oxygen evolution and hydrogen evolution at room temperature and ambient pressure for any given pH will still be 1.23 V.

When the electrode potential is measured during experiments, the potential is measured against the potential of another well-defined reaction. Although many different sets of redox reactions can be used as a reference for practical measurements, the potential of the measurements is typically converted to a common scale for ease of comparison. The standard that defines the potential scale is the SHE. The SHE scale is based on immersion of an ideal Pt electrode in a solution with a H^+ concentration of 1 M while bubbled with 1 bar of H_2 . The resulting potential from the hydrogen redox reaction defines the standard

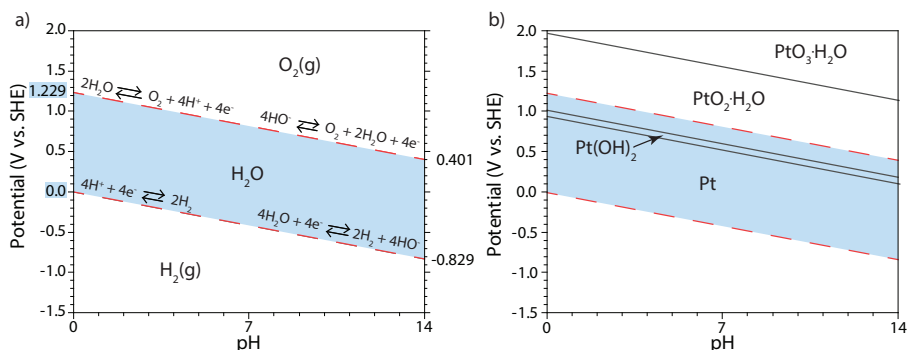


Figure 2.4: Pourbaix diagram, showing the thermodynamically stable phases for different potentials at a specific pH at room temperature and ambient pressure, of a) water and b) Pt. The blue area shows the stability domain for water which at pH 0 is 0–1.23 V vs. the SHE. Data from [84].

for 0 V at all temperatures. However, SHEs are impractical to construct and use, and hence two other types of electrode are often used instead; either the normal hydrogen electrode or the reversible hydrogen electrode (RHE). Like the SHE, the RHE also uses the hydrogen redox potential, but with the practical difference that it is defined as 0 at every pH.

2.2.2 Electrocatalysis

Electrocatalysis is a subset of catalysis that deals with the catalysis of electrochemical reactions. In an electrochemical setup, the electrocatalyst can be either the electrode itself, such as copper plates, or supported on the electrode, e.g., in the form of nanoparticles. Electrocatalysts function by lowering overpotentials and increasing selectivity, thereby reducing the amount of energy needed to drive a specific reaction.

In a galvanic cell (where the reactions are spontaneous), the overpotential determines how much voltage is lost compared to the theoretical maximum; in an electrolytic cell (where external energy input is required to drive the cell), the overpotential of the cell determines how much more energy is applied to drive the reaction. In both cases, overpotentials lead to loss of efficiency. Thus, a good electrocatalyst is characterised by good activity, i.e., to have high current densities at low overpotentials. Some other key criteria for an efficient electrocatalyst include selectivity and stability. The stability of the electrocatalyst means it should be able to withstand the relevant potential ranges and operating conditions, with minimal degradation and deactivation. Selectivity means that the catalyst should preferentially catalyse only the desired reactions while suppressing side reactions.

Chapter 3

Fuel Cells

In this chapter, I aim to introduce the fundamental principles and wide-ranging applications of fuel cell systems within the broader energy landscape. The focus is primarily on PEMFCs, exploring their current state-of-the-art components and the challenges they face. The key topics discussed include the working principle of the components, reaction mechanisms, performance metrics, voltage losses, and degradation issues, which are critical to understanding the basic working principle and potential improvements of PEMFC technology.

Fuel cells come in various types, often classified according to the type of electrolyte or fuel they use, and/or the operating temperature. Table 3.1 shows some common types of fuel cells, together with characteristic parameters. Despite their differences, all fuel cells share a common basic structure and concept. They consist of two electrodes: an anode, where a fuel is oxidised, and a cathode, where an oxidising agent is reduced. These electrodes are connected via an electrolyte, which can be either liquid or solid, facilitating the conduction of ions between the reaction sites. Electrons move from anode to cathode through an external circuit, thus providing electrical work. Fuel and oxidants, provided in gas or liquid form, are continuously supplied to the respective electrodes to sustain the reactions.

3.1 Applications, Challenges and Future Prospects

Fuel cells, with their promise of high efficiency and low emissions, have been the focus of considerable research and development over the years. One of the primary applications for fuel cells is the transportation sector. For the LDV sector, FCVs are an alternative solution to BEVs as emission-free alternatives to internal combustion engines. Although FCVs lag behind BEVs in terms of market share, they have become commercially available in the last decade, with several brands introducing their versions to the market [89]. Toyota launched its first commercial FCV, the Toyota Mirai, in 2014. The Toyota Mirai has demonstrated 6 000 hours of operation under actual driving conditions [90].

Fuel cell type	PEMFC ¹	AFC ²	DMFC ³	PAFC ⁴	SOFC ⁵	MCFC ⁶
<i>Electrolyte</i>	Polymer	KOH	Polymer	Phosphoric acid	Solid oxide or ceramic	Molten carbonate
<i>Charge carrier</i>	H ⁺	OH ⁻	H ⁺	H ⁺	O ₂ ⁻	CO ₃ ²⁻
<i>Fuel</i>	H ₂	H ₂	Methanol	H ₂	H ₂ , hydrocarbon	H ₂ , hydrocarbon
<i>Operation temperature</i>	20–100 °C	40–90 °C	70–90 °C	150–200 °C	600–1000 °C	650 °C
<i>Notable applications</i>	Vehicles, stationary and backup power	Space vehicles [†]	Portable electronic systems	Combined heat and power systems	Combined heat and power systems	Combined heat and power systems

¹Proton exchange membrane fuel cell, ²alkaline fuel cell, ³direct methanol fuel cell,

⁴phosphoric acid fuel cell, ⁵solid oxide fuel cell, ⁶molten carbonate fuel cell.

[†]Historical application.

Table 3.1: Operational parameters and applications of some common fuel cell types. Data from [85–88].

Other companies, such as Hyundai, Honda, Mercedes-Benz, and GM, have also released their own versions of FCVs. In the USA, a few thousand FCVs have been sold or leased so far [16]. However, despite their availability, the widespread adoption of FCVs for LDVs is limited by the lack of refuelling infrastructure, and their costs are currently higher than that of comparable BEVs [89].

Recently, larger potential markets for PEMFCs have attracted attention, particularly in the HDV sector [16, 89]. This includes long-haul transportation, buses, and machinery such as forklifts. Long-haul trucks drive, on average, much longer distances than passenger cars, and contribute significantly more to the total GHG emissions from the transportation sector. Implementing cleaner fuels for HDVs would substantially reduce global GHG emissions. Due to weight and recharging times, batteries are not optimal for most HDV applications. PEMFCs may be a more suitable option as they do not have the same inherent correlation between weight and energy output as batteries, and have refuelling times on the order of minutes rather than hours. Furthermore, since the routes for trucking and buses are more predictable, developing the necessary supporting infrastructure is easier than for passenger cars, requiring fewer refuelling stations along pre-planned routes [16].

With the shift in focus from LDVs to HDVs, the demands on PEMFCs also change. While PEMFCs for LDVs prioritise low loadings of Pt to reduce costs, and high power densities to reduce weight and size, PEMFCs for HDVs have more stringent requirements for durability and reliability under new types of operating conditions [16]. The US Department of Energy (DOE) assumes that class 8 trucks need lifetimes exceeding 12 years and 1.2 million miles

[91], with similar targets from other organisations setting the lifetime to more than 25 000 hours [16], which is notably higher than the 8 000-hour target set for LDVs. Successful small-scale implementations of PEMFCs for HDVs can already be seen in both Europe and the USA, where fleets of fuel-cell buses have been in operation since the early 2000s [92, 93] and more recently several project involving fuel-cell trucks have been implemented in, e.g., Norway and Switzerland [94, 95]. Some of the fuel-cell buses have shown operating times of more than 25 000 hours, with an average lifetime of around 14 000 hours [92, 96], showing the feasibility of reaching the lifetime targets. However, achieving both lifetime and cost goals simultaneously remains a challenge.

As use of PEMFCs for HDVs shifts the PEMFC targets towards longer lifetimes, operating costs become more important than initial capital costs to the total cost of ownership. Thus, higher efficiency and better durability are crucial to minimising overall operating costs, rather than simply reducing the noble metal content [16]. The shift to HDVs also changes the conditions that fuel cells must endure. For example, fuel cells for HDVs would benefit from stability at higher temperatures (above 90 °C) due to cooling requirements and the size and weight of radiators. Other heavy-duty applications where fuel cells are considered for use include the maritime and aviation industries. In these sectors, lifetime and reliability are even more critical. In high-power applications such as aircraft take-offs, tolerance to higher temperature could substantially reduce the need for excessive cooling capability, which could offer benefits in efficiency and system design as radiators can contribute significantly to the system weight and energy consumption [97].

In addition to transportation, PEMFCs are also used as portable and stationary power generators [98], such as auxiliary power units and backup power generators in, for example, hospitals. For these applications, PEMFCs have several advantages over diesel generators, such as high reliability and operational stability, high efficiency even at low loads, no toxic emissions or pollutants, and low vibration and noise levels. Moreover, their low thermal and acoustic signatures make fuel cells suitable for use as auxiliary power units for military applications [99]. Fuel cells have also been successfully implemented as auxiliary power units for aircrafts [100]. For stationary applications, the ease of scalability makes fuel cells suitable for various uses in residential, industrial, and commercial settings. The ease of scalability in fuel cells can be exemplified by current fuel cell applications ranging from 1 W handheld charging units to 100 kW engines for FCVs, up to 10–100 MW power plants supplying hundreds of thousands of households with power [101–103].

In summary, the potential applications for fuel cells are numerous. However, each case has its own unique specific requirements, benefits, and limitations that need to be considered in research and development.

3.2 Proton Exchange Membrane Fuel Cells: Working Principles and Components

PEMFCs are one of the more well-researched and commercially successful types of fuel cells. PEMFCs typically operate at around 80 °C or below, and are classified as low-temperature fuel cells, compared to, e.g., solid oxide fuel cells which can operate at over 750 °C [104]. The lower temperature makes start-up times much faster in the PEMFC than high-temperature fuel cell, thus making PEMFC a better option for applications such as FCVs. A PEMFC uses hydrogen as a fuel and combines it with oxygen, often provided from the ambient air, in an exothermic reaction to create water,

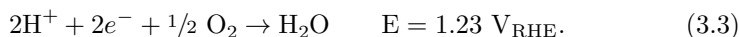


and thus, the only by-products in this reaction are pure water and heat. The product, H_2O , has a lower enthalpy than the reactants, H_2 and O_2 , and it is that difference in energy that is released during the reaction and which can be utilised.

If H_2 and O_2 react directly, all this energy is released as heat. To instead get the energy released in Eq. 3.1 directly as electrical energy, the reaction must be physically separated into its two half reactions, one at the anode and one at the cathode. At the anode, hydrogen is split into protons and electrons in the hydrogen oxidation reaction (HOR),



where RHE stands for the reversible hydrogen electrode. At the cathode, the protons and electrons are combined with oxygen to form water, in the ORR,



Instead of releasing the energy generated during the reaction described in Eq. 3.1 as heat, a PEMFC harnesses this energy to generate an electric current. This is achieved by separating the half-reaction described in Eq. 3.2 and Eq. 3.3 physically in space, so that protons move between the reactions via an electrolyte membrane and electrons travel through an external circuit. This separation is achieved by the well-thought-out design of a fuel cell. Figure 3.1 shows the typical structure and components of a single cell fuel cell, which includes a central ion-conducting membrane flanked by anode and cathode electrodes, gas diffusion layers (GDLs), flow fields, and current collectors. These individual components will be discussed in more detail in the following sections.

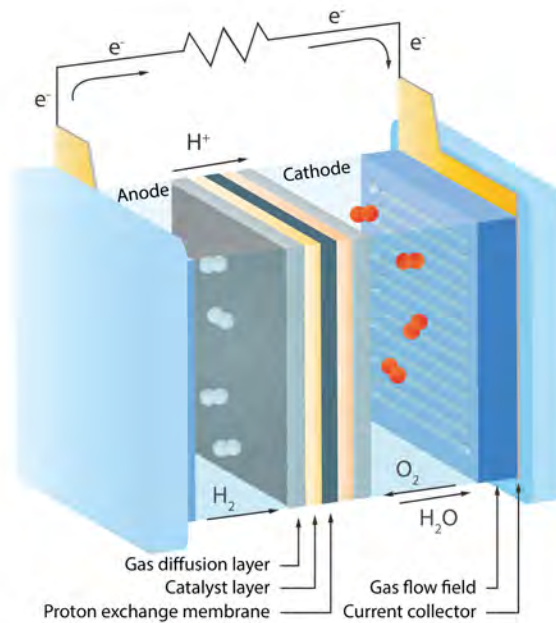


Figure 3.1: Structure and components of a single cell proton exchange membrane fuel cell.

3.2.1 Proton Exchange Membrane

The proton exchange membrane (PEM), also known as a polymer electrolyte membrane, sits in the middle of the fuel cell, between the anode and cathode electrodes. The PEM physically separates the anode from the cathode, and these three components together form what is known as the catalyst-coated membrane (CCM). The primary function of a PEM is to act as a solid electrolyte, conducting protons between the anodic and cathodic reactions, while being electrically insulating, thus forcing electrons to move through an external circuit. Moreover, the PEM acts as a physical barrier that prevents hydrogen and oxygen to react directly with each other which would lead to losses of useful fuel. The PEM must also be able to tolerate the harsh environments of the fuel cell. Thus, an effective PEM should exhibit high proton conductivity, low gas permeability, high electrical resistance, and good thermal, mechanical, and chemical stability [105–107].

The PEM is composed of an ionomer, which is a type of polymer with ion-conducting properties. Nafion has long been the industry standard ionomer for PEMFCs and was first synthesised by Walther Grot in the 1960s [108]. Since then, Nafion derivatives and similar short-chain ionomers such as Flemion, Aquivion, Hyflon and GORE-SELECT have entered the market as well [109–114]. Nafion is a fluoropolymer-copolymer based on sulfonated tetrafluoro-

ethylene (Figure 3.2 a). The backbone of Nafion is polytetrafluoroethylene, more commonly known as PTFE, which gives Nafion excellent chemical and oxidative resistance thanks to the strong bond between carbon and fluorine atoms [115]. Furthermore, PTFE is highly hydrophobic, which is favourable for removing water from the membrane. To provide ion conductivity, sulfonic side chains (SO_3^-) are added to the backbone, making it a perfluorinated sulfonic acid (PFSA) polymer. These sulfonic groups attract H^+ ions and are highly hydrophilic, which promotes water adsorption within the Nafion. As a result, Nafion can absorb up to 50% of its dry weight in water [105, 116]. The hydrophobic backbone together with the hydrophilic side chains form distinct phase-separated areas in the ionomers, creating water channels throughout the membrane, see Figure 3.2b. In these hydrated regions, the bond between the H^+ ions and the SO_3^- groups is weak, allowing good mobility of the ions. The ions move through the ionomer primarily through the vehicle diffusion mechanism, where ions ‘hitch-hike’ with cluster of water molecules, or via the faster Grotthuss mechanism, where H^+ ions can ‘jump’ between water molecules [117, 118], contributing to the good ion-conductive properties of Nafion when wet [116].

Another important aspect of the PEM is the thickness. To maximise the overall fuel cell volume to power ratio and improve ion conductivity, the trend has been to move toward thinner and thinner membranes [114]. However, the thinner the membrane, the more gas cross-over will occur [119–121]. In particular, hydrogen gas is difficult to prevent from permeating through the membrane, as it is the smallest and lightest molecule. Gas crossover leads to voltage losses and increases the degradation of the PEM. These issues are discussed in more detail in Section 3.4.1 and Section 3.5. Furthermore, the membrane needs to have good mechanical stability. When designing a membrane, the thickness must be a compromise between these requirements mentioned above. Although thinner membranes have better proton conductivity, they have less structural integrity and higher rates of hydrogen crossover. Nafion membranes are typically around 100–200 μm [122], although versions as thin as 25 μm are also available on the market [123]. To allow for thinner and more mechanically stable membranes, other PFSA membranes have been developed where they incorporate a reinforcement of expanded PTFE (ePTFE) for structural support, infused with PFSA for proton conductivity [53, 114, 124], such as GORE-SELECT membranes [113]. These types of membranes can be less than 10 μm thick, while still maintaining good mechanical properties as the ePTFE reinforcement prevents in-plane swelling and crack propagation during humidity cycling [16, 113, 124]. Due to better ion conductivity, thinner membranes performs better at beginning of life compared to thicker membranes, although they may suffer worse from degradation [124]. Thin membranes also facilitate the diffusion of water through the membrane, which, under certain conditions, allows self-humidification systems without external humidification [102, 125].

Although Nafion and similar PFSA ionomers have been the leading ionomers for proton exchange membranes and have reasonable tolerance to current

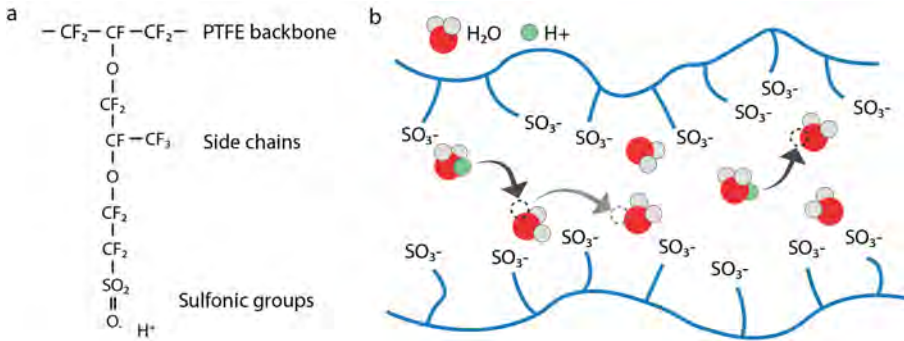


Figure 3.2: a) Chemical structure of Nafion. b) Illustration of protons moving through the water channels in the Nafion membrane via the Grotthuss mechanism. These water channels are formed due to the hydrophilic side chains of Nafion.

operating conditions, ongoing efforts to increase the operating temperature of PEMFC lead to the need to develop new membrane alternatives [126–128]. Currently, PEMFCs are typically operated at around or below 80°C . However, to improve kinetics, help water management, reduce the need for cooling systems, and increase the tolerance to CO poisoning, efforts are currently being made to increase the operating temperature to 100°C or above [105, 126, 129, 130]. Nafion and similar PFSA membranes require high levels of hydration to maintain their proton-conducting properties [107]. At high operating temperatures, the membrane can dry out quickly if operated at low RH, causing its ion-conductive capabilities to decrease by several orders of magnitude and severely limit performance [105, 107, 127, 128, 131]. Some of the issues with losing water through evaporation can be avoided by operating the fuel cell at elevated pressures. Furthermore, Nafion and other PFSA polymers have been reported to have glass transition temperature around 110°C and 120°C [132, 133], and Nafion's side-chains start to change structure and relax at around 100°C [134], which can lead to mechanical strength and durability issues if these membranes are operated at elevated temperatures.

Finding alternative membrane materials that could operate at higher temperatures and lower humidity would help simplify the design of the system, as control over the operating conditions of the system would not have to be as stringent. Furthermore, at lower humidity, the water management becomes easier, as the balance of under-humidification of the membrane and the risk of reducing the ion conductivity, and over-humidification of the MEA and risk flooding of the cell becomes easier if the fuel cell is not operated close to the dew point. Although there are versions of PEMFCs that operate at higher temperatures ($>130^\circ\text{C}$), they typically use membranes made of polybenzimidazole polymer doped with phosphoric acid [129]. High-temperature PEMFCs based on these types of membranes have excellent thermal stability, good CO tolerance, and can operate at low to no humidity, but they have

poor ion conductivity below circa 130 °C and low power densities compared to low-temperature PEMFCs [129], and tend to leak acid [135]. Furthermore, they tend to have very long start-up times as the system has to be slowly heated up to operation temperature before use. Consequently, these types of high-temperature PEMFCs are not preferred for, e.g., automotive applications. This creates a gap in the intermediate temperature range, between 80 °C and 120 °C, where suitable ion-conductive materials with both high conductivity and durability are lacking.

Another considerable issue with PFSA membranes is that they are part of a group of chemicals known as per- and polyfluoroalkyl substances (PFAS). The European Union is currently discussing plans to ban the use of PFAS due to their potential toxicity and negative effects on human health [136, 137]. PFAS are notorious for their persistent nature with long life-cycles in the environment as they are not biodegradable, their tendency to bio-accumulate in organisms, and their many adverse effects on human health [137–139]. Consequently, membranes based on PFAS materials face the risk of being phased out in the near future, and alternatives to PFSA-based membranes are needed. Preferably, a replacement material should have both good performance and better durability in a wider range of conditions than PFSA-based membranes, i.e., in a broader temperature range and lower humidity. However, achieving all of these targets at the same time is a considerable challenge.

Alternatives to fluorinated membranes are being researched, although replacements are not trivial because of the stringent requirements of the membranes in terms of, e.g., durability, ion conductivity, and mechanical properties. Sulphonated hydrocarbon-based membranes are among the top candidates for PFAS-free membranes, and have shown promising performance during PEMFC operation. In addition to being PFAS free, hydrocarbon membranes might offer higher thermal stability and lower gas crossover compared to PTFE-based membranes. Currently, few hydrocarbon-based MEAs have been successfully introduced to the market and many hydrocarbon-based MEAs in the literature have shown a poor peak power output compared to PFSA-based MEAs even when PFSA is introduced into the ionomer to improve conductivity [140]. Furthermore, the hydrocarbon based ionomers still require high hydration levels to sustain adequate ion conductivity [141]. Recent advances in the field have led to fully hydrocarbon-based MEAs with performance comparable to state-of-the-art PFSA MEAs under automotive conditions at 80 °C and high RH, and even outperform PFSA MEAs in terms of maximum power output at 100 °C [142, 143]. However, hydrocarbon-based CLs have been reported to be less porous and more dense than equivalent Nafion-based CLs [141], and recent studies of commercially available HC ionomers suggest that they have an ionomer/Pt ratio for optimal gas transport that is lower than that of PFSA ionomers, leading to an increase in proton resistance and lower utilisation of Pt, especially at low humidity [143, 144]. This reduced utilisation of platinum stands in contrast to the goal of maximising the available surface area and minimising the use of platinum.

3.2.2 Catalytic Layers

The actual chemical reactions in the PEMFC take place on the anode and cathode electrodes, also known as the catalyst layers (CLs). A major role of the CLs is to provide a large amount of active sites per geometric surface area of the fuel cell, to facilitate large current densities. Currently, the catalyst commonly used for both the anodic and cathodic electrode in PEMFCs is Pt nanoparticles on a carbon support (Pt/C) or other carbon-supported Pt-metal alloys [145–148]. Typically, fine Pt particles (~ 5 nm in diameter) are dispersed on supporting carbon particles (~ 50 nm in diameter), as shown in Figure 3.3. The catalyst layers are relatively thin, with the cathode of state-of-the-art MEAs being around $10\ \mu\text{m}$ thick and the anode being as thin as $1\ \mu\text{m}$.

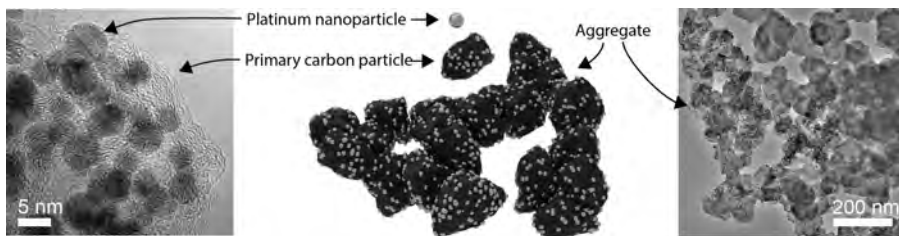


Figure 3.3: Illustration and electron microscopy images of carbon supported platinum catalyst particles. Pt nanoparticles are evenly distributed across the surface of primary carbon particles. These carbon particles form aggregates, creating a porous framework.

Pt or Pt-alloys act as catalysts for both the HOR on the anode and the ORR on the cathode, thereby facilitating high current densities at low overpotentials. The reason why Pt is currently the industry standard in PEMFC and has a good activity for both ORR and HOR, becomes clear when considering the binding energy between Pt and the intermediate species involved in these reactions. For ORR, the binding energy of Pt is just $0.1\ \text{eV}$ below the estimated optimal value, shown in the Volcano plot in Figure 2.2b, and is the best catalyst out of all pure metals [46].

However, while Pt has good performance, much effort in fuel cell research is focused on finding alternative catalyst materials. Pt is a scarce resource and an expensive noble metal. In large-scale production, it is predicted that the raw cost of Pt will account for up to 40% of the production cost [32]. Thus, in order to reduce the production cost and reach the cost targets, the use of Pt needs to be minimised to the extent possible without greatly affecting the performance or lifetime of the fuel cell. Moreover, even though Pt has high activity for both HOR and ORR and relatively good stability under harsh conditions of the fuel cell [89, 145], the highly corrosive environment in the PEMFC means even Pt suffers from degradation [149]. Finding a suitable replacement for Pt is challenging. A viable alternative must not only be more cost-effective, but also exhibit high activity and stability in the harsh and dynamic conditions inherent in PEMFCs.

Efforts to reduce the Pt loading often focus on alloying or doping Pt with various elements. For example, suggested Pt alloys include transition metals such as nickel, chromium, iron and cobalt, and lanthanide metals such as lanthanum, cerium, samarium, gadolinium, terbium, dysprosium, thulium, or calcium, of which a Pt-terbium alloy showed up to six times higher performance than pure Pt [46, 48, 52, 147, 150]. However, many of these have shown poor stability and tend to dealloy [150–153]. Alloys with rare earth metals, such as scandium, hafnium, and yttrium, are suggested to possibly have better stability due to low heat of formation, where alloying with yttrium has been shown to increase activity by up to ten times compared to pure Pt [47–50].

Another approach to decrease the use of Pt involves creating nanostructured Pt particles to maximise the number of active sites per mass [40, 154]. Pt particles with well-controlled shapes, such as octahedrons, and other shape- and structure-controlled Pt or Pt-alloy nanoparticles, such as core shell particles, nanocages and nanoframes, have been produced, showing increased activities compared to common Pt [41–45, 154, 155].

While many novel catalysts show highly promising results in laboratory settings, these results are often hard to upscale or replicate in fuel cell testing. For example, while Brown et al. found that sputtered Pt_3Y films had a seven-fold performance increase over pure Pt in half-cell testing [156], the same Pt_3Y thin films showed only a two-fold increase in activity compared to Pt films when measured in a real fuel cell [157]. One of the more successful attempts of Pt-alloys is Pt_xCo , which has been used in commercial settings [102] and has been shown to both perform better than pure Pt, and to have good stability under relevant application conditions [51, 52]. As for shape-controlled nanoparticles, they tend to be unstable in the operating conditions of PEMFCs, and revert back to more spherical structures [154].

When choosing the size of the catalyst particles, two main aspects have to be taken into account, namely stability and activity. Smaller particles allow for a higher utilisation of the material, due to a larger surface area per gram and, thus, typically exhibit higher mass activity. This is a desirable quality especially for expensive catalyst materials, as it minimises the amount of catalyst needed. For Pt nanoparticles, the highest mass activity for the ORR is achieved somewhere around 2–3 nm [158, 159]. However, small particles are unstable and suffer more from degradation, dissolution, and performance decline [160–162], and therefore the lifetime of the fuel cell is compromised. Larger Pt particles, on the other hand, are more stable but have lower mass activity. Hence, particle size must be a trade-off between activity and stability. The optimal size for Pt particles has been suggested to be around 2–5 nm [149, 163]. However, for Pt metal alloys, the optimal size might be different. For example, Pt_3Co particles have been indicated to have a good balance between stability and mass activity at around 8 nm [52], and studies on Pt_xY catalyst suggest that the highest ORR mass activity for Pt_xY nanoparticles is achieved somewhere around 10 nm [158], although the stability of those particles under real fuel cell operation is still unclear.

The Pt nanoparticles are distributed on a catalyst support material, which plays a crucial role in facilitating the distribution, utilisation and stability of Pt particles within the CL [147, 148, 164]. This support material ensures optimal dispersion of Pt particles and maximises the available Pt surface area [164]. This is vital given the high cost of Pt, and ensures that as much Pt as possible is available for electrochemical reactions. Additionally, the support limits Pt particle agglomeration and sintering, while also establishing electrical connection within the CL [164]. The support material should be inexpensive, corrosion resistant under relevant operating conditions, and readily available, with carbon-based materials typically fulfilling this role [164]. Ideally, the support should have a high surface-to-volume ratio to allow for a high loading of platinum per electrode surface area. For example, KetjenBlack carbon black has a surface area of more than $1200 \text{ m}^2 \text{ g}^{-1}$ [165]. KetjenBlack is a type of carbon black, which is a commonly used support material. Carbon black consists of primary particles approximately 30–50 nm in diameter, which form aggregates, as depicted in Figure 3.3. These aggregates form even larger agglomerates, creating a highly porous structure that allows the gases to reach the reaction sites on the Pt particles. Other types of carbon support are also being used and researched, such as activated carbon, graphitised carbon, carbon nanotubes, and carbon nanofibers [147, 148].

To provide proton conductivity to the reaction sites, the Pt/C catalyst is covered with an ionomer, the same type of material used in the PEM. The ionomer also acts as a polymer binder, binding the catalyst layer together. Although the ionomer is vital for providing protons to the reaction site, it also hinders the access to oxygen [166]. Thus, a compromise between proton conductivity and oxygen access must be reached when deciding on the ionomer loading of the catalyst layer [167, 168], and for Nafion, the optimal loading has been reported to be around 30%wt [169, 170], with an optimal ionomer/carbon mass ratio suggested to be between 0.6 and 1 [170–172].

The ORR at the fuel cell cathode can occur in the presence of oxygen, electrons, and protons. This occurs on specific sites where the pores for gas transport, carbon support for electrical conduction, and ionomer for proton conduction meet at the Pt catalyst. If the catalyst layer is sufficiently humidified, water can partially act as an ion conductor at sites otherwise not in contact with the ionomer [173]. These sites at the triple phase boundary are illustrated in Figure 3.4. The loss of any of the phases in the triple-phase boundary inhibits the catalytic reaction. For example, if the porosity of the catalyst layer is reduced as a result of degradation of the carbon support, the triple phase boundary cannot be sufficiently supplied with gases, thus limiting performance. Similarly, if the contact between the Pt particles and the carbon support or the ionomer is compromised, fuel cell performance will suffer as a result of lack of electronic and ion conductivity.

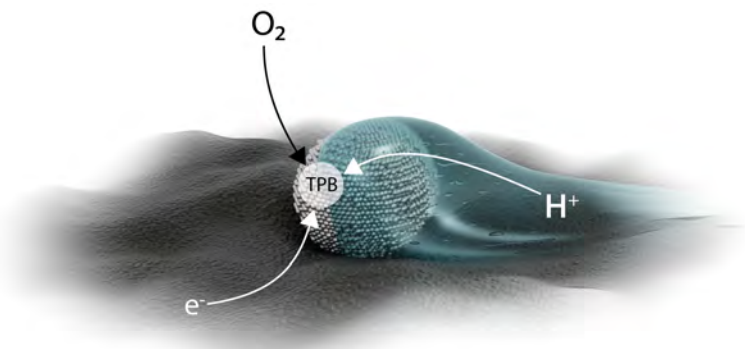


Figure 3.4: Illustration of the triple phase boundary where the electron conductor (carbon support), the ion conductor (ionomer) and the ‘porous’ gas phase meet on the catalyst.

3.2.3 Gas Diffusion Layers

The gas diffusion layers (GDLs) are placed on either side of the CLs and serve as an interface between the CLs and the flow fields that conducts electricity, facilitates the uniform distribution of gases over the catalyst layers, helps with water management and heat dissipation, and provide some mechanical stability [174–176]. To achieve this, GDLs are constructed from porous conductive materials such as carbon paper (nonwoven carbon fibres pressed into a sheet), or carbon cloth and are often treated with PTFE to enhance their hydrophobic properties and facilitate the removal of water [174–179]. Carbon-based GDLs are preferred because of their good electrical conductivity, durability, and gas permeability. The GDL is often coated with a microporous layer (MPL), which is a carbon black layer treated with PTFE [177, 178]. Figure 3.5 shows the structure of a GDL made of carbon paper with an MPL. The hydrophobic nature of the MPL facilitates the removal of water, and the microscopic structure improves the electrical contact between the CL and the rest of the GDL, and helps to evenly distribute gases over the CL [174, 177, 179].

Careful water management is important for the function of the MEA. If the membrane becomes too dry, the proton conductivity will suffer and the membrane risk degrading. Too much water, on the other hand, will cause flooding and block pores, leading to limitations in mass transport [174, 178]. At high current densities, flooding of the GDL and CL is a major contributor to mass transport limitations. The flooding problem is most prevalent on the cathode side, as that is where water is produced in the cell [178]. Furthermore, the thickness of GDLs can greatly affect fuel cell performance. A GDL that

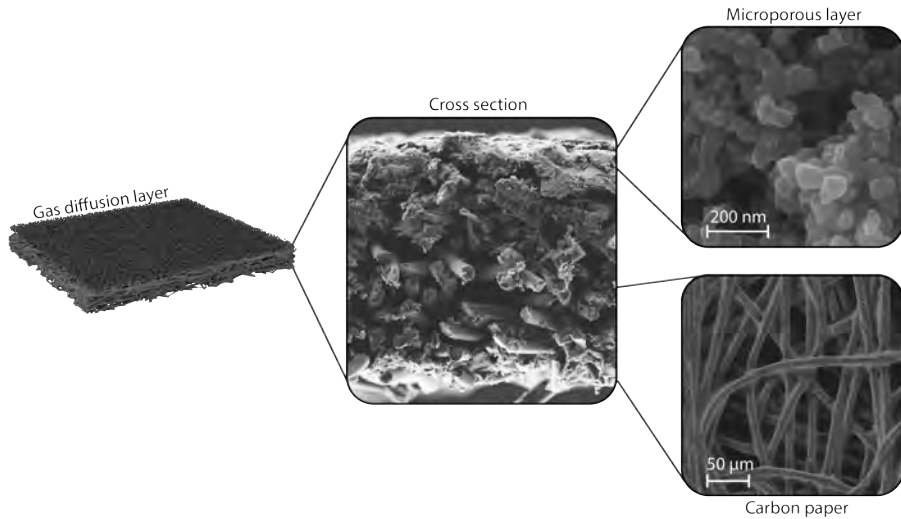


Figure 3.5: Typical construction of a GDL. The GDL is made out of carbon fibre paper, infused with PTFE for increased hydrophobicity, and coated with a micro-porous layer.

is too thick leads to excessive losses from ohmic resistance and gas transport resistance within the GDL, whereas too thin GDLs have issues with nonuniform distribution of water and oxygen over the catalyst layer. An optimal thickness of the GDL has been reported to be around 200 μm [180, 181].

3.2.4 Membrane Electrode Assemblies

A membrane electrode assembly (MEA) is formed by mounting a GDL on either side of the CCM, with the MPLs facing the CLs, together with supporting gaskets, see Figure 3.6a. An alternative approach to construct an MEA is to deposit the CL directly onto the GDL, forming a gas diffusion electrode (GDE), also known as a catalyst-coated substrate (CCS), and then hot-pressing two CCSs together with a PEM in-between to form a CCS-MEA. Typically, MEAs constructed from CCMs will have better performance than MEAs based on CCSs, partly due to enhanced proton conductivity due to better contact between the CL and the membrane, and CCM-based MEAs have shown an increased power density for the same Pt loading [173, 182]. The full MEA with all its layers is typically around 200–500 μm thick.

3.2.5 Flow-Fields and Current Collectors

Part of the supporting structures include the flow fields and the current collectors. The flow fields are placed next to the GDLs and serve to distribute fuel to both the anode and the cathode. The flow fields also provide electrical contact between the MEA and the current collectors located on either side of the flow field, see Figure 3.5b. An effective distribution of gases is achieved by

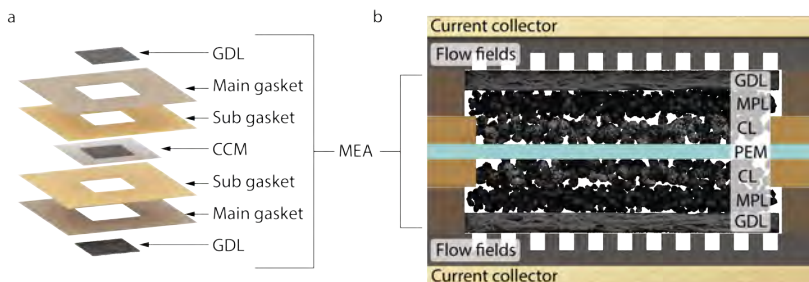


Figure 3.6: a) Construction of an MEA. A GDL is placed on either side of a catalyst coated membrane (CCM), with the MPL facing the CL. The assembly is held in place with the help of gaskets, that also serves to seal in the gases. b) Cross-section of an assembled single cell fuel cell.

well-designed flow-field patterns. Common flow field patterns include serpentine fields, parallel channels, and grid-type patterns, each offering slightly different properties with respect to, e.g., gas distribution, pressure drop, and water management [183, 184]. Poor flow field design can lead to inadequate O_2 or H_2 distribution over the catalytic layers, and promote water accumulation within the GDL and CL, thus blocking gas transport.

Furthermore, the flow-fields must be electrically conductive, allow for heat transport, be chemically and mechanically stable, be gas tight, have low weight and volume, and be cost effective and easy to manufacture [184, 185]. Flow fields are commonly made out of graphite, or stainless steel [184]. Although stainless steel plates have good conductive properties, are easy to mass produce and can be made very thin, they tend to corrode [57, 186]. Graphite, on the other hand, has excellent corrosion resistance, but is harder to mass produce, is more brittle, and needs to be made thicker to have adequate mechanical durability [186]. The flow fields are in contact with the current collectors, to which the external circuit is connected.

To achieve higher voltages than can be achieved in one single fuel cell (i.e., >1 V), several single cells are connected in series, forming a fuel cell stack. In a fuel cell stack, multiple individual cell assemblies, each composed of its own MEA, are stacked together end to end so that the anode of one cell connects to the cathode of the neighbouring cell. The cells are separated with bipolar plates, which serve as flow fields for both the anode of one cell and the cathode of the next. Modern bipolar plates are around 0.5–1 mm in height, and together with the around 500 μm thick MEA, each cell in a fuel cell stack is less than 2 mm thick. In all, the bipolar plates constitutes one of the larger contributors to both the stack weight, stack thickness, and production cost. The total voltage of the stack is the sum of the voltage of each individual cell, while the current output of the stack is determined by the surface area of the individual MEAs used.

3.2.6 Humidification

The performance of the PEMFC is strongly related to the humidity levels in the cell [187, 188]. Water plays a crucial role in facilitating the conductivity of protons through the membrane and the ionomer, as well as in transferring protons to platinum areas that may not have sufficient contact with the ionomer. Proper water management in a fuel cell is a careful balance between water production and water removal. Water is generated at the cathode at a rate proportional to the current by

$$n_{\text{H}_2\text{O}} = \frac{I}{2F}, \quad (3.4)$$

where $n_{\text{H}_2\text{O}}$ is the number of moles of water produced per second, I is the current and F is Faraday's constant. Thus, at high current densities, water production can be significant, leading to a risk of flooding if water removal does not match the production rate [178, 189]. Flooded catalyst layers can result in pore blockage, impeding mass transport, and cause a considerable voltage drop. Conversely, no water is produced at the anode. Together with water evaporation due to elevated temperatures, and the tendency of protons to drag water with them while they migrate through the membrane from the anode to the cathode through a phenomenon known as electro-osmotic drag, the anode is susceptible to drying out [106, 190]. However, this tendency is somewhat mitigated by the diffusion of water back from the cathode to the anode, driven by the water concentration gradient. Dry catalyst layers, and in particular a dry membrane, leads to issues with proton conductivity.

Humidity is often expressed in terms of relative humidity (RH), which relates the water vapour pressure, P_{W} , to the water saturation pressure, P_{sat} , at the specific temperature,

$$\text{RH} = \frac{P_{\text{W}}}{P_{\text{sat}}}. \quad (3.5)$$

RH is highly dependent on temperature and pressure, see Figure 3.7. At higher temperatures, the water saturation pressure increases, and thus the RH of a given water vapour pressure decreases. For example, if a gas at 20 °C and with 100% RH is heated to 80 °C without adding any more water, the new RH will only be a minuscule 2.4%, which is extremely drying for the membrane.

To keep the humidity within the acceptable operating range, humidifiers are typically used to wet the ingoing gases. In practical applications, the system can self-supply with water by recirculating internally produced water from the cathode exhaust [102, 192]. With some clever design choices, the system can even be completely internally self-humidified, i.e., not having any water supplied with the ingoing gases and only relying on internal production and diffusion of water. This is possible by, for example, operating at lower temperatures, low flows, and high pressures to reduce excess water evaporation through the gases,

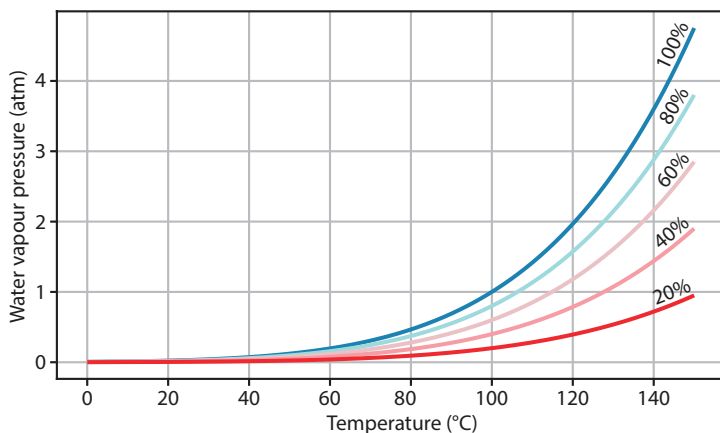


Figure 3.7: Water vapour pressure versus temperature, with contour lines representing RH levels at 20%, 40%, 60%, 80%, and 100%. The plot was constructed using the Antoine equation [191].

utilising counter-flow of anode and cathode gases, and using thin membranes [102, 125, 189, 193]. An RH value between 60–70% has been suggested to provide optimal performance for Nafion membranes [194], although it may lead to an increased rate of membrane degradation compared to operating at either 100% or 20% RH [195]. Still, many research protocols call for a high humidification of up to 100% RH, although for realistic automotive applications lower humidification levels <100% RH are likely more practical, as they minimize the need for external humidification and reduce the risk of flooding.

3.2.7 Additional Fuel Cell Stack Components

The discussion above regarding fuel cell components is certainly not exhaustive, and several other components are vital for the overall function and control of fuel cell systems. Additional components worth mentioning include gaskets, which are used in MEA to prevent gas leakages from the porous edges of the CL and GDL, as well as to prevent fuel crossover from the sides of the CL and electrical shortcuts while controlling the compression rate of the GDLs [196]. Furthermore, proper gas supply and control are essential for fuel cell operation, including recirculating excess fuel from the exhaust. Furthermore, since fuel cells are often operated under elevated pressures to increase activity, air compressors are frequently needed. The end plates of the fuel cell/stack serve to hold everything together and provide uniform pressure, which is critical for optimal compression of the GDLs and to reduce contact resistance [197].

Moreover, the fuel cell also needs some kind of heat management system [198]. In small-scale research systems, the fuel cell itself and the gas pipes often need to be heated to reach the desired operating temperature, mimicking realistic operating conditions. However, in real applications, the fuel cell will

produce much heat by itself during the catalytic conversions, which leads to the need for cooling. For small systems, the cooling effect of reactant air flowing over the cathode and heat radiation can be enough [199]. For slightly larger systems, separate air channels can be used purely for cooling if the reactant air cannot remove heat quickly enough [199]. For systems greater than 10 kW, water cooling is generally preferred [200]. Water cooling is advantageous, when operating between 0 °C and 100 °C, due to its excellent heat removal capabilities, allowing for the use of smaller and more compact cooling systems [97]. Other coolants such as aromatic coolants and aliphatic coolants are favourable at higher temperature intervals [97].

3.3 ORR and HOR Reaction Pathways

In the acidic conditions of PEMFC, two reaction pathways for ORR have been identified [201]. Water is formed either via the two-step 2-electron pathway with intermediate hydrogen peroxide formation,

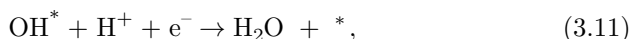


or via the direct 4-electron pathway

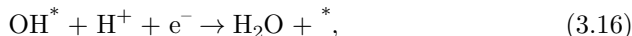


Due to the formation of hydrogen peroxide in the two-step pathway, there is a risk of hydrogen peroxide release, which is undesirable because hydrogen peroxide can damage the membrane. Due to its ability to form hydroxyl and peroxy radicals, hydrogen peroxide accelerates membrane degradation, and therefore the 4-electron pathway is preferred [202, 203].

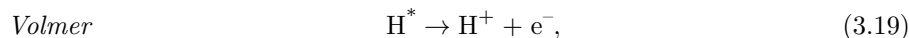
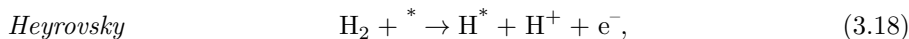
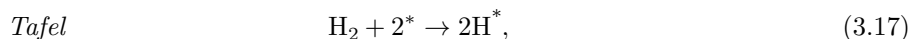
Nørskov et al. [46] have suggested two mechanisms for the 4-electron pathway. The first mechanism is called dissociative, where the oxygen dissociates on the surface before being hydrogenated;



where * denotes an active site on the catalyst surface, and the other mechanism is called associative, where O_2 react directly with H^+ on the surface;



In contrast to the complicated ORR, the HOR is a much simpler reaction, described by three possible steps [204],



where two of the steps described in Eqs. 3.17, 3.18 and 3.19 take place, either Tafel–Volmer or Heyrovsky–Volmer. Overall, the HOR is a very fast reaction with low overpotentials and high exchange current densities on good catalysts. For Pt, which is the commonly used catalyst for HOR in PEMFC, the exchange current density can be as high as $10 \times 10^{-1} \text{ A cm}^{-2}_{\text{Pt}}$ [205] (although the exact current density is a complicated value to measure, and reported values varies by orders of magnitude), and the contribution of the anode to the total cell overpotential and losses is negligible as long as the anode has enough Pt surface area, and don't suffer from, e.g., resistance or mass transport losses. In contrast, the ORR involves more electron transfers and intermediate steps than the HOR and has a much slower reaction rate, by several orders of magnitude, with an exchange current density for the ORR of the order of $10 \times 10^{-6} \text{ A cm}^{-2}_{\text{Pt}}$ [206]. To somewhat compensate for the low exchange current densities and large overpotentials at the cathode, the cathode typically have much higher loadings of Pt catalyst. For example, the Toyota Mirai have an anode Pt loading of around 0.05 mg cm^{-2} and a cathode Pt loading of around 0.315 mg cm^{-2} [207]. The large overpotential caused by the ORR leads to a large decrease in efficiency, and therefore most research on the topic of catalysts for fuel cells is focused on the ORR rather than the HOR. Even so, some improvements can still be made for the catalyst for the HOR, for example, by finding an alternative catalyst with a better tolerance for CO [208–210].

3.4 Performance Metrics and Efficiency Factors in PEMFCs

For real-life applications, some key fuel cell operating parameters are used to compare fuel cells with other competitive technologies. For the electrodes,

the current density j (current per unit area) is one of the main parameters. For ease of comparison between fuel cell systems of different dimensions and design, the current is usually normalised, either by geometric surface area (j_{geo} [$\text{A cm}_{\text{geo}}^{-2}$]), electrochemical surface area (ECSA, j_{ECSA} [$\text{A cm}_{\text{ECSA}}^{-2}$]) or by catalyst mass (j_{mass} [$\text{A g}_{\text{catalyst}}^{-1}$]), and the current is often compared at a specific voltage, such as 0.6 or 0.7 V. Figures of merit such as power per area, specific power (kW kg^{-1}) and power density (kW m^{-3}) are important when comparing alternative power generation technologies. Other important parameters for successful commercialisation include the cost of production, cost per kW, efficiency, and lifetime. Table 3.2 shows the targets for some of these performance parameters set by the DOE.

Characteristic	80 kW system	Class 8 Long-Haul Trucks
	2025 targets	Ultimate target
<i>Cost</i>	35 \$ kW ⁻¹	60 \$ kW ⁻¹
<i>Peak efficiency</i>	65%	72%
<i>Lifetime</i>	8 000 h	30 000 h
<i>Catalyst loading</i>	≤ 0.1 mg _{Pt} cm ⁻²	0.25 mg _{Pt} cm ⁻²

Table 3.2: Key technical targets for 80 kW fuel cell systems and fuel cells for Class 8 Long-Haul Trucks, set by DOE. Data from [35, 91].

3.4.1 Cell Voltage and Efficiency

The cell voltage and efficiency of a fuel cell depend on several variables. Firstly, the theoretical maximum cell voltage is given by the thermodynamics of water formation. Using Eq. 2.8, and isolating E , gives the the maximum theoretical cell voltage that can be achieved by a specific electrochemical reaction as a function of the change in Gibbs free energy,

$$E = -\frac{\Delta G}{nF}. \quad (3.20)$$

Quantity	Reactants		Product	Difference
	(kJ mol ⁻¹)		(kJ mol ⁻¹)	(kJ mol ⁻¹)
	H ₂	O ₂	H ₂ O	Δ
G_{f}°	0	0	-237.14	-237.14
H_{f}° (LHV)	0	0	-241.83	-241.83
H_{f}° (HHV)	0	0	-285.82	-285.82

Table 3.3: Gibbs free energy of formation, G_{f}° , and enthalpy of formation, H_{f}° , at standard temperature and pressure for H₂, O₂ and H₂O using the lower heating value (LHV) and higher heating value (HHV) of the enthalpy of formation. Data from [211, 212].

At standard state (20 °C and 1 bar), the change in Gibbs free energy of formation of water (Eq. 3.1) is $\Delta G_{\text{f}}^{\circ} = -237.14 \text{ kJ mol}^{-1}$, see Table 3.3. Using Eq. 3.20 with $n = 2$ electrons, we get

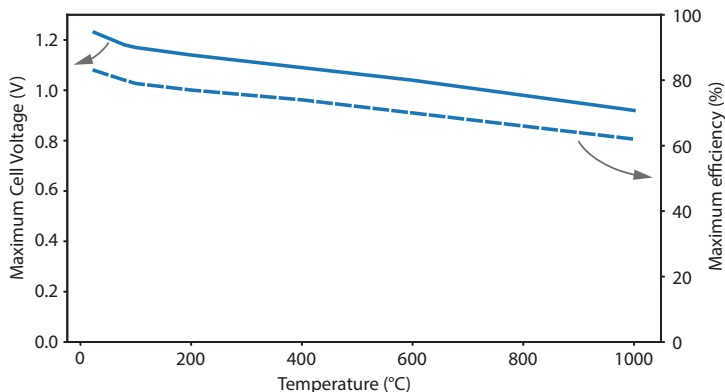


Figure 3.8: Theoretical maximum cell voltage (solid line) and efficiency (dashed line) at standard pressure at different temperatures. Data from [199].

$$E_0 = -\frac{\Delta G_f^\circ}{nF} = 1.23 \text{ V}, \quad (3.21)$$

which is the theoretical maximum cell voltage that can be achieved at standard state when no net current is produced. The change in Gibbs free energy ΔG_f at higher temperatures than in the standard state will be lower. For example, at 80 °C and 1 bar, the maximum cell voltage is 1.18 V, and at 100 °C and 1 bar, the maximum voltage would be 1.17 V. Figure 3.8 shows the maximum cell voltage and efficiency at standard pressure between 20–1000 °C.

Thermodynamics also gives the maximum thermodynamical efficiency for a PEMFC. The efficiency of an electrochemical reaction is the ratio between the useful energy, ΔG and the total energy, given by the change in enthalpy, ΔH . The change in enthalpy for the formation of water is ambiguous, as it depends on whether the product is steam or liquid water, giving the lower heating value (LHV) or the higher heating value (HHV), respectively (see Table 3.3). Using HHV, that is, assuming that the product is liquid water, the change in enthalpy for the formation of water under standard conditions is $\Delta H_f^\circ = -285.82 \text{ kJ mol}^{-1}$, which results in a maximum efficiency of

$$\epsilon = \frac{\Delta G_f^\circ}{\Delta H_f^\circ} = \frac{-237.14}{-285.82} = 83\%, \quad (3.22)$$

at standard state. This can be compared to the maximum thermodynamic efficiency of a combustion engine, which is limited by the Carnot efficiency. A combustion engine operating at $T_H = 400 \text{ °C}$ with an exhaust temperature of $T_C = 50 \text{ °C}$, has a maximum efficiency of

$$\epsilon_{\text{Carnot}} = \frac{T_{\text{H}} - T_{\text{C}}}{T_{\text{H}}} = 52\%, \quad (3.23)$$

but a real engine will have a lower efficiency due to, e.g., friction and heat losses. Thus, the thermal efficiency of a typical diesel engine ranges between 30–35%. Combustion engines can approach the theoretical efficiency of electrochemical processes, especially at higher operating temperatures. For instance, at temperatures around 700 °C, the Carnot efficiency of a combustion engine can approach that of a PEMFC. Despite this, electrochemical processes generally maintain higher efficiencies at a broader range of temperatures, as they do not rely on high-temperature thermal gradients to operate, and avoid significant energy losses due to mechanical friction and exhaust heat.

3.4.1.1 Voltage Losses

However, a real fuel cell system will work at less than 83% efficiency and operate at voltages below 1.23 V, typically between circa 0.6–1.0 V. The thermodynamic efficiency of a fuel cell operating at a cell voltage E_{cell} lower than the theoretical maximum can be described by

$$\epsilon_{\text{real}} = 0.83 \frac{E_{\text{cell}}}{E_0}. \quad (3.24)$$

This loss of efficiency is caused by overpotentials. The real cell voltage E_{cell} can be described by

$$E_{\text{cell}} = E_0 - \eta_{\text{kinetic}} - \eta_{\text{ohmic}} - \eta_{\text{concentration}}, \quad (3.25)$$

where E_0 is the thermodynamic equilibrium cell voltage at no current, η_{kinetic} is the kinetic overpotential, η_{ohmic} is the ohmic overpotential and $\eta_{\text{concentration}}$ is the mass transfer overpotential. Different type of overpotentials will be dominant in the low, medium and high current regions, see Figure 3.9.

Open Circuit Voltage An ideal membrane should not allow for any gases to permeate through it. However, in reality, there will always be some amount of gas that cross over through the membrane. In particular, this issue becomes more pronounced as the trend for state-of-the-art membranes is to make them thinner and thinner [124]. Small amounts of H_2 cross the anode to the cathode through the membrane. This leads to a mixed potential at the cathode, where ORR and HOR now occur at the same electrode, and the open-circuit voltage (OCV, the cell voltage at which no current flows through the cell) decreases until the current from ORR matches the current from HOR due to hydrogen crossover. This results in a noticeable voltage drop of the OCV of around 200–250 mV from the theoretical value of 1.23 V_{RHE} down to slightly below 1 V_{RHE} [121]. OCV losses due to H_2 crossover are worse for thinner membranes

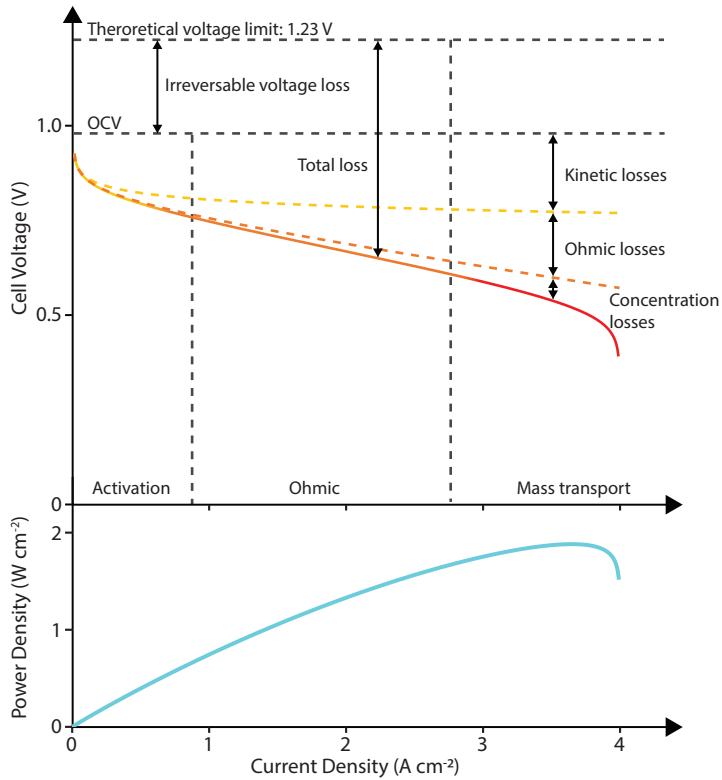


Figure 3.9: Theoretical polarisation curve at 20 °C based, on Eqs. 3.25–3.28, and corresponding power density. The polarisation curves were constructed assuming an OCV of 250 mV below the theoretical E_0 , a Tafel slope (b) of 59 mV dec^{-1} , exchange current density ($i_{0,\text{OOR}}$) of $10 \times 10^{-6} \text{ A cm}^{-2}$, a catalyst area of $100 \text{ cm}_{\text{Pt}}^2 \text{ cm}_{\text{geo}}^{-2}$, a cell resistance of $25 \text{ m}\Omega \text{ cm}^2$ and a limiting current density (i_{lim}) of 4 A cm^{-2} .

[121, 124], as hydrogen crossover rates increase. H_2 can react directly with O_2 on the cathode, forming water and releasing excess heat, which can lead to local hotspots leading to membrane thinning and pinhole formation, which in turn can further increase hydrogen crossover rates. The mixed potential that decides the OCV is also partly influenced by the mixed potential of the partially oxidised surface of the Pt/PtO catalyst [121].

Activation Losses At low currents, the voltage loss is dominated by kinetic losses. Slow kinetics and high activation barriers to initiate the ORR reaction on the cathode need to be overcome by applying higher overpotentials, which leads to a highly nonlinear loss of voltage in the low-current region. Kinetic losses, also called activation losses, are described by the Tafel equation.

$$\eta_{\text{kinetic}} = b \log \frac{i}{i_0}, \quad (3.26)$$

where $b = RT/\alpha nF$ is the Tafel slope, i_0 is the exchange current density, and i is the cell current density. Activation losses are mainly governed by the kinetics of the catalyst material and the catalyst loading. Better-designed catalysts, with larger exchange current densities i_0 , help improve performance in the kinetic region, and degradation of the catalyst, e.g., by loss of surface area leading to a decrease in i_0 , leads to higher kinetic losses. The cathode typically contributes substantially more to the activation overpotential and voltage loss than the anode at a given current density, as the HOR exchange current density $i_{0,\text{HOR}} \approx 10 \times 10^{-1} \text{ A cm}^{-2}$ is many orders of magnitude higher than the ORR exchange current density $i_{0,\text{ORR}} \approx 10 \times 10^{-6} \text{ A cm}^{-2}$ [205, 206], see Figure 3.10.

Ohmic Losses Once the kinetic barriers have been overcome, the drop in voltage will mainly come from internal resistance in the fuel cell due to both ionic resistance and electronic resistance. This ohmic resistance regime is characterised by a linear dependence between the voltage and current according to Ohm's law,

$$\eta_{\text{ohmic}} = iR, \quad (3.27)$$

where R is the cell resistance. The ionic resistance comes from the movement of H^+ throughout the membrane and the ionomer, and will be affected by the type of ionomer used, the thickness of the membrane and the humidification levels. Electronic resistance comes from the internal resistance in the CL and the GDL, and the contact resistance at the interfaces between each component of the fuel cell. Typically, the ionic resistance is much larger and more influential than the electronic resistance.

Mass Transport and Concentration Losses Mass transport losses in a fuel cell occur due to the challenges associated with transporting H_2 and O_2 within CLs and GDLs. The rate at which these reactants can diffuse through the GDL and CL to the reaction sites is inherently limited.

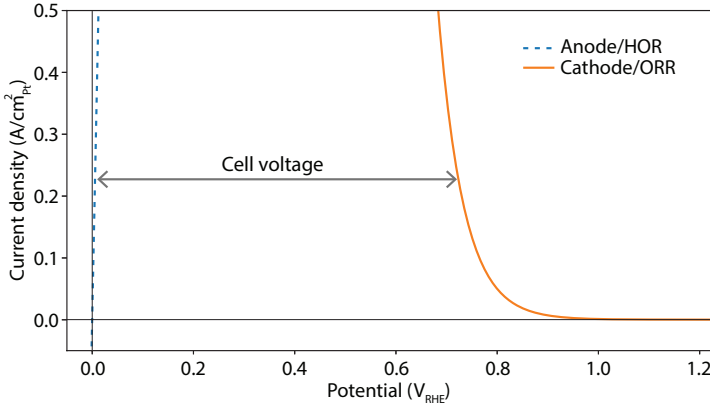


Figure 3.10: Overpotential contribution of the anode (hydrogen oxidation) and the cathode (oxygen reduction) on Pt at room temperature, based on the Tafel equation (Eq. 3.26), with $\alpha = 0.5$, $i_{0\text{HOR}} = 10 \times 10^{-1} \text{ A cm}_{\text{Pt}}^{-2}$ and $i_{0\text{ORR}} = 10 \times 10^{-6} \text{ A cm}_{\text{Pt}}^{-2}$. The resulting cell voltage is the difference between the anode and cathode potential. Due to the fast kinetics of the HOR on Pt, the overpotential contribution from the anode is negligible for any reasonable current densities.

Anode mass transport losses are generally minimal because H_2 diffuses relatively quickly through the GDL and CL. Additionally, the anode experiences fewer mass transport issues since water is transported away from it to the cathode via electro-osmotic drag, reducing the risk of flooding. In contrast, mass transport losses at the cathode are more significant, mainly due to the slower diffusivity of O_2 and the increased susceptibility to flooding. As O_2 is consumed, the partial pressure of O_2 decreases near the catalyst. This leads to a decrease in cell potential according to the Nernst equation (Eq. 2.12). This is particularly noticeable if the consumption of O_2 is large compared to the gas flow, as areas far from the inlet can be completely depleted of O_2 .

At very high current densities, the current reaches a limiting current, as the mass transport of reactants to the reaction site will be insufficient to replenish O_2 or H_2 , or the removal of water will be too slow. This issue is further exacerbated by the increased rate of water production at higher current densities, raising the risk of water blockage and worsening gas transport issues. Mass transport losses can be described as a function of the limiting current i_{lim} [213],

$$\eta_{\text{concentration}} = -\frac{RT}{nF} \ln \left(1 - \frac{i}{i_{\text{lim}}} \right). \quad (3.28)$$

An insufficient gas supply can lead to unnecessary mass transport limitations and local gas starvation. Hence, gases are typically supplied at an over-stoichiometric value, that is, more gases are supplied than are consumed for a given current density. Bad water management, loss of hydrophobicity in the

GDL due to degradation, or poor flow field design can all lead to problems of flooding and mass transport limitations.

3.4.1.2 Effects of Partial Pressure of H₂ and O₂

For ideal gases, the activity a used in Eq. 2.4 can be expressed as

$$a = \frac{P_a}{P^\circ}, \quad (3.29)$$

where P_a is the partial pressure of species a and P° is the standard pressure, i.e., 100 kPa. Thus, for a fuel cell that uses gaseous reactants, assuming the water product is steam, the Nernst equation (Eq. 2.12) can be rewritten as

$$E_{\text{Cell}} = E_{\text{Cell}}^\ominus + \frac{RT}{4F} \ln \frac{P_{\text{H}_2}^2 P_{\text{O}_2}}{P_{\text{H}_2\text{O}}^2}, \quad (3.30)$$

where P_{H_2} , P_{O_2} and $P_{\text{H}_2\text{O}}$ are the partial pressures of H₂, O₂ and H₂O, respectively. From this expression, individual contributions from the change in the partial pressures of H₂ and O₂ can be isolated. If the pressure of H₂ changes from $P_{\text{H}_2,1}$ to $P_{\text{H}_2,2}$ the cell voltage changes by

$$\Delta E_{\text{H}_2} = \frac{RT}{2F} \ln \frac{P_{\text{H}_2,2}}{P_{\text{H}_2,1}}, \quad (3.31)$$

and similarly, if the O₂ pressure changes from $P_{\text{O}_2,1}$ to $P_{\text{O}_2,2}$ the voltage shifts by

$$\Delta E_{\text{O}_2} = \frac{RT}{4F} \ln \frac{P_{\text{O}_2,2}}{P_{\text{O}_2,1}}. \quad (3.32)$$

Thus, if the partial pressure of H₂ or O₂ increases, the cell potential increase. In practice, this means that the cell potential is increased if the whole system is operated under pressure, as that leads to an increase in the partial pressure of the reactants, and that the cell voltage is higher if the system is run on pure oxygen (100% O₂) rather than with air ($\approx 21\%$ O₂). However, air is still often preferred, as using air is often more practical from a supply standpoint as ambient air can be used rather than needing a separate tank for onboard O₂ storage.

If the fuel cell is operated at elevated temperatures, for example 90–120 °C, the partial pressure of water needs to be increased if the RH is to remain the same, since the saturation pressure of water increases with temperature. However, if the total system pressure is kept the same, it follows that the partial pressure of hydrogen and oxygen decreases at elevated temperatures. According to Eq. 3.32, this leads to a decrease in cell potential. It has been reported that this decrease in partial pressure of oxygen leads to a lower OCV and reduced

performance of PEMFC when operated at intermediate temperatures (IT-PEMFC), i.e., around 100 °C to 120 °C, as compared to conventional operation temperatures of 80 °C or below [121, 214].

3.5 Fuel Cell Degradation

As mentioned in Chapter 1, one of the primary challenges facing PEMFC is the lifetime, related to harsh operating conditions. These conditions, which include potential cycling, start-up/shutdown cycles, freeze/thaw cycles, humidity cycling, contamination, and chemical poisoning, contribute to the degradation of various components of the fuel cell [215–219]. Table 3.4 lists some common degradation phenomena that are known to occur in PEMFC and gives examples of mitigation strategies.

Component	Degradation issue	Mitigation strategies
<i>Catalyst</i>	-Catalyst dissolution during voltage cycling -Chemical poisoning (e.g., CO)	-Limit cell voltage operation window, system hybridisation, develop new materials -Feed O ₂ in anode, use air filters and high purity fuel
<i>Catalyst support</i>	-Carbon corrosion at high potentials	-Well-controlled start-up/shutdown procedures with gas purging, develop new materials
<i>Membrane</i>	-Chemical attack by peroxide radicals -Mechanical stress due to RH cycling -Unstable at high temperatures	-Incorporate radical scavengers in membrane -Incorporate reinforcing backbone -Develop new materials
<i>Gas diffusion layer</i>	-Mechanical stress -Loss of hydrophobicity	-Use composite materials, reinforce, adjust thickness -Optimise, e.g., porosity and PTFE loading
<i>Bipolar plate</i>	-Corrosion due to acidic environment and high potentials	-Corrosion resistant coatings

Table 3.4: Degradation issues and mitigation strategies of different components in proton exchange membrane fuel cells [54, 126, 220–227].

The degradation of fuel cell performance can be divided into reversible and irreversible degradation phenomena. Reversible degradation often occurs on shorter timescales, ranging from minutes to hours, and associated performance losses can be partially or fully recovered. For example, flooding can cause a rapid drop in cell voltage, but can also be easily reversed by increasing the gas temperature to promote water evaporation or increasing the gas flow to flush out excess water [178], and while CO-catalyst poisoning severely limits the performance, it can be reversed by appropriate addition of, e.g., O₂ in the anode stream [221]. In contrast, irreversible losses often occur over longer timescales, ranging from weeks to months, and are more challenging or impossible to reverse. An example of irreversible loss is membrane thinning due to chemical degradation, leading to higher rates of hydrogen crossover or membrane failure [228].

To reach lifetime targets of 30 000 h or more with a performance loss less than 10% (a common target for end of life performance), the degradation rate cannot be more than a few μV per hour. Thus, every minor contribution to performance loss matters, and risk being the lifetime limiting factor. Although this section will primarily address the degradation of the MEA components, it is important to note that other components of the PEMFC system also suffer from degradation. For example, o-rings and gaskets can degrade due to chemical and thermo-mechanical stress, while bipolar plates can corrode in the highly acidic and humid environments of PEMFCs [196, 219, 229–231].

3.5.1 Catalyst Dissolution

In normal operation, a PEMFC operates below the OCV. When the fuel cell is under low or no load, the cathode potential will be close to the OCV, around 0.9–1.0 V_{RHE}. When the load increases, the cell voltage will decrease to provide a current density to match the demand, see Figure 3.9 [232]. Furthermore, maximum power density is typically achieved at a potential of around 0.5–0.6 V_{RHE}, and the 2-electron ORR pathway, which leads to unwanted H₂O₂ formation, becomes favourable at around 0.5 V_{RHE} or below. Hence, there is rarely a reason to drop further in potential [233, 234]. Thus, in normal operation, the cathode potential typically cycles between approximately 0.6 and 1.0 V_{RHE}, representing high and low load, respectively. As seen in the Pourbaix diagram for Pt (Figure 2.4b), Pt shifts from a metallic state to an oxidised state somewhere above 0.85 V_{RHE}. That means that during normal fuel cell operation, Pt will repeatedly cycle between being oxidised and being reduced. This shift of state can lead to Pt dissolution, especially during the reduction,



which can induce loss of catalyst material and decrease in electrochemical surface area (ECSA) on the cathode [235, 236]. Rapid shifts in potential are particularly harmful, as the surface does not have time to relax and redeposit Pt ions [215],

and the majority of the Pt dissolution tends to come from the cathodic scans, when PtO is reduced, compared to dissolution from the anodic scans [235–237]. Topalov et al. measured Pt dissolution rates during voltage cycling in 0.1 M HClO₄ using inductively coupled plasma mass spectrometry (ICP-MS), and found that dissolution started when cycling to an upper potential limit of 1.1 V or above, and that the amount of dissolution during the cathodic scan was highly dependent on the upper potential limit [235, 236]. The Pt dissolution on the anode is much less severe, as the anode experiences a lower and much more stable potential close to the equilibrium potential of HOR/HER.

Another factor contributing to Pt dissolution is that smaller Pt particles are desirable to maximise the mass activity. It has been found that the Pt particles with the highest mass activity have a diameter in the range 2 to 5 nm [149, 163, 238]. However, smaller particles also suffer more from dissolution than larger particles [149]. The dissolved Pt ions can then migrate into the membrane, where they are reduced to metallic Pt by hydrogen crossing over, thus crystallising and forming a Pt band inside the membrane [239–241]. In addition to material loss due to dissolution, Pt particles have been shown to degrade by other effects driven by potential cycling, such as growing by crystallite migration and coalescence, and Oswald ripening, and by particle detachment and redeposition [222, 242]. These different modes of Pt ageing are illustrated in Figure 3.11. The growth and dissolution of Pt particles results in a decrease of ECSA and increased kinetic overpotentials. The amount of Pt growth and ECSA loss is strongly linked to the potential limits during cycling. In particular, a higher upper potential limit has been found to lead to a greater loss of ECSA and Pt growth [243]. Thus, the issue with Pt dissolution can be mitigated by limiting the voltage operating window of the fuel cell and keeping the cell voltage as stable as possible, e.g., by hybridising the system with batteries to balance the power demand of the fuel cell.

Catalyst degradation, such as Pt dissolution during voltage cycling between $0.6 V_{\text{RHE}}$ and $1.0 V_{\text{RHE}}$, and its effect on fuel cell performance, was studied in **Paper I–III** and **Paper V**.

3.5.2 Start-Up/Shutdown and Cell Reversal

Although the fuel cell is typically operated at less than $1.0 V_{\text{RHE}}$, the potential can reach $1.5 V_{\text{RHE}}$ if the anode is starved of H₂ or if a H₂/air front is formed at the anode. This can happen during start-up/shutdown (SUSD) conditions if the fuel supply is not properly managed, or during operation if there is local H₂ starvation due to insufficient fuel supply [244–246]. These potential peaks are very harmful to the fuel cell, and in particular to the CL.

When a fuel cell is at rest and the exhaust is not closed, air can diffuse back into the anode through the exhaust. In addition, air can diffuse through the membrane from the cathode to the anode. As both the cathode and anode are filled with air, this causes the potential of both electrodes to reach the equilibrium potential of the ORR. As H₂ is introduced into the anode during start-up, a H₂/air front will form on the anode electrode moving from the

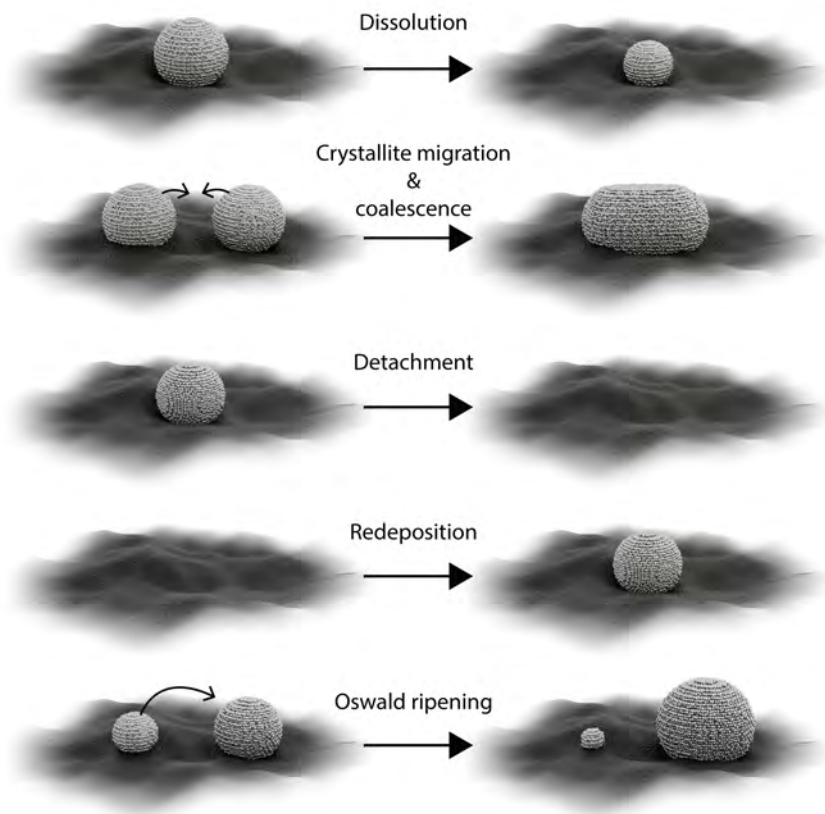


Figure 3.11: Possible degradation mechanisms for catalyst particles.

inlet to the outlet, creating two distinct regions, where region 1 filled with H_2 and region 2 filled with air. H_2 /air fronts can also form during uncontrolled shutdown, when air diffuses in from the exhaust. The resulting regions, along with the associated reactions, electron flow, and proton flow, are illustrated in Figure 3.12a.

In region 1, filled with H_2 , the anode and cathode will be at their usual equilibrium potentials (i.e., circa $0 V_{\text{RHE}}$ and $1 V_{\text{RHE}}$ respectively). However, in the air-rich region 2, the anode potential will be around $1 V_{\text{RHE}}$, leading to a potential difference across the anode. This potential difference will drive local ORR and HER, causing internal current within the anode, with electrons flowing from region 1 to region 2. Simultaneously, on the cathode side, the potential in region 2 increases to maintain a constant potential difference of circa 1 V across the membrane. Thus, the cathode potential can locally reach much higher than $1 V_{\text{RHE}}$, to over $1.4 V_{\text{RHE}}$. Consequently, water splitting (OER) and carbon oxidation (COR) can occur on region 2 at the cathode. The internal potential difference within the cathode drives the electrons to flow from the COR and the OER in region 2 to the ORR in region 1. The protons needed to complete the reactions in region 1 and region 2 will travel the path of least resistance through the membrane from the anode to the cathode in region 1 and from the cathode to the anode in region 2. Despite these internal currents, the cell does not generate any external current, resulting in a net flow of zero for both electrons and protons.

Similar issues can occur due to fuel starvation when the cell is under load, see Figure 3.12b. The anode can be locally starved of H_2 due to, e.g., water blocking the pores physically hindering gas transport or rapid load changes without proper fuel supply management leading to fuel depletion near the exhaust. Even without proper fuel supply, the cell must output the same amount of current as the surrounding cells. To sustain the current demand, electrons on the anode are instead provided by water electrolysis and carbon corrosion occurs, see Figure 3.12b. To drive these electrochemical reactions, the potential of the anode changes locally to well above $1.0 V_{\text{RHE}}$, while the cathode remains under its usual conditions. This leads to a reversal of cell voltage, and the cell acts as an electrolytic cell that uses energy provided by the surrounding cells to drive the reactions, thus reducing the overall energy output of the fuel cell stack.

Both uncontrolled start-up/shutdown conditions and local fuel starvation result in COR, and hence corrosion of the carbon support. Carbon corrode into carbon dioxide in the COR,



While the COR has a thermodynamical equilibrium potential of $0.207 V_{\text{RHE}}$ at 25°C [247], very high overpotentials are needed for COR to transpire at any considerable rate, due to the sluggish kinetics of the COR. Thus, during

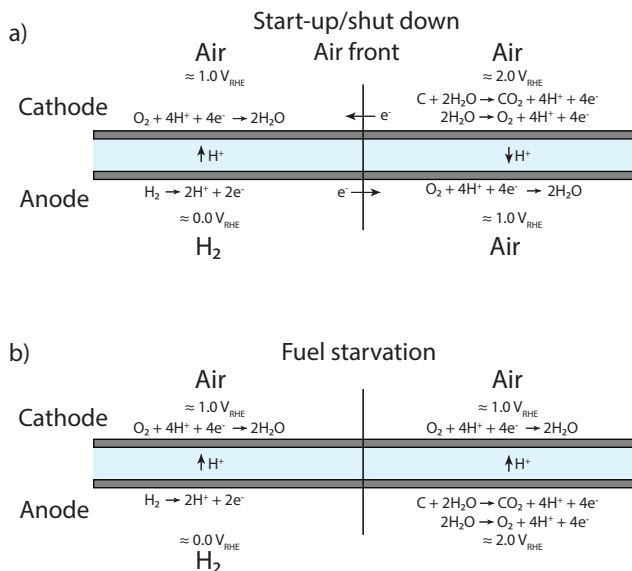


Figure 3.12: Effects of a) forming an H₂/air front inside the fuel cell during start-up/shutdown events and b) local fuel starvation.

normal operation, the effect of COR is negligible. It is mostly during these special unwanted events the potential increases above $1.0 V_{RHE}$ and the effects of COR start to be noticeable. Furthermore, there are indications that Pt is catalysing the COR, thus exacerbating the issue of support degradation in Pt/C catalyst [148, 245, 248].

Loss of support due to carbon corrosion means Pt particles can detach [245], and possibly attach somewhere without electrical or ion conductivity, essentially leaving the Pt lost and leading to a decrease of ECSA and increased kinetic overpotentials. Furthermore, carbon corrosion can lead to loss of hydrophobicity in the CL and GDL, and can cause a collapse of the carbon support leading to compaction of the porous structure of the CL [245]. Both of these effects can limit the mass transport of reactants to the catalytic sites and increase the concentration overpotentials. Collapse and deformation of the carbon support can also lead to an increase in the internal resistance of the cell as a result of loss of physical contact between Pt, the ionomer, the support, and GDL leading to increased ohmic overpotentials. All of this leads to massive losses of activity during carbon corroding conditions [245, 249].

Carbon corrosion issues during start-up/shutdown events can be mitigated by appropriate purging of the system during shutdown with inert gases, using dummy loads to consume excess H₂ and O₂ after shutdown, or designing catalyst supports that can withstand corrosion [245]. Several versions of gas purging and dummy load uses have been proposed and successfully implemented, aimed at preventing the formation of a H₂/air interface [245]. However, these protocols are suboptimal for the implementation of actual vehicular applications, as it is

inconvenient to bring purging gases, such as N_2 along with the vehicle [245]. Carbon corrosion from fuel starvation can be avoided or limited by adequate fuel supply and well-designed GDLs and flow fields that facilitate water removal and promote adequate gas supply.

The effects of high-voltage cycling and carbon corrosion were studied in **Papers III—IV**.

3.5.3 Temperature Cycling

Fuel cells can experience varying temperatures within a broad temperature range. Firstly, fuel cells should be able to cold start from at least -20°C [250, 251], which can be an issue due to water management. Water is both produced in the MEA during fuel cell operation and provided externally in the humidified gases. If this water is left in the system after the system is shut down at subzero temperatures, the water will freeze and expand. This causes mechanical damage to GDLs, CL and membrane, and repeated freeze/thaw cycles greatly deteriorate the performance of fuel cells [250]. Strategies to avoid ice formation involve purging the cell after use to remove all liquid water, and operating the cell at low voltages, i.e. at high power, at start-up to quickly produce much heat to raise the stack temperature above 0°C [252].

Furthermore, during extreme loads, the temperature is at risk of increasing to 100°C or above if the cooling system is not properly dimensioned to handle such events. These higher temperature ranges can, as discussed in Section 3.2.1, degrade the Nafion membrane. However, so far little research has been published on effects of PEMFC operation or degradation at 80 – 120°C , also known as intermediate temperatures (IT). Butori et al. [214] studied the effects on the performance of a single cell fuel cell operated at 80°C , 100°C , and 120°C , and found that higher temperatures does not inherently lead to worse performance. However, the current density can be limited because of the difficulty of keeping both the relative humidity levels and the partial oxygen pressure high at the same time. Zhang et al., [121] and Song et al., [253] also reported decrease of performance and OCV at intermediate temperatures, likely due to high partial pressures of water vapour. Furthermore, Butori et al. also studied the effects of IT-PEMFC operation on membrane conductivity and hydrogen crossover rates, and saw that membrane conductivity improved and that membrane permeability increased with increasing RH and temperature [254]. However, they did not study the long-term effects of degradation. IT operation could also potentially lead to increased rates of degradation of the Pt catalyst, or the carbon support.

The effects of IT-PEMFC operation was studied in **Paper V**.

3.5.4 Humidity Cycling

The membranes are sensitive to humidity levels. Low RH dehydrates the membrane, which reduces its ion conductivity and causes it to shrink. The movement of swelling and shrinkage of the membrane can cause mechanical

damage to the structures, e.g., in the form of cracks or tears in the membrane [55]. Damage to the membrane can lead to fuel leakage and crossover, harming fuel cell performance and further accelerating MEA degradation [55]. Cycling of the RH leads to faster degradation compared to constant RH conditions [251, 255]. Furthermore, high RH has been associated with an increase in Pt degradation and a decrease in carbon support degradation and membrane degradation [195, 243].

3.5.5 Pinholes

For maximum energy efficiency, the anode and cathode should be completely separated by the membrane, with only protons being transferred via the membrane, although in reality, some hydrogen crossover occurs naturally in a small amount even in pristine membranes. However, pinholes can be generated in the membrane due to physical defects, mechanical stress, and chemical degradation, causing hydrogen crossover rates to increase massively [256, 257]. This reduces the OCV, reduces efficiency and further increases the degradation rates or leads to membrane failure.

3.5.6 Chemical Damage and Poisoning

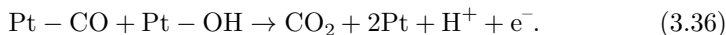
The components of the fuel cell can suffer from chemical damage, poisoning, and contamination. Impurities and contaminants can come from within the fuel cell system itself. The highly acidic conditions of the PEMFC, coupled with high potentials and a high humidity environment, promote the corrosion of, e.g., steel bipolar plates, creating metal ions. These ions may poison the membrane or catalyst. The protons inside the membrane that facilitate proton conduction can be exchanged for metal cations, thus reducing the proton conductivity. Furthermore, Fe^+ ions from steel bipolar plates can catalyse the conversion of H_2O_2 to hydroxyl and peroxy radicals that increase the rate of membrane degradation [202]. The effects of free radicals can be reduced by introducing free radical scavengers, such as ceria, into the membrane [54]. Steel bipolar plates are often coated with corrosion resistant materials to reduce the corrosion of the bipolar plates [57, 258].

Moreover, contaminants can also come from outside sources, e.g., via the fuel or air supply. For example, if H_2 is produced by steam reforming, CO can be present in the fuel at concentrations up to 100 ppm [221]. This is a considerable issue as CO binds strongly to the Pt surface at low potentials,



When CO binds to Pt, it effectively blocks catalytic sites and reduce the available ECSA, thus poisoning the surface and reducing the activity of the catalytic layer. CO poisoning can lead to considerable performance loss at CO concentrations of only a few ppm [126]. CO poisoning is mostly an issue on the anode, since that is where the potentially contaminated H_2 is supplied, and

any CO present on the cathode would immediately be oxidised to CO₂ due to the oxidative environment of high potentials and presence of O₂,



Fortunately, it has been found that injecting 2–5% O₂ into the anode feed completely reverses the effects of CO poisoning [221], and the use of a Pt alloy as an anode catalyst, such as PtRu, has also been shown to increase CO tolerance [259]. The inclusion of Ru has two effects. Firstly, Ru decreases the binding energy of CO to Pt, and secondly, Ru can bind OH stronger than Pt, which can then react with CO to form CO₂ [259]. Furthermore, CO adsorption on Pt is strongly dependent on temperature. An increase of working temperature reduces the effects of CO poisoning, and at 125 °C, CO concentrations up to 0.1% can be tolerated [260]. Other contaminants can also be introduced to the cathode electrode from the outside environment if using, e.g., ambient air. Air filters can be used to minimise the amount of contaminants that reach the cathode.

3.5.7 Mitigation Strategies

Although some degradation of components is inevitable, the effects can be minimised. Two main strategies can be used to mitigate the degradation issues of PEMFCs and improve their lifetime. Either more durable materials can be developed to withstand harsh operation conditions, or fuel cell operation can be carefully controlled to prevent the most damaging operation conditions. To implement either strategy, studies need to be done on the effects of different conditions on the fuel cell components, so that degradation mechanisms can be better understood and avoided.

Chapter 4

Experimental Techniques

In this chapter, I will provide a brief introduction to the theory and principles behind the techniques used in the work that form the basis of **Paper I–V**. For more information on experimental details, the reader is referred to the appended papers.

4.1 Electrochemical Measurements

Due to the nature of fuel cells, electrochemical methods and characterisation techniques are of great importance for fuel cell research. In this section, I will give an introduction to some fundamental characterisation techniques in electrochemistry and some of the most important techniques utilised in **Paper I–V**.

4.1.1 Set-Ups

Two main types of electrochemical setups have been used in the work included in this thesis: the electrochemical half-cell and the single-cell test station. The half-cell is a good tool for measuring the intrinsic behaviour of catalysts by isolating individual processes. The controlled environment allows for detailed analysis of catalyst performance. However, conditions in half-cells often differ significantly from those in real fuel cells, making it challenging to directly extrapolate half-cell results to real-world applications. In contrast, the single-cell setup closely mimics the conditions of real fuel cells, providing insight into how catalyst materials perform in realistic environments. However, while this setup offers a more practical evaluation, it also involves many interconnected components, making it difficult to isolate the effects of individual materials.

4.1.1.1 Liquid Half-Cells

In an electrochemical half-cell, each half-reaction of the electrochemical reaction can be studied separately. The simplest version of an electrochemical cell

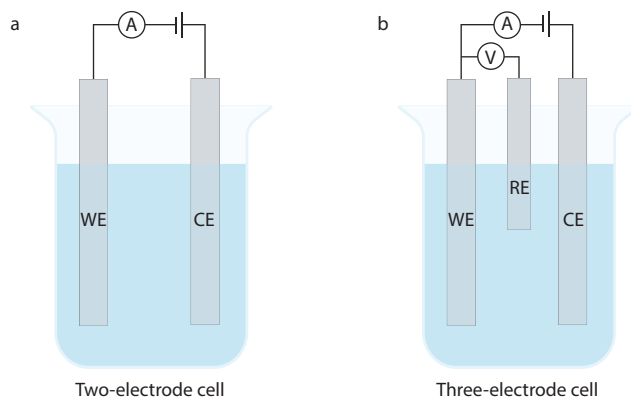


Figure 4.1: Schematic of a) a two-electrode and b) a three-electrode cell.

contains two electrodes—one working electrode (WE) on which the half reaction of interest is occurring, and one counter electrode (CE) that acts to balance the charge by acting as an anode or cathode to the reaction on the WE—connected via an electrolyte. A voltage is applied between the electrodes and the resulting current is measured, or vice versa. When currents pass through the CE, its potential will shift, making it difficult to measure the absolute potential of the WE accurately. To overcome this, a third electrode, known as the reference electrode (RE), is often added to the system, making it a three-electrode set-up. No current passes through the RE, so its potential is kept stable at a known value. The potential of the WE is measured against the RE, while the current is measured between the WE and the CE, see Figure 4.1. The potential of the RE depends on the reversible reactions on which it is based. To simplify the comparison between measurements performed against different REs, the voltage is often converted and presented against the redox potential of hydrogen H_2/H^+ , also known as RHE, which is defined as 0 V_{RHE} . During electrochemical measurements, a potentiostat is often used to control and measure the potential and current. The potentiostat precisely controls the potential of the WE relative to the RE and measures the resulting current flowing through the system.

4.1.1.2 Electrochemical Quartz Crystal Microbalance

The quartz crystal microbalance (QCM) technique is a characterisation method in which small mass changes can be measured by tracking variations in the resonance frequency of a quartz crystal. A good QCM setup can detect changes less than 1 ng cm^{-2} . In comparison, a monolayer of Pt weighs around 400 ng cm^{-2} [261]. Quartz is a piezoelectric material, which means that there is a relationship between applied voltage and mechanical deformation. Coating both side of a quartz crystal disc with electrodes (Figure 4.2a), and applying an alternating electric field between them, will induce oscillations (Figure 4.2b). At a specific resonance frequency, the amplitude of the oscillations will

increase. This resonance frequency will depend on the mass of the crystal and the material on or near the surface. If mass is added or lost, the frequency will shift.

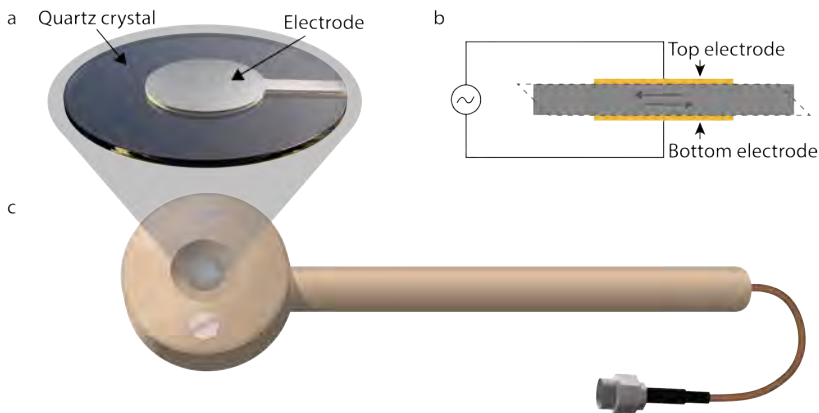


Figure 4.2: a) Typical quartz crystal used for quartz crystal microbalance (QCM) measurements. b) An alternating electrical field is applied over a quartz crystal, which causes it to oscillate. c) Illustration of an electrochemical QCM dip-holder used for measurements in **Paper I**. A QCM crystal is coated with one electrode on either side, and the crystal is mounted in the dip-holder such that the electrode of interest is exposed to the outside, and can be used as a working electrode in an electrochemical cell. The dip-holder is made from polyetheretherketone (PEEK), and held together using screws made from nylon. The holder is sealed using o-rings made from perfluorinated elastomer (FFPM).

The Sauerbrey equation relates the frequency change Δf_n of the resonance frequency of the n^{th} overtone to the mass change Δm as

$$\Delta f_n = -n \frac{2f_{0,n}^2}{A\sqrt{\rho_q\mu_q}} \Delta m, \quad (4.1)$$

where $f_{0,n}$ is the initial resonant frequency of the n^{th} overtone, A is the area of the electrode, ρ_q is the density of quartz and μ_q is the shear elastic modulus of quartz [262]. The Sauerbrey equation is valid only if certain conditions are satisfied: the electrode films must be rigid and thin, and the change in mass should be small in comparison to the initial mass of the quartz crystal [263, 264]. Preferably, the resultant frequency change Δf_n should be less than 2% of the initial resonance frequency $f_{0,n}$. If the mass changes are larger than this, a more complex expression than Eq. 4.1 needs to be used, that take into account the difference in density and wave propagation velocity of the quartz and the deposited material. The rigidity criterion of the film can be checked by looking at the change in the dissipation factor,

$$\Delta D = \frac{2\Delta\Gamma}{f_{0,1}}, \quad (4.2)$$

where $\Delta\Gamma$ is the change in half bandwidth and $f_{0,1}$ is the initial fundamental frequency. The film is considered rigid if

$$\frac{\Delta D}{\Delta f} \ll \frac{1}{f_{0,1}}. \quad (4.3)$$

In electrochemical QCM (EQCM), one electrode of the QCM is used as the WE in an electrochemical half-cell, allowing for measuring mass changes and performing electrochemical measurements simultaneously. EQCM can be used to measure, e.g., mass changes associated with oxide formation during potential cycling and dissolution rates.

EQCM set-ups come in many variants, such as flow cells or dip holders. Figure 4.2c illustrates a dip-holder that was used for EQCM measurements in **Paper II**. A quartz crystal coated with a Pt and an Au electrode is mounted in the dipholder, so that the Pt electrode is exposed to the outside, where it is in contact with the electrolyte. This allows for using the Pt electrode as a working electrode in an electrochemical cell, while applying an alternating current field between the Pt and Au electrode to measure the shift in frequency response.

4.1.1.3 Fuel Cell Test Station

While fuel cells intended for commercial applications are often large and made of stacks, small-scale single-cell setups can be used for research purposes to study catalyst behaviour under realistic fuel cell conditions while minimising material consumption. Figure 4.3 shows the schematic of the setup used for measurements in **Paper I** and **Paper III–V**. The flow rates of the gases and their composition (H_2/Ar for the anode and $\text{O}_2/\text{Air}/\text{Ar}$ for the cathode) are controlled using mass flow controllers. Before entering the fuel cell, the gases pass through humidifiers to increase their RH. The humidifiers work by bubbling the gases through water, and the RH levels are controlled by controlling the temperature, and hence the water saturation pressure, of the humidifiers. The RH levels of the gases are measured using humidity sensors at the inlet and outlet of the fuel cell. The temperature of the ingoing and outgoing gases is measured using thermocouples. The pressure of the gases are regulated using back pressure regulators placed at the outlets and monitored by pressure gauges at the fuel cell inlet. The humidifiers, gas tubes, and fuel cell are all individually heated using heating tapes connected to thermocouples. A potentiostat is used to control and measure the potential and current between the anode and the cathode of the MEA in the fuel cell. The test station is controlled and automated via a LabVIEW script.

During fuel cell measurements, the fuel cell operates as a two-electrode system, where the cathode acts as the working electrode, and the anode works both as the counter electrode and as a reference electrode. If the anode is in a H_2 rich environment and the currents are relatively small so that the anode overpotential is small, the anode will act similarly to a reversible hydrogen electrode due to the fast kinetics of the HOR on Pt [205]. Thus, the cathode potential will essentially be the same as the cell voltage (see Figure 3.10), and the whole system will behave similarly to a three-electrode set-up. This is the case for the cell used in **Paper I** and **Paper III—V**, since the cell is working under high flows of pure H_2 and the cell is relatively small, thus the H_2 pressure difference between inlet and outlet of the electrode area will be negligible. Thus, the anode can be used as a reference electrode and eliminates the need to add an additional electrode to the set-up, which would greatly complicate the set-up. The fuel cell used in this set-up is a 5 cm^2 single-cell using graphite flow fields with a serpentine flow field pattern. Graphite flow fields are commonly used in research because of their superior resistance to corrosion, assuming it is not the bipolar plate material that is under investigation. Although graphite flow fields are thicker than stainless steel flow fields, this is generally not a concern in single-cell measurements for research and development purposes, where weight or size optimisation is often less critical. The MEAs used in the fuel cell are assembled according to Figure 3.6a and inserted into the fuel cell according to Figure 3.6b. The compression rate of the GDLs is controlled by the use of appropriately thick glass fibre reinforced Teflon gaskets, and the cell is closed using a torque force of 12 N m in **Paper I** and **Paper III**, or by using a 1.5 bar pneumatic pressure in **Paper IV** and **Paper V**.

4.1.1.4 A Note on the Difference Between Fuel Cell and Half-Cell Measurements

Often, performance and degradation of catalyst materials for PEMFCs are studied in three-electrode half-cells. However, due to the considerable difference in conditions between half-cells and PEMFC, results obtained in either set-up type may differ substantially, and it can be difficult to extrapolate the results obtained in half-cells to PEMFC [265, 266]. Half-cell measurements, such as rotating disc electrode (RDE) measurements, are used to monitor one half of the redox reaction at a time, either the oxidation or the reduction, at the electrode surface. To do so, the catalyst material in question is deposited on the electrode, which is dipped into a liquid electrolyte, often $0.5\text{ M H}_2\text{SO}_4$ or 0.1 M HClO_4 . Because of the liquid environment, the mass transport of oxygen is poor, and thus RDE measurements are limited to low current densities. Typically, in RDE measurements, the ORR performance of a catalyst is evaluated at potentials around $0.9\text{ V}_{\text{RHE}}$, far from the high current densities at $0.6\text{ V}_{\text{RHE}}$ relevant for practical fuel cell operation. Furthermore, half-cell measurements are most often performed at room temperature and at ambient pressure. Thus, half-cell systems are inherently different from PEMFCs, which operate at elevated temperatures, using gaseous reactants and solid electrolytes, and at elevated pressures. Table 4.1 highlights some key differences in the operation

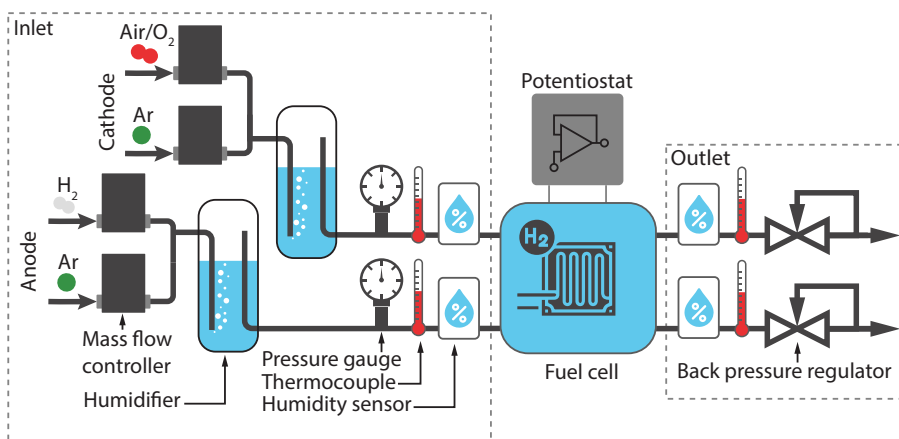


Figure 4.3: Schematic of the single-cell test station used in this thesis work. At the inlet, mass flow controllers control the mass flow and stoichiometry of ingoing gases (H_2 and Ar for the anode and Ar, synthetic air and pure O_2 for the cathode). The gases are passed through humidifiers before entering the fuel cell. Thermocouples and humidity sensors are connected to both the inlet and outlet of the fuel cell to measure temperature and RH levels of the ingoing and outgoing gases. Back-pressure controllers are connected to the outlets, and the pressures are measured using pressure gauges connected to the inlets. The fuel cell is controlled by a potentiostat, and the test station is controlled via a LabVIEW program. The humidifiers, tubing and fuel cell are all insulated and heated, which is not depicted in the figure.

conditions between PEMFCs and half-cells. According to Lazaridis et al. [266], durability trends measured in RDE setups are not transferable to PEMFCs due to differences in Pt dissolution/redeposition rates and non-CL degradation that cannot be reproduced in the simplified electrode used in RDEs. Imhof et al. [267] tried to recreate MEA degradation in RDE experiments by increasing the temperature in the RDE to 80 °C, and by changing the ionomer/carbon ratio to a closer match to that of the MEA, yielding a more similar degradation of the electrochemical performance. Yu et al. [268] also noted the discrepancies between the results obtained from the half-cell measurements and the MEA measurements using the same testing protocol in both set-ups. They tried to alleviate this issue by changing the testing conditions in the half-cell until the results match those obtained in an MEA, e.g., by changing the potential limits and electrolyte used in the half-cell measurements. However, it is not clear how such changes in the operating conditions should be applied when looking at other catalyst materials or when studying other types of degradation phenomena.

An example of the discrepancy between half-cell measurements and PEMFC measurements involves Pt-rare-earth-metal alloys. These alloys show great enhancement in activity in half-cell testing, and due to the large negative heat of formation between platinum and rare earth metals they have been hypothesised to have good stability in PEMFCs [47–50]. However, they have been shown to suffer degradation and dealloying when introduced to PEMFC environments. For example, PtY alloys have shown good activity under RDE conditions, but in PEMFC measurements they show little improvement in activity or stability compared to the Pt catalyst [269].

Parameter	PEMFCs	Half-Cells
<i>Electrolyte</i>	Solid polymer	Liquid
<i>Reactants</i>	Gaseous	Dissolved in liquid
<i>Temperature</i>	20 °C–120 °C	Room temperature
<i>Overpressure</i>	Up to 2 barg	0 barg
<i>Mass-transport regime</i>	Gas phase diffusion	Liquid diffusion
<i>Mass-transport limited current</i>	>4 A cm ⁻²	<10 mA cm ⁻²

Table 4.1: Typical operating conditions for PEMFCs and liquid half-cells.

Thus, while half-cells and similar techniques might be a good tool to quickly and cheaply screen the viability of new material candidates, much care should be taken when extrapolating those results to real PEMFC performance. If possible, experiments should be performed in an environment as close as possible to that of the intended end use.

4.1.2 Electrochemical Methods

Electrochemical reactions have several important characteristics, such as the relationship between voltage and current, which can be probed using various electrochemical methods, some of which will be described here.

4.1.2.1 Cyclic Voltammetry

In cyclic voltammetry (CV), the potential between the RE and the WE is cycled linearly between two potential values, and usually the current is then plotted against the potential of the WE. The resulting plot is known as a cycling voltammogram, which is also shortened as CV. CVs can be used to study the electrochemical properties of an analyte in the electrolyte solution or of the electrode surface itself. Positive currents come from oxidation on the WE, and negative currents come from the reduction on the WE. In each scanning direction, characteristic peaks will appear from oxidation/reduction of species. These features will depend on the electrode, analyte, and electrolyte, and can be used as a fingerprint of sorts to identify materials if the material in question has any electrochemical reaction taking place in the potential window used. CVs can also be used to identify whether reactions are reversible, if reactions are limited by kinetics or mass transfer, and if the surface is changing over time due to, e.g., the formation of a monolayer.

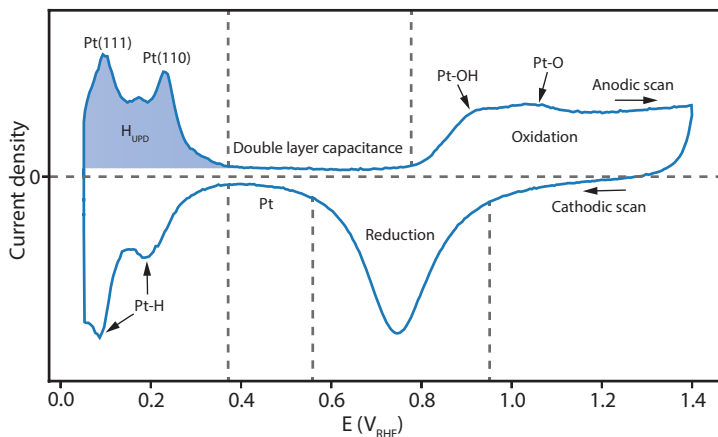


Figure 4.4: Typical cyclic voltammogram of polycrystalline Pt in 0.5 M H_2SO_4 in an inert atmosphere.

Of special interest to PEMFC research is the typical CV of polycrystalline Pt in acidic conditions, see Figure 4.4, which has three main regions in which different electrochemical processes dominate. Below 0.4 V_{RHE} is the region associated with hydrogen underpotential deposition (H_{UPD}) and desorption. During cathodic scans, i.e., negative scans, H^+ ions begin to bind to the Pt atoms on the surface, starting from around 0.4 V_{RHE} , leading to distinct current peaks. At 0 V_{RHE} , hydrogen evolution begins, and cycling further down in potential would lead to large negative currents from hydrogen evolution. Increasing the potential from 0 V_{RHE} , during anodic scans, will cause the H^+ adsorbed to the surface to instead desorb. Different crystal facets of Pt have different adsorption/desorption energies and thus the peaks appear at different potentials. Thus, each peak in the adsorption/desorption current is associated with a specific Pt crystal plane and can be used to identify the

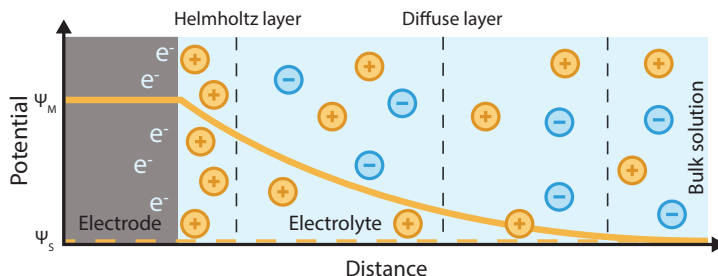


Figure 4.5: Illustration of the electric double layer formed at the interface between an electrode and an electrolyte, and the resulting potential distribution in the electrolyte.

crystal structures present on the surface of the sample. The CV in Figure 4.4 show signs of H_{UPD} peaks from the Pt crystal planes Pt{111} and Pt{110} [270, 271], typical of polycrystalline Pt surfaces.

The flat region between 0.4 and 0.7 V_{RHE} stems from the double layer capacitance. When the electrode potential changes, a surplus or deficit of electrons will accumulate near the surface in the electrode, even if no other electrochemical reactions are taking place. In turn, this will attract ions in the electrolyte, creating an electrical double layer, which acts as a capacitor (see Figure 4.5). The total charge stored in the electric double layer will depend on the applied potential and the electrode surface area. The current from charging the double layer is proportional to the scan speed, and the capacitance C of the double layer is defined as

$$C = \frac{\partial Q}{\partial E}, \quad (4.4)$$

where ∂Q is the change in charge and ∂E is the change in potential. Thus, if the potential is held at a specific point, the electric double layer will be stable, and no current from charging the layer will arise. The double layer is charged throughout the whole CV, hence its contribution has to be accounted for when studying other effects in the CV. The double layer is proportional to the total chargeable area, which in the case of a Pt/C electrode is the sum of the electrochemically available Pt surface and the carbon surface.

Continuing the anodic scan, at around 0.9 V_{RHE} , OH binds to the surface, and at 1.0 V_{RHE} , Pt-O starts to form. The surface oxide layer continues to grow at higher potentials, and somewhere after 1.23 V_{RHE} , oxygen evolution will become the dominant process. During cathodic scans, the Pt-O that has been formed is reduced to metallic Pt at about 0.8 V_{RHE} .

4.1.2.2 Electrochemical Surface Area

The ECSA of the Pt can be determined from the blue marked region in the CV in Figure 4.4, or equivalent region from the cathodic scan. Consider the region between 0.0 and 0.4 V_{RHE} . The currents in this region comes from

H_{UPD} adsorption/desorption to the Pt surface during cathodic/anodic scans, respectively. Every H^+ takes/gives an electron when it is adsorbed/desorbed. Assuming that every Pt atom on the surface has adsorbed one H^+ ion, the total charge associated with hydrogen adsorption Q can be determined by integration the current I versus time t in this region,

$$Q = \int I dt = \int I dE \frac{dt}{dE}, \quad (4.5)$$

where E is the potential and dE/dt is the scan speed. Note that the current from these types of reactions are proportional to the scan speed, and that the total charge associated with the process is the same even if the scan speed is varied. When using Eq. 4.5, the charge associated with the double layer capacitance should be subtracted. Dividing Q with the charge of one adsorbed monolayer σ , gives the electrochemical surface area

$$A_{\text{ECSA}} = \frac{Q}{\sigma}. \quad (4.6)$$

The surface charge of a monolayer σ depends on the type of metal or metal alloy and the dominant crystal facets. For polycrystalline Pt, the surface charge of one monolayer of hydrogen is usually set to $\sigma_{\text{Pt}} = 210 \mu\text{C cm}_{\text{Pt}}^{-2}$, which is an average of the surface charge of the most common crystal facets [272, 273]. For H_{UPD} on Pt, it is sometimes assumed that integrating from the double layer region to the lower peak in the cathodic scan (see Figure 4.4) corresponds to a 77% hydrogen coverage [272], which gives the formula for the ECSA as

$$A_{\text{ECSA}} = \frac{\int I dE}{0.77 \sigma \frac{dE}{dt}}. \quad (4.7)$$

For fuel cell research, the surface area of Pt A is often presented as ECSA per mass Pt, as the mass utilisation of the metal is of interest. This is calculated by

$$A_{\text{ECSA}/\text{mass}} = \frac{Q}{\sigma L A_{\text{geo}}}, \quad (4.8)$$

where L is the Pt loading of the sample and A_{geo} is the geometric surface area of the electrode.

Other reactions with distinguishable peaks in the CV can also be used to determine the ECSA in a similar fashion, such as the reduction of a metal on the surface or CO-stripping, or by measuring the capacitance of the double layer [274]. During CO-stripping, the usually undesirable affinity of CO to

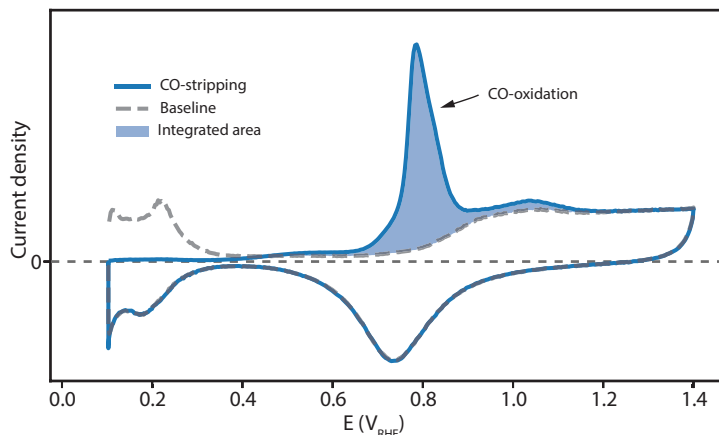


Figure 4.6: Typical behaviour of CO-stripping of polycrystalline Pt in 0.5 M H_2SO_4 in an inert atmosphere. First scan (solid blue line) causes all absorbed CO on the Pt surface to oxidise, and the second scan (dashed grey line) is used as a baseline when integrating. Note that the peaks associated with hydrogen desorption are suppressed during the first scan as CO binds strongly to the surface, blocking all sites from hydrogen adsorption.

bind strongly to many surfaces, otherwise known as CO-poisoning, is used to an advantage. The catalyst surface is flushed with CO for a few minutes while the catalyst surface is held at a low potential, typically around $0.2 V_{\text{RHE}}$. CO will then bind to all available surface sites. While continuing to hold the electrode potential steady, the surface is flushed with an inert gas such as Ar, until all CO except for the CO bound to the catalyst surface is removed. While still under an inert environment, the electrode potential is scanned up to at least $1.0 V_{\text{RHE}}$. At around $0.8 V_{\text{RHE}}$, CO undergoes oxidation to form CO_2 , resulting in a large current peak, see Figure 4.6. Another CV is performed immediately after to be used as a baseline. The current from the CO oxidation peak is integrated according to Eq. 4.5, and the ECSA is calculated according to Eq. 4.6, using a surface charge $\sigma_{\text{Pt,CO}} = 420 \mu\text{C cm}_{\text{Pt}}^{-2}$, i.e., twice that of a monolayer of hydrogen as two electrons are transferred per CO being oxidised.

4.1.2.3 H_2 Crossover

Linear sweep voltammetry (LSV) is a technique similar to CV, with the difference being that the voltage is only swept in one direction, between two voltages at a set scan speed. LSVs can be used to measure H_2 -crossover through the membrane in a fuel cell, which is a process that leads to fuel inefficiencies and lower cell performance and thus is of importance to monitor. To measure H_2 -crossover, the potential is swept through the double layer region, typically from $0.3 V_{\text{RHE}}$ to $0.7 V_{\text{RHE}}$, where the contribution from H_{UPD} or Pt oxidation is negligible, at a slow speed, typically around 1–2 mV/s, to avoid contributions

from charging the double layer [275]. During these measurements, the anode is supplied with H₂ gas, while the cathode is supplied with an inert gas such as N₂ or Ar. Since the cathode gas is inert and the double layer does not contribute significantly at such slow scan speeds, the current can be assumed to come from electrochemical oxidation of H₂ gas crossing over from the anode through the membrane. The oxidation of any crossover H₂ can be assumed to be immediate due to the high overpotential compared to the hydrogen reduction equilibrium potential (0 V_{RHE}). The crossover current i_0 resulting from H₂ crossover can be evaluated by making a linear fit to the data,

$$i(V) = i_0 + \frac{V}{r_{\text{int}}}, \quad (4.9)$$

where i_0 is the crossover current, and r_{int} is the internal cell resistance. The current i_0 can then be converted to H₂ flux, by dividing it with Faraday's constant F and remembering that each H₂ produces two e⁻,

$$J_{\text{H}_2} = \frac{i_0}{2F}. \quad (4.10)$$

The hydrogen crossover can also be measured by another similar method, chronoamperometry (CA), where the potential is held for a few minutes at a few potentials in the same range, between, e.g., 0.3 V_{RHE} and 0.7 V_{RHE}. The current for each potential is measured as an average at the end of each potential hold. The hydrogen crossover is then calculated in the same way as before, using Eq. 4.9 and Eq. 4.10.

4.1.2.4 Polarisation Curves

The performance of an electrocatalyst can be evaluated using polarisation curves. Polarisation refers to the overpotential, or deviation from the equilibrium potential, of the reaction in question. Polarisation curves are typically plotted as E vs. j or $\log j$, even when E is the independent variable that is being controlled during the experiment, and shows what overpotentials are needed to reach a certain current density. Polarisation curves can be used to probe reaction kinetics, determine the Tafel slope and exchange current density, and study mass transport limitations. Polarisation curves can be obtained by performing an LSV between two potentials within the operating window of the fuel cell/catalyst, e.g., 0.5 V_{RHE} and OCV, in the presence of reactants for the relevant reaction to be studied, i.e., H₂ and O₂/air. Figure 4.7 shows a typical polarisation curve measured in a single-cell PEMFC fed with H₂ and synthetic air. If using a scanning technique, polarisation curves should be performed at low scan speed to avoid currents from charging the double layer. Polarisation curves can also be measured by chronoamperometry (CA) or the similar method chronopotentiometry (CP). In CA, the potential is instead held for a few minutes at a few potentials in the range of interest. In CP, the current, rather than the potential, is held constant for a period of time at a few current

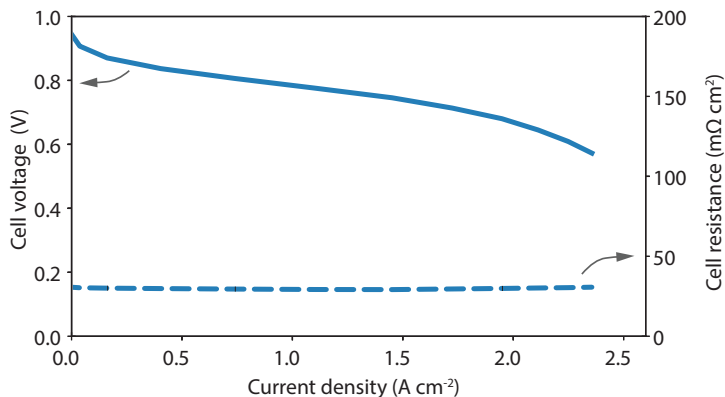


Figure 4.7: Typical polarisation curve (solid line) and high frequency resistance (dashed line) measured in a single-cell PEMFC. Measurements were performed while feeding H_2 and air to the anode and cathode, respectively, and under 1.5 barg overpressure.

densities in the operating window. By their static nature, CA and CP types of measurements naturally exclude effects from charging of the double layer, and are therefore often preferred for accurate measurements of, e.g., kinetic parameters.

4.1.2.5 Electrochemical Impedance Spectroscopy

Electrochemical impedance spectroscopy (EIS) is a method in which impedance Z is typically measured by applying an alternating potential E to a system and measuring the current response I , where

$$Z = \frac{E}{I}. \quad (4.11)$$

The impedance Z is often expressed as an imaginary number, where $\Re Z$ corresponds to the normal resistance, i.e., the direct response of the current to the applied voltage, and $\Im Z$ is a phase-shifted response of the current, due to capacitive and inductive properties. In EIS, the frequency f of the ac-signal is scanned from high to low frequency, or vice versa, and the resulting impedance $Z(f)$ is plotted either in the imaginary plane in a Nyquist plot, or $\Re Z$ and $\Im Z$ are plotted separately in a Bode plot.

The EIS spectra can be fitted to an equivalent circuit [81]. A simple equivalent circuit includes a resistance connected in series with a capacitor in parallel with a resistance. A so-called Warburg element can be added to account for diffusion processes.

Different frequency regimes give information on different processes in the cell. Thus, EIS can be used to distinguish between contributions from different

components and processes in the cell. The high frequency resistance (HFR) comes from H^+ -resistance in the membrane, electronic resistance in the CL and GDL and contact resistance, whereas lower frequencies can give information about, e.g., charge transfer resistance, mass transport limitations and CL flooding [276–279]. Figure 4.7 shows the typical HFR of an MEA measured in a single-cell fuel cell.

4.1.2.6 Activation Procedures and Recovery

After manufacturing, MEAs typically need some kind of break-in procedure to have stable and reproducible behaviour [280]. Exactly what effects a good break-in procedure has in the MEA is debated, but several effects are suggested to occur, namely: membrane hydration, catalyst activation, and reduction of contaminants from production [280–283]. The membranes need to be humidified to obtain optimal proton conductivity. This can be achieved by introducing the MEA to a humid environment, e.g., by using humidified gases, or by running the MEA at high current densities, thus letting internal water production humidify the system. Moreover, MEAs might contain contaminants left from production. These contaminants can be reduced and removed by applying appropriate potentials, by exposing the MEA to a hydrogen-rich environment, or by flushing the contaminants out by (internally produced) water. Break-in procedures could also have a role in letting the membrane relax and get a more favourable structure, e.g., by heating up the system, which can be done by running at high power, thus having a high internal heat production. Small Pt particles, while having a large surface area, do not have the highest surface activity. By letting these Pt particles grow, by dissolving the smallest particles, and redepositing the Pt on larger particles, the Pt might settle in a more active form. This can be achieved by cycling the potential over the Pt redox point, e.g., by cycling between OCV and 0.6 V. Reported activation procedures include pre-assembly-treatments such as steaming or boiling the MEA, or post-assembly-treatments such as voltage holding at different voltages for different lengths of time (0.4–0.65 V for 4–48 h), current holding at different current densities for different lengths of time (0.1–0.5 A cm⁻² for 2–120 h), immersion of MEA with hydrogen, CO-stripping and even short-circuiting of the fuel cell [282–284]. In the work presented here, the activation typically consisted of holding the potential at potentials between 0.6 V and 0.95 V at high humidity and elevated temperatures for 10 h or until the performance was stable.

Similar methods to the activation procedure can be used before electrochemical characterisation to get more reproducible results, or, if a real stack is run, interspersed in the running schedule to regain some of the reversible losses of the fuel cell. Then it is often called a recovery procedure. An example of a recovery procedure used in **Paper I**, and **Paper III–V** is voltage holding at a low cell voltage, i.e., 0.3 V, to reduce contaminants and Pt oxides, at full humidity and high temperature to re-humidify the membrane. The latter might be extra important if the MEAs had been exposed to vacuum, as is the case when we performed electron imaging of the cathode electrode, see Section

4.2.1.

4.1.2.7 Accelerated Stress Tests

Due to the impracticality of testing fuel cell systems for target lifetimes of up to 30 000 h (which would require almost 3.5 years of continuous operation), accelerated stress tests (AST) are often used instead. The aim of using ASTs is to simulate the degradation processes of the materials during real operational conditions, so that the real degradation processes can be studied and understood, but with testing times on the order of days and weeks, rather than years. There are many different types of ASTs for PEMFCs, designed to simulate different operating conditions and separate different types of degradation effects; see Figure 4.8. ASTs can be divided into static methods, such as potential holding, or dynamic techniques such as different types of potential, humidity, or temperature cycling. Typically, it is transients between conditions that are the most detrimental to a fuel cell, rather than static operation conditions, and thus many ASTs are focussing on varying, e.g., the potential, load, or RH, to accelerate the degradation processes. For potential variations, the faster the potential shifts, the more damage is done to the system. As an example, a study by Stariha et al. [215] showed that square wave cycling leads to a five-fold increase in the degradation rate compared to triangular wave cycling in the same potential ranges, due to faster shifts in potential during square wave cycling. Uchimura et al. [285] made a similar study, where they compared different AST profiles and dwell time. They found that square-wave cycling leads to a much higher degradation rate compared to triangular wave profiles in the same potential window, while a doubling of dwell time/cycle time only had a minor impact for a given voltage profile. Furthermore, Uchimura et al. [285] found that providing the cathode with either air or N₂ had no considerable effect on the degradation rate, showing that voltage cycling is much more important regarding degradation than the gas environment at the cathode. Astudillo et al. [286] found similar results, in which the RH level was found to be much more influential on the degradation rate than the use of N₂ or air. However, when using air or O₂ instead of an inert gas, care should be taken when choosing the potential limits, as the cell voltage and the cathode potential might differ substantially due to high currents, and therefore a high iR voltage drop when air is present. As the voltage limits have a great impact on the catalyst degradation, the voltage during an air-based AST should be iR-compensated for for a fair comparison to be made between different ASTs. The OCV can also shift during the course of the experiment, due to increased rates of H₂ crossover, thus a set upper potential limit is often preferred over using the shifting OCV [286].

Voltage cycling between 0.6 and 0.95–1.0 V or OCV is often performed to simulate degradation during normal operation of a fuel cell, while voltage cycling between 1.0 and 1.5 V is used to simulate voltage spikes that can occur during SUSD events [34, 215]. Wet/dry cycling of the RH can also be used, sometimes in combination with varying voltages or loads, to study, for example, the stability of the membrane [251]. Other types of ASTs aim to simulate

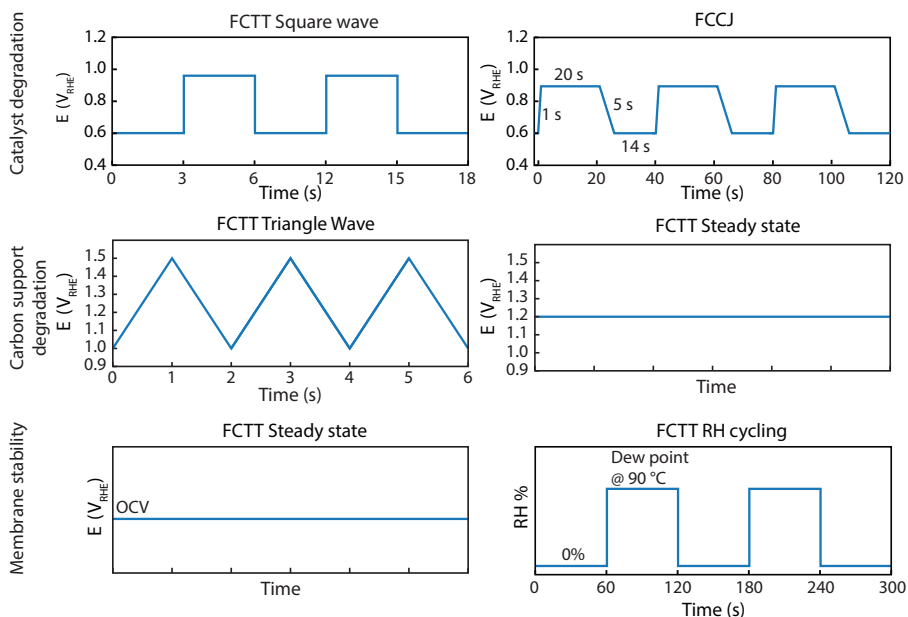


Figure 4.8: Examples of accelerated stress test protocols for fuel cell degradation, focused on studying the degradation of either the catalyst, the carbon support or the membrane. Protocols taken from [215, 288, 289].

representative drive cycles in, e.g., a city, where a vehicle would typically need to accelerate and decelerate often and idle at red lights and crossings [287].

Although the exact correlation between AST degradation and degradation rates during real operation may be difficult to establish, comparisons have been made between degradation during ASTs and degradation during several thousands of hours of regular operating. For example, a 6 000 h real world driving test with the Toyota Mirai showed remarkable similarity in degradation as after 30 000 cycles as a square wave AST with voltage cycling between 0.6 and 0.95 V, with a holding time of 3 s at each voltage [90].

4.2 Electron Microscopy

Scanning electron microscopy (SEM) is a characterisation method in which a focused beam of electrons is used to image the surface of a sample [290]. Figure 4.9a shows a schematic of an SEM. A high-energy electron beam (around 0.2 to 40 keV) is focused using magnetic lenses and scanned in a raster pattern over a sample. The electrons interact with the atoms in the sample, producing different types of signal, such as secondary electrons (SE), backscattered electrons (BSE), and characteristic x-rays. These signals can give information on the surface topography and chemical composition of the sample. Due to the difference in

energies of the SE, BSE, and x-rays, they have different mean free paths, and thus the signals will come from different depths in the interaction volume of the sample; see Figure 4.9b. SE comes from the electrons in the outer orbitals of the atoms being knocked out. SE has the lowest energy of the signals and thus only measures a few nm down in the sample. The signal strength of SE will depend, among other things, on the angle of incidence of the sample compared to that of the electron beam and will thus show the topography of the sample. BSE comes from the electrons in the electron beam being elastically backscattered from the atoms. Heavier elements backscatter electrons more strongly than lighter elements, and thus BSE gives good contrast between areas with different elements. BSE have more energy than SE, hence BSE signals originate from a larger interaction volume than SE. X-rays are produced when a lower-valence electron is knocked out of its orbit by the electron beam. A higher valency electron jumps down to take its place, and emits photons of a characteristic frequency in the process. Thus, x-rays provide information about the chemical composition of the sample. X-rays have an even longer mean free path than BSE, and thus give information from an even larger interaction volume.

SEM can be used to study samples from the macro- and microscale to the nanoscale. Under the right conditions, an SEM can reach resolutions of less than 1 nm. Due to the attenuation of electron beams under gas atmospheres, conventional SEM requires imaging to be performed under high vacuum. Furthermore, the sample being imaged should be electrically conductive to prevent charge accumulation and image distortion.

Transmission electron microscopy (TEM) works on similar principles as SEM, but instead of measuring secondary and backscattered electrons, the image is formed by detecting transmitted electrons; see Figure 4.9a [290]. Due to the de Broglie wavelength of electrons, they will interact with the specimen and form an image plane, much like a normal light microscope works. However, since the wavelength of electrons is on the order of Å, TEM can give an image resolution where single columns of atoms can be detected. Since the electron beam has to be transmitted through the samples, the samples have to be thin, preferably below 100 nm. Like SEM, TEM can be operated in different modes. Normal TEM can be used either to image the sample directly or to look at the diffraction pattern, which can give information about either the sample morphology or crystal structure.

4.2.1 Identical Location Microscopy

In identical location (IL) SEM and TEM, the same area of the sample is imaged repeatedly. These methods have the strength of being able to follow changes in the sample on the nanoscale, allowing the study of the degradation of individual particles. IL-SEM and IL-TEM can help separate effects that with normal SEM and TEM would not be distinguishable. For example, with IL-SEM and IL-TEM, different types of particle degradation, such as detachment, migration, redeposition, corrosion, and dissolution (Figure 3.11) can be clearly distinguished, which would not be possible without having an initial reference

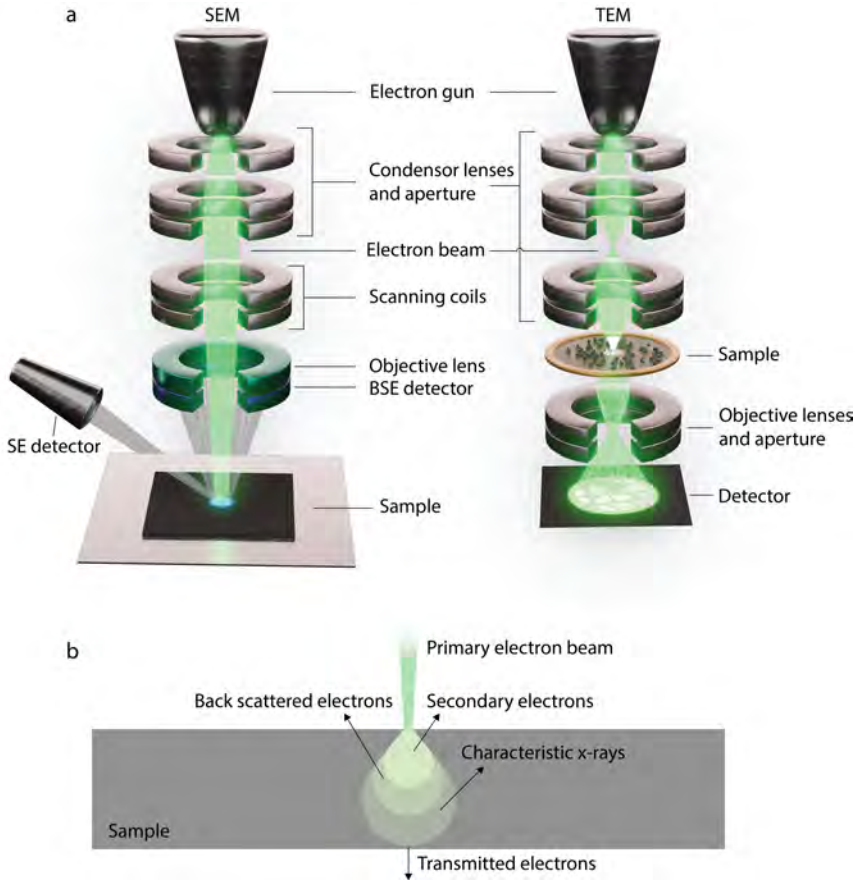


Figure 4.9: a) Schematics over a scanning electron microscope (SEM, left) and transmission electron microscope (TEM, right). In both SEM and TEM, a high energy electron beam is focused on a sample using magnetic lenses. In SEM, the beam is scanned in a raster pattern over the surface, and either scattered electrons or characteristic x-rays is detected. In TEM, the electron beam is transmitted through the sample, and the image of the sample is projected on a fluorescent screen or a digital detector. b) Interaction volume of electrons in a sample.

image to compare to. By taking several intermediate IL images during a process, the growth rate of individual particles can be calculated, and the influence of, e.g., initial defects can be studied.

IL-TEM has previously been used to study degradation of catalyst materials for PEM fuel cells [268, 291–296]. Mayrhofer et al. [291–293] introduced IL-TEM to investigate the degradation of the PEMFC catalyst and illustrated the strengths of the method by using IL-TEM to observe the degradation of standard Pt/C during potential cycling at different potential ranges. They reported that a potential cycling up to $1.4 V_{\text{RHE}}$ leads to the growth and detachment of Pt particles, with minimal corrosion of the carbon support [291, 292]. Perez-Alonso et al. [296] used IL-TEM to study Pt/degradation during voltage cycling between 0.6 and $1.2 V_{\text{RHE}}$, and concluded that Pt dissolution is the main degradation route, which led to major loss of Pt volume, with little loss of carbon support. The IL-TEM technique has been further developed by using tomography to reconstruct the 3D structure of the Pt/C catalyst, which presents a unique view of Pt degradation [294, 295, 297]. There are also examples of studies using IL-SEM to studying PEMFC catalyst degradation. Hodnik et al. [298] used IL-SEM to study the degradation of Pt/C catalyst layer during potential cycling between $0.2 V_{\text{RHE}}$ and $1.4 V_{\text{RHE}}$, and observed considerable Pt particle growth, with no noticeable carbon support corrosion.

However, it should be noted that these IL-TEM and IL-SEM studies have primarily been performed in half-cell setups such as RDE, in aqueous electrolytes, and at room temperature. The degradation rates and main degradation phenomena may differ in a real fuel cell operating at elevated temperatures, as elevated temperatures increase Pt ion mobility and carbon corrosion rates, and the gaseous environment might reduce the rate of Pt dissolution. Schlögl et al. used IL-TEM to study degradation of Pt/C during potential holds at up to $1.3 V_{\text{RHE}}$ at $60\text{ }^{\circ}\text{C}$ and $75\text{ }^{\circ}\text{C}$, and found that the carbon support degradation was considerable, which is in contrast to the results presented by Mayrhofer et al. [291, 292], Perez-Alonso et al. [296] and Hodnik et al. [298]. This highlight the need to carefully design experiments, especially when studying degradation, to ensure the operation conditions are relevant for applications. Yu et al. [268] observed differences in degradation observed with IL-TEM and degradation observed in a PEMFC MEA, and tried to overcome these discrepancies by tuning the conditions of the half-cell measurements used for the IL-TEM measurements until the results matched those of the PEMFC MEA, by, e.g., introducing Pt ions into the electrolyte, increasing the operating temperature and changing the potential cycling window, thereby effectively changing the degradation condition until the ‘correct’ types of degradation were observed.

In **Paper I** and **Paper III**, IL-SEM and IL-TEM were implemented in a real single-cell fuel cell system, and in **Paper IV**, these methods were used to study the effects of SUSD cycling on the cathodic CL.

For IL-SEM, the MEAs are constructed according to Figure 3.6 and pressed together in the fuel cell. The MEA is then removed from the fuel cell and

the GDL of the cathodic layer is gently removed, exposing the cathode CL (CCL). The MEA, without the cathodic GDL, is mounted on an in-house-built SEM stage. Conducting carbon tape is placed on the corner of the CCL, and wrapped around to connect to the metal of the stage, to allow for removal of accumulated electrons on the sample during imaging. The MEA on the stage is then inserted into an SEM instrument to image the surface of the CCL. The process of removing an MEA from the fuel cell and inserting it into SEM for imaging is shown in Figure 4.10a–i. After SEM imaging, the carbon tape is removed, the GDL is placed back on top of the CCL, and the full MEA is reinserted into the fuel cell for electrochemical evaluation. The CCL imaging process is then repeated to follow the changes in surface morphology over time. The stage used for SEM imaging ensures the same orientation of the MEA every time and, together with the use of a coordinate system in the SEM software, the same location of the MEA can be found and imaged repeatedly. By systematically imaging every area starting from low magnification and gradually increasing the magnification, the same area can be found even at magnifications up to 200 kX, without the need for any physical marking of the sample. Figure 4.11 shows an image series that illustrates how the same area is located by gradually zooming in. The image series at the beginning of life is later used as a map to relocate the same area.

Samples for TEM imaging are prepared by scraping a powder of Pt/C from the cathodic side of a fresh 3-layer CCM. The powder is dispersed in Milli-Q water and the solution is drop-casted on TEM grids, which are left to air dry, see Figure 4.12a. The TEM grids are placed between the GDL and the CCL of an MEA, constructed in the same fashion as for the IL-SEM imaging, see Figure 4.12b. After each AST session, the cathodic GDL is removed to expose the TEM grid, which is gently lifted out for imaging. After TEM imaging, the grid was placed back at the same location on the CCL, the GDL was placed back on the MEA, and the full MEA was placed in the fuel cell for electrochemical testing. The TEM grids have a notch on the edge, which helps to position the TEM grid in the same position in the TEM grid holder each time, and markings on the grid system, which help locate the same area of the sample, see Figure 4.12c. After locating the correct square on the grid, the feature to be imaged is located by gradually zooming in on the area of interest (Figure 4.12d) while comparing to reference images of the fresh sample. In this manner, the same area and features can be located without the need to introduce any markings to the sample.

4.3 Sample Preparation

A model system is a simplified and well-defined electrochemical system, used to study fundamental processes like reaction rates. In particular, in the work included here, model systems in the form of thin-film electrodes are used. By studying the behaviour of thin films with a well-defined surface area, confounding effects such as mass transport limitations, size- and shape dependence, and catalyst-support interactions can be separated, and the intrinsic activity and

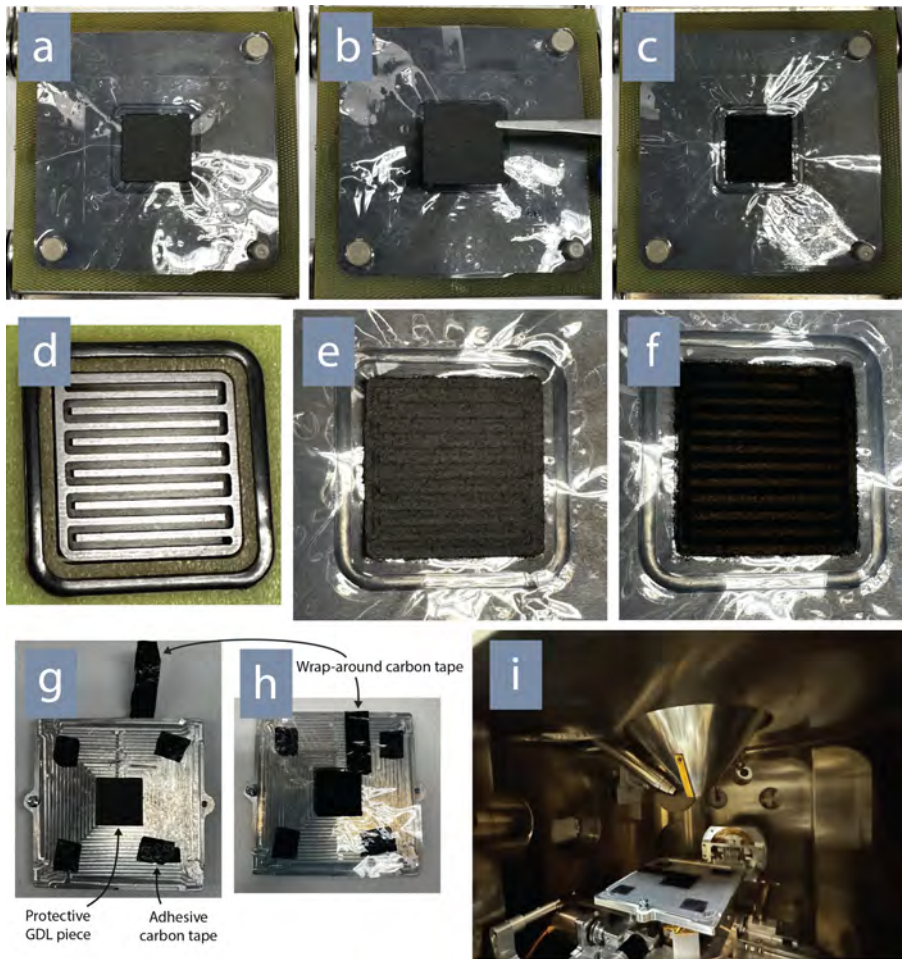


Figure 4.10: Workflow of removing an MEA from the fuel cell for imaging with SEM. a) The fuel cell is opened, exposing the full MEA with the cathode facing up. The cathodic GDL is gently removed with tweezers (b), leaving the cathodic catalyst layer exposed (c). The cathodic flow field (f) leaves visible imprints on the GDL (e) and on the top of the CCL (f). g) Double sided carbon tape for adhesion, and a protective piece of GDL is placed on an in-house-made SEM stage. h) The MEA is placed on the stage, taking care to align it with the edges, and a wrap around piece of carbon tape is attached to the edge of the cathode catalyst layer for electrical connection with the stage. i) The SEM stage with the MEA is inserted into SEM for imaging.

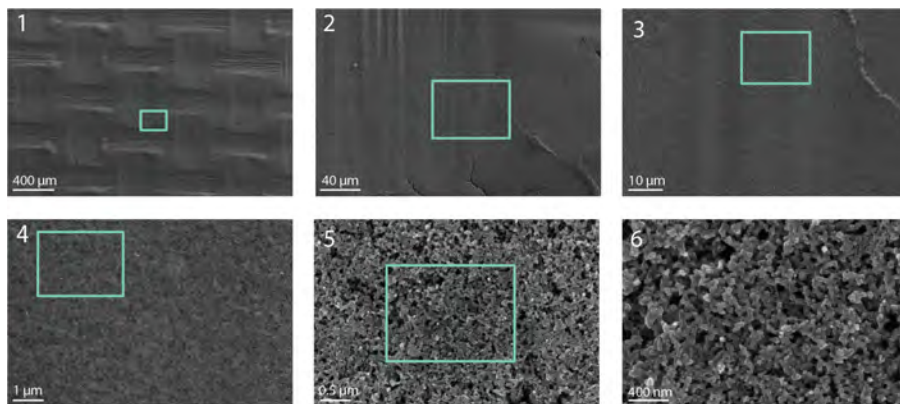


Figure 4.11: Series of SEM images from 100 X magnification up to 100 000 X magnification from a fresh sample, illustrating how the area of the sample was located by gradually zooming in. Blue rectangles show where the next image in the series was taken. This image series is later used as a map when relocating the area after AST cycling.

behaviour of the material itself can be studied.

4.3.1 Thin Film Fabrication

Electron-beam (E-beam) evaporation is a type of physical vapour deposition used to deposit thin films of materials. A beam of high-energy electrons is directed from a filament to an ingot of the target material of choice by using magnetic fields. When the beam hits the target, it will heat up rapidly until it starts to melt or sublime, leading to vapours being ejected from the surface. These vapours are used to coat a substrate. The coating thickness is measured using QCM, and E-beam evaporation can be used to create thin films with a thickness of a few Å up to several μm . This method was used in **Paper II** to fabricate 200 nm thick Pt thin films on quartz crystals, for use in EQCM measurements. To help with adhesion, a 3 nm Ti layer was deposited on the quartz crystal before the Pt layer was evaporated.

4.3.2 Preparation of Cross Sections

Cross sectional samples of CCMs (**Paper I**) and QCM crystals (**Paper II**) were produced using a focused ion beam, in which a high-energy beam of ions is used to mill the surface of a sample. The cross sections were then attached to TEM grids to later be imaged with TEM.

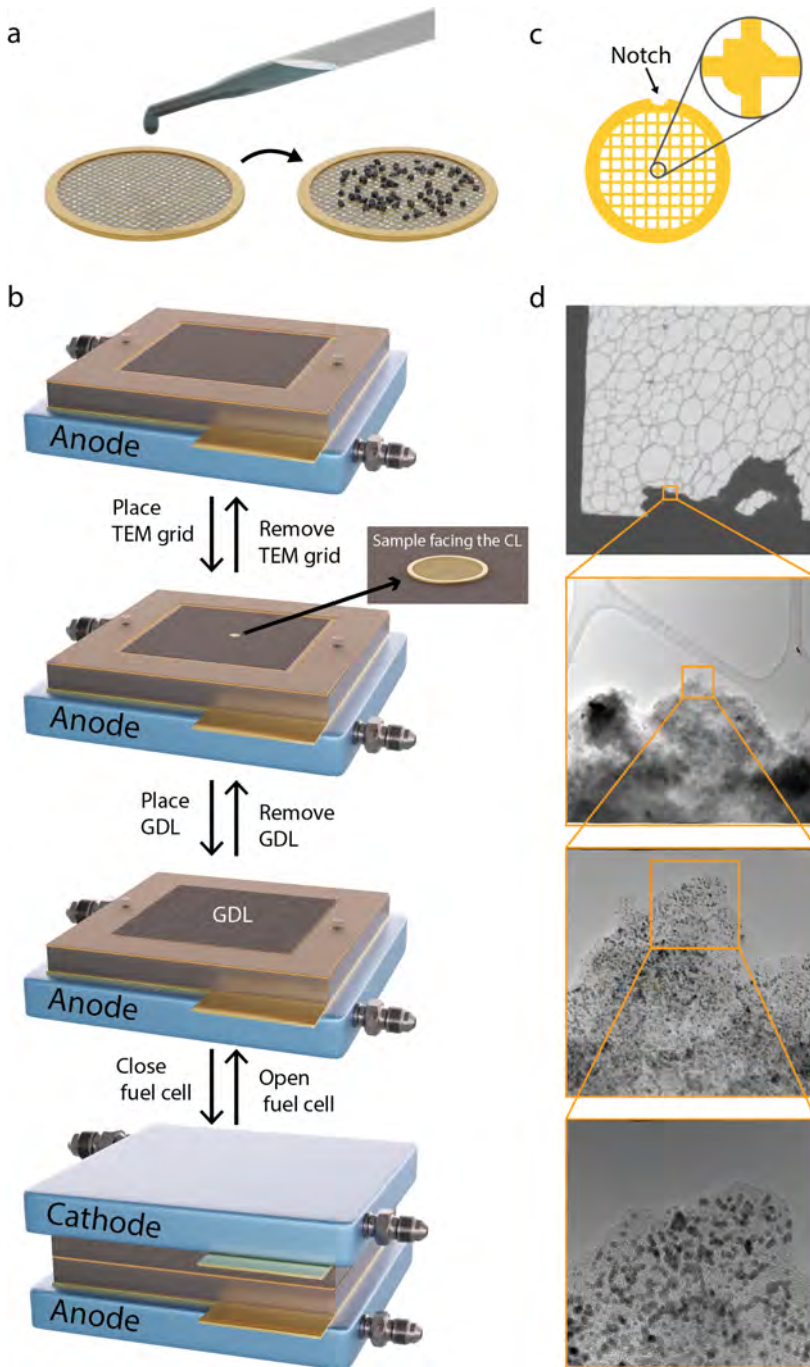


Figure 4.12: a) TEM grids are prepared by drop-casting a solution of Pt/C catalyst, and letting it air-dry. b) A full MEA is assembled and inserted into the fuel cell, with the TEM grid inserted in between the CCL and the cathodic GDL. c) A notch at the top of the TEM grids and markings in the middle of the grid helps with locating the correct area. d) A specific area of the sample on the TEM grid is located by gradually zooming in.

Chapter 5

Results & Discussion

In this chapter, I present some of the key results and discussions that form the foundation of **Paper I–V**, expanding on the analysis and connecting the dots between them. This chapter also serves as a chronicle of my own journey into the world of fuel cells and catalysis during my doctoral years. Summarising four years of work on a few pages is no easy task, especially given the many detours, challenges and dead ends along the way. Those missteps are, of course, omitted as this thesis otherwise might have been more aptly titled ‘100 Ways to Kill a Fuel Cell’. However, these challenges have been instrumental in deepening my understanding and refining the methodologies that led to the successful outcomes presented here.

5.1 Mass Response and Dissolution of Pt Thin Films

While studying catalysts in real fuel cells is invaluable for understanding degradation effects, the complexity of the samples and testing environments makes it difficult to isolate the individual contributions to performance loss and catalyst deactivation, gas transport through the catalyst support, and ion conduction through the ionomer. To address this, simplified model systems can be employed to isolate each effect, allowing for a clearer understanding of its impact on overall performance and degradation.

Paper II presents EQCM measurements performed on Pt thin films to investigate their dissolution rate and mass response behaviour in different electrolytes when scanning to different upper potential limits (UPL). The behaviour of Pt was studied in H_2SO_4 , due to its similarity to the acidic side groups of Nafion used in PEMFC. Furthermore, KOH was used to investigate how the results of Pt in acidic conditions compare with the behaviour under alkaline conditions. This comparison is motivated by ongoing research efforts to develop alkaline alternatives to PEM technologies.

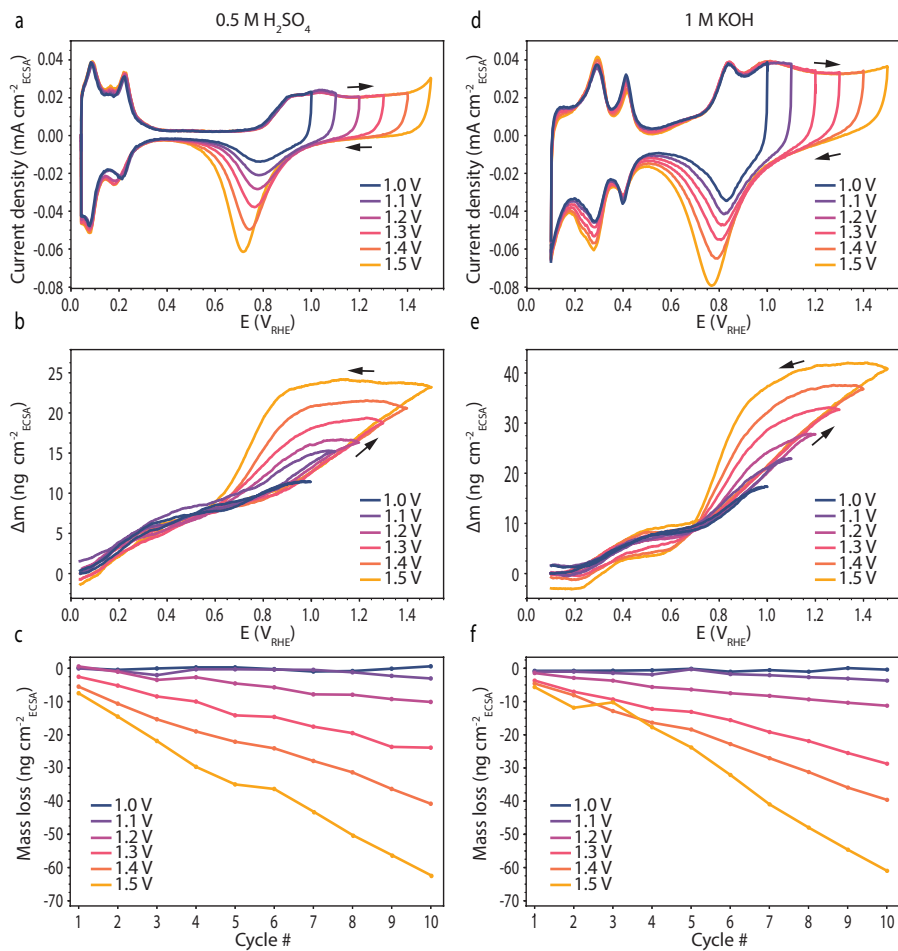


Figure 5.1: CVs, corresponding mass responses and mass loss per cycle of Pt thin films cycled to different upper potential limits in 0.5 M H₂SO₄ (a, b, and c) or 1 M KOH (d, e, and f) at 50 mV s⁻¹ and under inert atmosphere.

Figure 5.1a and b show CVs and corresponding mass responses of a polycrystalline Pt thin film in 0.5 M H_2SO_4 , measured using EQCM. The CVs are characteristic of polycrystalline Pt measured in H_2SO_4 , and show features of hydrogen adsorption/desorption, charging of the electric double layer, and Pt oxidation and reduction, as described in Section 4.1.2.1. The mass response of the Pt thin film can similarly be divided into three distinct potential regions, corresponding to the regions of different electrochemical processes in the CV.

In the first region below $0.4 V_{\text{RHE}}$, the hydrogen adsorption/desorption region, the surface mass decreases during cathodic (negative) scans, when hydrogen adsorbs. Similarly, the mass increases during anodic (positive) scans when hydrogen desorbs. This may seem counterintuitive, as one would expect the mass to increase when hydrogen is adsorbed to the surface and vice versa, but can be explained when taking into account what the EQCM actually measures. The frequency of the QCM is affected not only by the mass of the crystal or what is adsorbed to it, but also by the behaviour of the environment in the near vicinity of the surface, which will be dragged along with the vibrating surface. When hydrogen is adsorbed to the surface, heavier water molecules and other ions in the electrolyte near the surface are displaced, thus less mass is dragged along with the crystal vibration, giving an apparent decrease of mass. Similarly, when hydrogen desorbs, heavier molecules take its place, thus giving an apparent measured increase of the measured mass. This decrease during hydrogen adsorption leads to a point of minimum mass, at which all the surface have been fully covered with hydrogen and no more water is being replaced. This point of minimum mass has previously been reported for H_2SO_4 to occur at around $0.05 V_{\text{RHE}}$ [299], which is just at the edge of the potential window scanned here, and is thus not visible in Figure 5.1b.

When scanning in the region dominated by charging the electric double layer (circa 0.4 to $0.8 V_{\text{RHE}}$), the mass increases slightly due to heavier ions in the electrolyte being attracted to the vicinity of the electrode surface as the surface potential increases. After $0.8 V_{\text{RHE}}$ during anodic scans, the mass increases more rapidly due to oxidation of the surface, which proceeds in steps. First, OH ions are being bound to the surface, and at around $1.0 V_{\text{RHE}}$ PtO begins to form. The mass gained during oxidation, from $0.8 V_{\text{RHE}}$ to the UPL, scales roughly linearly with the UPL, indicating that the amount of oxide formation scales in the same fashion. When the scan direction is reversed during cathodic scans, the mass is roughly stable until a potential of $0.8 V_{\text{RHE}}$ is reached, indicating that the formed PtO is stable in this window. However, when $0.8 V_{\text{RHE}}$ is reached, the mass decreases rapidly as PtO is reduced to Pt. At about $0.6 V_{\text{RHE}}$, all oxide has been reduced, as indicated by the mass response that has reached its preoxidation value for the double layer region.

Figure 5.1c, shows the dissolution rate of the Pt thin film, during potential cycling to different UPLs, i.e., the difference in mass at the beginning of each cycle. At an UPL of $1.1 V_{\text{RHE}}$ or below, little to no mass is lost per cycle. When cycling to higher potentials, the surface starts to lose mass, and the

amount of mass lost per cycle scales with the UPL. This is in good agreement with previously reported data from Topalov et al. [235, 236] on Pt dissolution in acidic media. The mass loss comes from Pt being dissolved mainly during cathodic scans [236], when PtO is reduced back to metallic Pt. During this reduction, Pt has to settle back into its metallic state, and oxygen has to be released from within the surface layer. When the PtO layer is thin, i.e., when the total mass increase during oxidation is lower as it is for the lower UPLs, the Pt is more likely to settle back on the surface. When the PtO layer is thicker, as is the case when scanning to higher UPLs, Pt ions are less likely to redeposit on the surface, and is more likely to be dissolved and diffuse into the electrolyte. Hence, little to no mass loss is observed at lower UPLs, while more and more mass loss occurs with higher UPLs. When relating these findings to catalyst behaviour in a realistic PEMFC environment, i.e., when the potential is cycled between 0.6 and 1.0 V_{RHE} , the results in Figure 5.1c indicate that very little Pt should be lost through dissolution, while potential excursions to above 1.0 V_{RHE} would likely increase dissolution.

The characteristic CVs and corresponding mass responses of a Pt thin film in 1 M KOH is shown in Figure 5.1d and e. The CVs are distinctly different than when measured in H_2SO_4 , showing clearly how CVs are highly specific for the combination of electrolyte and electrode material. Even so, the currents in the different regions have similar characteristics and origins as when measured in H_2SO_4 , i.e., the CVs shows features from hydrogen adsorption/desorption, charging of the electric double layer, and Pt oxidation and reduction. The CVs in Figure 5.1a and Figure 5.1d are both normalised by the ECSA measured from hydrogen underpotential deposition, so the total area under the hydrogen adsorption/desorption peaks should be equal in both CVs.

At lower potentials, $<0.5 V_{\text{RHE}}$, the current peaks comes from underpotential deposition/desorption of hydrogen. Notably, these peaks are shifted towards higher potentials as when compared to the CVs in H_2SO_4 . Between circa 0.5 and 0.8 V_{RHE} , the current is coming mainly from charging of the double layer. Above 0.8 V_{RHE} in the anodic scan, the current is coming from oxidation of Pt. Notably, this current is larger per ECSA when cycling in KOH than when cycling in H_2SO_4 , indicating that more oxide is formed. Similarly, the current peak from PtO reduction during the cathodic scan is larger as well, as the current from Pt oxidation and PtO reduction should be equal. Furthermore, PtO reduction starts at higher potentials, with a small but distinct amount of current from PtO reduction present almost directly when the scanning direction is reversed.

These differences between the CVs measured in H_2SO_4 and KOH are found to be reflected in the behaviour of the mass responses (Figure 5.1e). Starting at the hydrogen adsorption/desorption, the mass response in KOH have a noticeable plateau below 0.2 V_{RHE} , not seen in this scan window for the mass response in H_2SO_4 , i.e., the mass response have a local minima of mass found at 0.2 V. This local minima of mass found in KOH is analogous to the point of minimum mass previously identified in H_2SO_4 at around 0.05 V_{RHE} [299],

which have been attributed to the point at which a full layer of hydrogen has been adsorbed to the surface. This mass plateau/minimum mass indicates that a full hydrogen layer is reached at a higher potential in KOH than in H_2SO_4 . This is congruent with the location of the hydrogen adsorption/desorption peaks in respective CVs. For H_2SO_4 , the lower peak for hydrogen desorption lays just at the limit of the scan window, at $0.05 V_{\text{RHE}}$ in Figure 5.1a, which correlates well to the previously reported point of minimum mass. For KOH, the lower peak of hydrogen desorption is found at a higher potential, around $0.2 V_{\text{RHE}}$ (Figure 5.1d), which correlates well with the higher potential of minimum mass for KOH found in the mass response reported here. As a side note, these lower peaks in the CVs are often used as limits when integrating the total hydrogen adsorption currents, and the congruence with the points of minimum mass supports the use of these peaks as well-defined cut-off points for measuring the full surface area.

The mass response also show that more mass is gained during oxidation (upwards scanning from $>0.8 V_{\text{RHE}}$) in KOH than in H_2SO_4 , corresponding to the higher current density in the CVs from the KOH in this region. Also, during PtO reduction (when scanning down from the upper potential limit to $0.6 V_{\text{RHE}}$), the mass reduction for KOH starts more or less immediately, albeit at a slower pace in the beginning, in contrast to the mass plateau seen in H_2SO_4 . This is in agreement with the earlier onset of reduction current for the KOH CVs compared to the H_2SO_4 CVs.

Based on the larger amount of mass gained during oxidation in alkaline electrolyte, one might be lead to think that Pt would be more prone to dissolution in alkaline environments, since when more PtO is formed and reduced, the likelihood of Pt redepositing should be decreased. However, that is not what was observed here. Despite the differences in behaviour of the CVs and mass response between Pt measured in H_2SO_4 and KOH, the dissolution rate per cycle and per UPL is comparable in either electrolyte, see Figure 5.1 c and f. As in H_2SO_4 , no dissolution is observed in KOH when cycling to $1.0 V_{\text{RHE}}$. At $1.1 V_{\text{RHE}}$ and above, the dissolution rate scales with UPL, and the values are similar for both H_2SO_4 and KOH. This indicates that the stability of Pt is similar in either electrolyte, and that the potential ranges at which the cell is operated are much more impactful to lifetime and degradation rather than the pH.

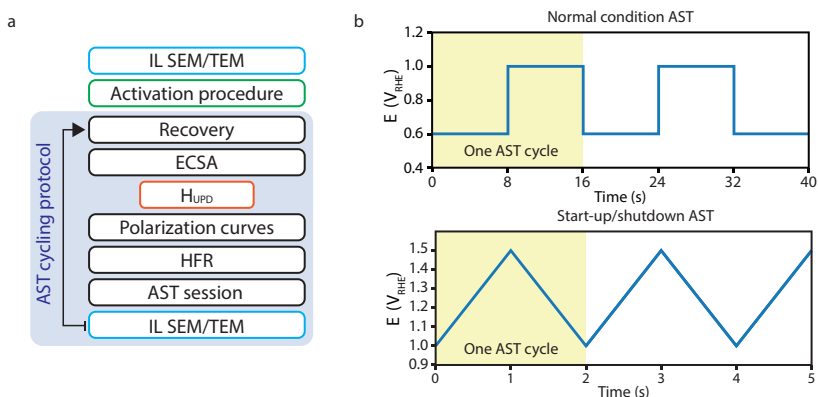


Figure 5.2: a) Test protocol for IL-SEM/TEM studies. b) AST profiles for simulating normal operation conditions (upper) and start-up/shutdown conditions (lower).

5.2 Identical Location Electron Microscopy

The remainder of this thesis is focused on investigating MEAs within a single-cell fuel cell, with a particular emphasis on the cathode electrode. The cathode is the focus in this thesis because it endures the most severe operating conditions, particularly regarding electrochemical potentials and potential cycling, making it one of the key components that limit the fuel cell's lifetime.

Degradation of commercially available MEAs was studied under different operation conditions in a test station equipped with a 5 cm² single-cell fuel cell. The test station, detailed in Section 4.1.1.3, was designed and constructed in-house during this thesis work. Over the course of the research, the station has undergone continuous updates and improvements. Similarly, the electrochemical protocol has been refined to achieve more consistent and reliable performance. As a result, while the absolute performance data may not be directly comparable across all experiments, overall trends still tell a story. For details on the experimental procedures, the reader is referred to **Paper I, III-V**, but a brief overview of the experimental protocol is included here for the convenience of the readers.

For IL microscopy, samples for IL-SEM and IL-TEM were prepared according to Section 4.2.1. After initial imaging, these samples were inserted into a 5 cm² fuel cell with the surrounding control system as described in Section 4.1.1.3. Before stress testing, each MEA was subjected to a conditioning procedure until a stable performance was achieved, after which the initial electrochemical performance was characterised. After, the samples were subjected to an AST cycling protocol, including recovery procedures, electrochemical characterisation, AST sessions and IL-SEM/TEM imaging. An overview of the protocol is shown in Figure 5.2a, and a full description of the experimental method can be found in **Paper I, III and IV**.

5.2.1 Method Verification

Fuel cell degradation studies where the the MEA has been disassembled and imaged under vacuum mid-run with the MEA being reinserted into the fuel cell for further testing had not previously been presented to the best of our knowledge. To ensure the imaging process itself did not cause extra harm to the sample, and that only the AST cycling was causing the degradation of the samples, several test runs were performed with and without intermediate fuel cell disassembling or electron imaging.

Figure 5.3 shows two test runs that were performed using AST cycling between 0.6 and 1.0 V: one with intermediate IL-SEM imaging, and one reference run without any disassembling or intermediate SEM imaging. Both experiments were performed on MEAs from the same batch, in the same set-up and using the same running procedure, giving similar starting points of the polarisation curves, HFR and CVs. Electrochemical characterisations from the two runs show little discernible differences in degradation, neither in polarisation curves, HFR, CVs, or ECSA. The HFR is quite unstable for both runs, where the test without IL-SEM shows some trends of an increase in HFR, which is not seen for the test run with IL-SEM. Furthermore, the the run without IL-SEM has a slightly better performance at high current densities, i.e., where mass flow limitations are more prominent, at BOL compared to the run with IL-SEM, but at the end of life (EOL), the two samples exhibits remarkably similar performance. The absolute ECSA is a few percent lower for the sample run with IL-SEM at BOL, but when looking at the relative decrease of ECSA, the behaviour is almost identical between the two runs. Furthermore, the difference between the two samples is in the range of what we would normally see between two samples of the same batch from this specific producer, with this version of the setup and running procedure.¹ Overall, the electrochemical data shows no significant differences between the sample run with and the sample run without IL-SEM and, in particular, no tendency for the sample run with IL-SEM to degrade any more than the sample run without IL-SEM or disassembling. It should be noted that MEAs exposed to SEM imaging, and thus was exposed to vacuum, typically exhibit poor performance right after reinsertion. However, after a recovery procedure involving low potential holds and exposure to fully humidified gases at elevated temperatures, they typically regained their pre-SEM imaging performance. This could be explained by the membrane being dehydrated by the exposure to vacuum, leading to poor ion conductivity, which is reversed by exposure to high humidity levels. The same recovery procedure is performed for all samples either way, to regain recoverable losses after each AST session. From this we conclude that disassembling the fuel cell, removing the cathodic GDL, and imaging the MEA under vacuum do not lead to considerable degradation of the electrochemical performance and that the behaviour we see of the CL via IL-SEM is indicative of the true degradation processes.

¹Much of the set-up, including the cell house and the supplier of the MEAs were later changed and the experimental protocol was modified and optimised to produce more consistent results.

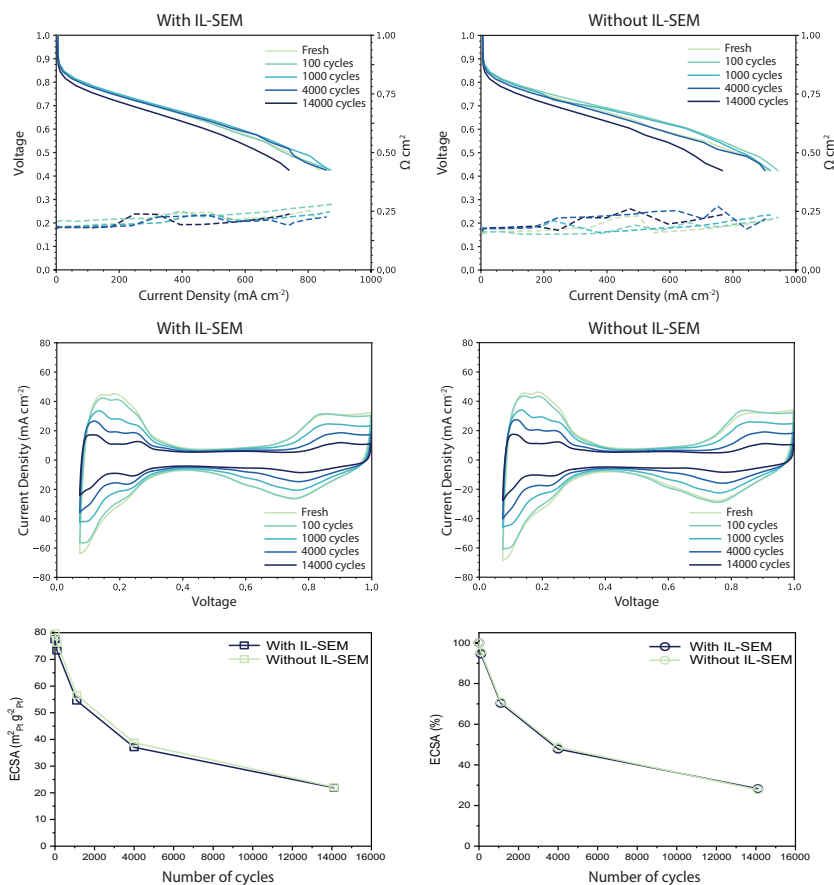


Figure 5.3: Polarisation curves, high frequency resistance, CVs and ECSA for an experimental run with intermediate IL-SEM, and a reference run without intermediate IL-SEM.

5.2.2 Pt Dissolution and Particle Growth

As a first test of the capabilities of the IL microscopy methods, we chose to study the degradation of a well-studied system, using commercially available MEAs (industry standard Pt/C catalyst with PFSA based ionomer and membranes) and a commonly used stress test meant to mimic regular fuel cell operation, with voltage cycling between circa 0.6 and 1.0 V. See **Paper I** and **III** for experimental details. This type of AST will here be referred to as a normal operation AST.

Figure 5.3 shows typical fuel cell degradation during normal operation, with a gradual decline of performance, as seen by the voltage loss, and a relatively stable resistance. The CVs in Figure 5.3 are typical of CVs measured in a fuel cell environment, and show similar peaks to the CVs in Figure 5.1a measured in H_2SO_4 , albeit with slightly less pronounced peaks for hydrogen desorption/adsorption. Over the course of the AST cycling, the CVs demonstrate a considerable decrease in the hydrogen desorption/adsorption peaks and platinum oxidation/reduction peaks, with a relatively stable double-layer capacitance. The decrease in H_{UPD} area indicates a considerable decrease in available Pt surface area, or ECSA. The total loss of ECSA was quantified from these H_{UPD} peaks, and is shown in the bottom row of Figure 5.3. The initial surface area is around $80 \text{ m}^2\text{g}_{\text{Pt}}^{-1}$, and declines steeply in the first 1000 cycles. The ECSA continues to gradually decrease until the EOL to around $20 \text{ m}^2\text{g}_{\text{Pt}}^{-1}$. This is a typical decay pattern observed for the standard Pt/C catalyst. This large ECSA loss of 75% might, at a first glance, seem much more severe than the minor decrease of performance that the polarisation curves show, but this can be explained by looking closer at the correlation between ECSA loss and polarisation loss. First, we examine the current densities. To simplify, we consider a case where we have lost 90% of the initial ECSA, i.e., $1/10^{\text{th}}$ of the initial Pt surface area is left. To achieve the same total current as the performance of the beginning of life (BOL), it follows that the current density per Pt surface area must increase by a factor of 10. The Tafel slope tells us exactly how much the overpotential must increase in order to increase the current by a factor of 10, and for ORR measured at $80 \text{ }^\circ\text{C}$, the Tafel slope is predicted to be around 70 mV dec^{-1} [145]. Thus, if we lose 90% of our initial surface area, the Tafel slope predicts that the voltage would decrease around 70 mV for a given current density. With this in mind, the voltage loss observed here is in good agreement with the concurrent decrease of ECSA.

IL-SEM imaging shows how the structure of the cathodic catalyst layer changes during the AST at different magnifications, see Figure 5.4. At $100 \times$ magnification², on the $100 \text{ }\mu\text{m}$ scale, the catalyst layer shows grid-like patterns, made of indentations left over from the MEA production process. Possibly, these MEAs were made by decal transfer and hot pressing, and the pattern observed on the MEA is the moulded outline of the woven substrate used for

²Although magnification technically refers to the enlargement of an image when displayed at a specific size, it is used here to provide a relative indication of how much the images have been magnified relative to each other.

the transfer. In either case, these large-scale structures show no noticeable change over the course of the AST. At a magnification of 15 kx, the sponge-like porous structure of the carbon support begins to be noticeable. No significant changes can be seen during the duration of the AST on this scale either.

At very high magnifications, of 250 kx, the primary particles of the carbon support can clearly be seen, as light grey spherical structures that form aggregates. Some larger Pt particles can also be distinguished as bright white dots. An important thing to note here is that the SEM has a detection limit of about 4–5 nm, and that the Pt catalyst is typically 2–5 nm in diameter. Thus, we did not expect to see the smallest Pt particles, and only larger Pt particles or Pt clusters can be distinguished in the SEM imaging. Some stringy features can also be seen between the carbon particles, which is the polymer ionomer used as a binder and ion conductor. At this high magnification, some changes throughout the AST start to be discernible. The most noticeable one is the increase in the amount and size of the bright white Pt particles at the EOL. The Pt particles that were too small to be discerned at the BOL have grown large enough over the course of the AST to be visible by SEM.

Looking closer at cut-outs of high-magnification images (Figure 5.5), more effects can be discerned on the catalyst layer. For Pt particles, they can be seen to move, grow, merge, and disappear. While the carbon support is mostly stable, some deformation and movement of carbon spheres in relation to neighbouring particles can be seen. The Pt particle growth comes from repeated oxidation and reduction of the Pt, leading to the dissolution of smaller particles and the redeposition and growth of larger particles, as well as the migration and coalescence of particles. Although carbon corrosion should not be prevalent at these cell voltages, the minor deformation of the carbon support could come from pressure within the cell and mechanical stress, possibly due to repeated humidification cycling or mechanical handling during SEM imaging.

While some effects on the degradation and ageing of Pt particles can certainly be seen in the SEM images, it should be kept in mind that we still miss information on the smallest Pt particles. Naturally, many large Pt particles at the EOL as seen in Figure 5.5 did not spontaneously emerge. Instead, this is an indication that numerous smaller Pt particles are present in the area at the BOL. During the AST, these particles grow and merge, forming particles and particle clusters large enough to be seen with the SEM. Thus, our conclusions are skewed to what is observed for larger particles, which should only make up a fraction of our sample. Hence, the next step in our journey of IL microscopy is to introduce TEM imaging, to observe what happens with these smaller Pt particles.

Figure 5.6 shows IL-TEM images of the Pt/C during normal operation AST. In the TEM images, the carbon support can be seen as a light-grey mass, while the Pt particles show up as dark-grey or black spheres. On a larger scale, the Pt/C seems stable stable, with no loss of or deformation of the support structure. Looking closer at the Pt particles, they can be seen to migrate and merge to form larger Pt particles and clusters. Some particles seem to have

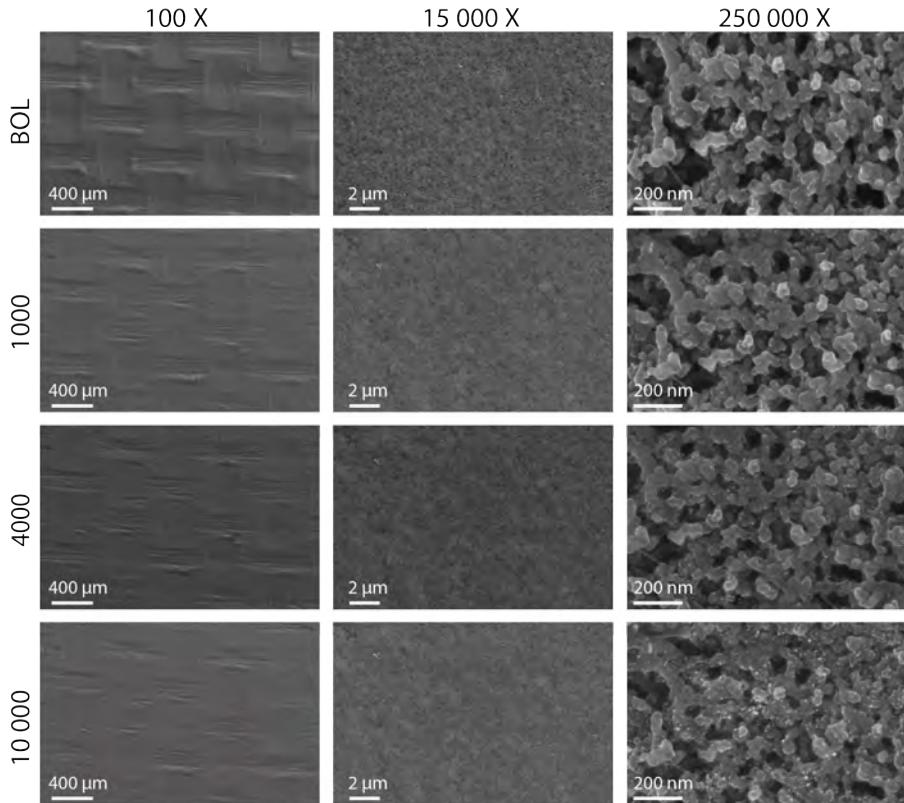


Figure 5.4: IL-SEM images from BOL, and after 1000, 4000, and 14000 total AST cycles between 0.6 and 1.0 V at 100 x, 15 kx, and 250 kx magnification.

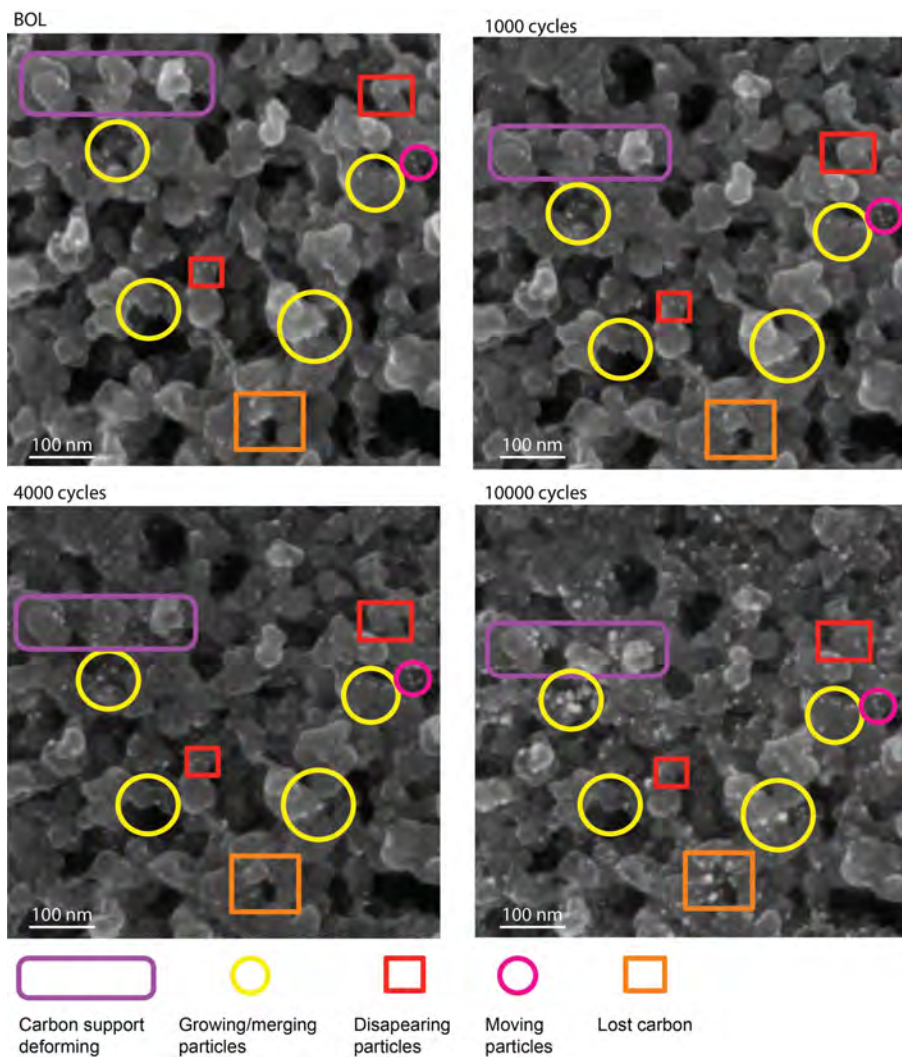


Figure 5.5: High magnification SEM images at BOL and after 1000, 4000, and 14 000 normal condition AST cycles. Markings on the figures are a guide for the reader to highlight some of the changes of the catalyst layer that can be seen throughout the AST. These markings are not comprehensive.

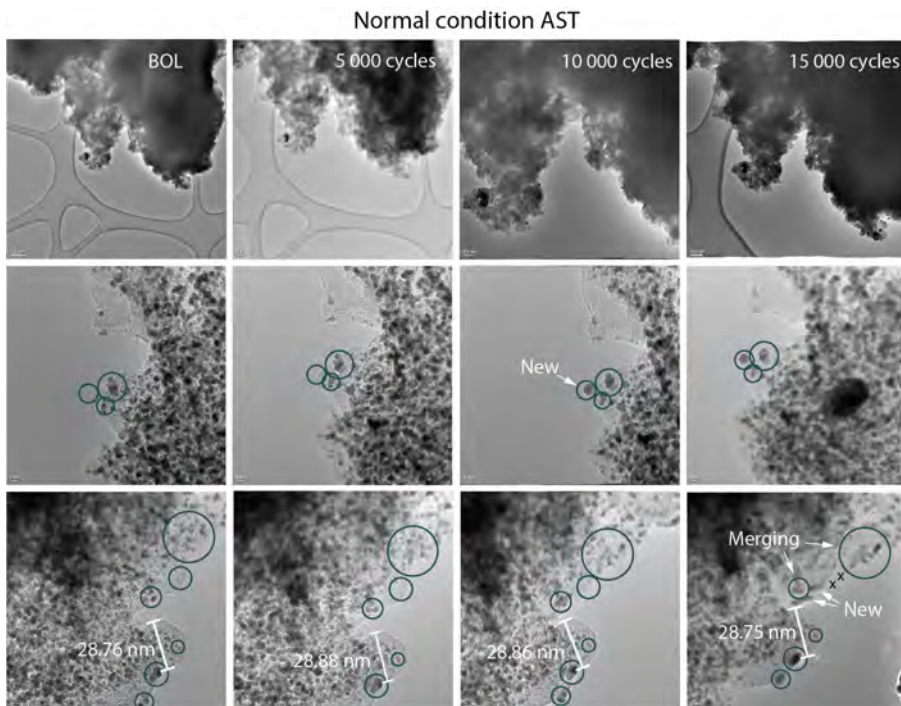


Figure 5.6: IL-TEM images showing the degradation of Pt/C during normal conditions. The carbon support can be seen as light grey mass, while Pt shows up as darker black particles scattered throughout.

detached, and on some occasions new particles emerge. Possibly these particles have detached from another area. Some of these effects are highlighted in the figure. The carbon support show some minor deformation (e.g., change in angle and relative position between primary carbon spheres and clusters), but no considerable loss of volume. Some larger ionomer agglomerations are seen to shrink throughout the AST.

High-magnification IL-TEM images of the Pt/C catalyst (Figure 5.7), show how some Pt particles are seen to merge, grow, and detach in more detail. Mostly, Pt particles can be seen to move toward each other and merge into larger particles. Some particles have disappeared between cycles, either by detaching or by moving far away and merging to form larger clusters. Some changes can also be seen on the outline of the carbon support.

This growth of Pt particles was quantified by measuring their average diameter from the IL-TEM images. Figure 5.8 shows the Pt particle size distributions (PSD), and the inset in Figure 5.8 shows the corresponding average sizes together with the ECSA. At the BOL, the Pt particles are between 2–6 nm in diameter, with an average of about 3.4 nm. Looking back at the SEM images, most of these particles seen with TEM (smaller particles <4 nm) would not

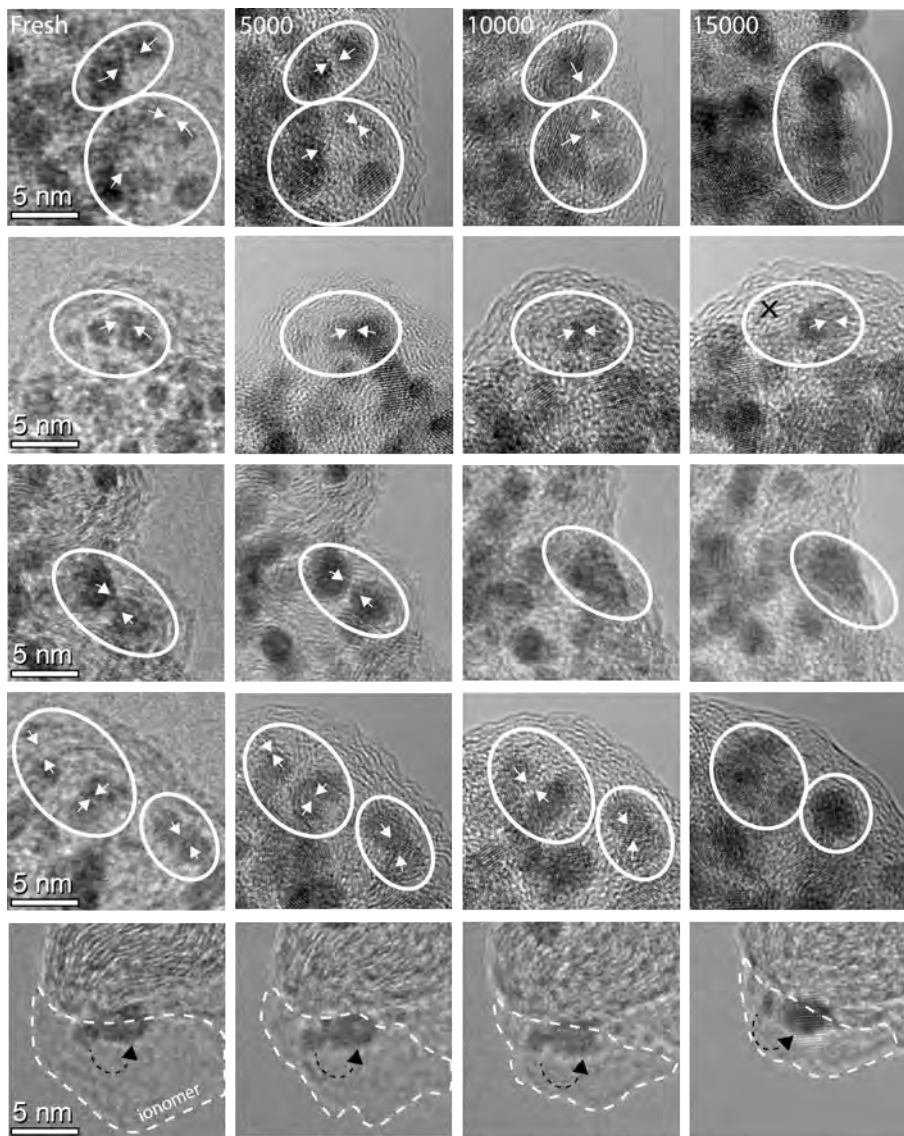


Figure 5.7: IL-TEM images, showing Pt particles migrating, coalescing and growing by Oswald ripening, and ionomer vanishing.

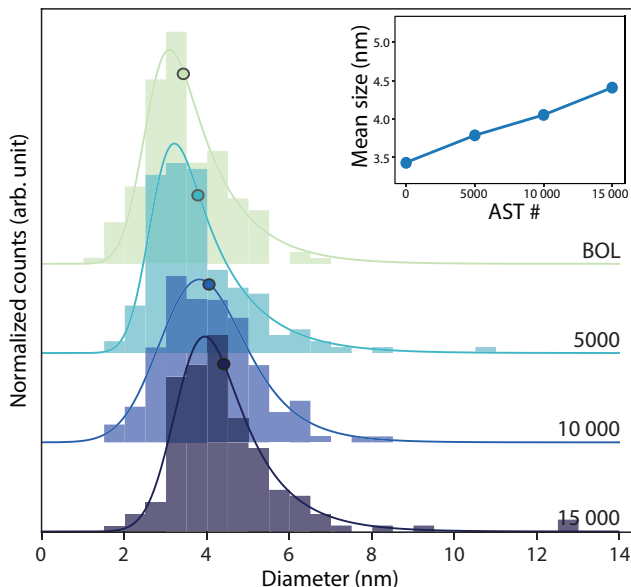


Figure 5.8: Pt particle size distributions from BOL, and after 5000, 10 000, and 15 000 normal operation AST cycles. The particle size distributions have been fitted with a log-normal distribution. Inset show mean Pt particle diameter and ECSA.

be discernible with SEM. Only a minority of the particles (larger particles >4 nm) might be visible, congruent with the few larger particles seen in the SEM images and the BOL. The average particle size increases linearly with the number of cycles, and at the EOL, the average particle size of Pt is around 4.4 nm, with a growth of around 30%. This particle growth is in part responsible for the loss of ECSA.

Overall, the loss of performance during normal operation AST can be explained by the decrease in ECSA, which in turn is explained by the growth of Pt particles induced by repeated potential cycling. The IL-SEM and IL-SEM microscopy show relatively minor degradation of the Pt/C catalyst, with a mostly stable carbon support, and Pt particles that slowly grow mainly by migrating and coalescence. These effects themselves are well-known to occur, but our results demonstrate the feasibility of implementing IL microscopy inside a real single-cell PEMFC under realistic fuel cell operation conditions.

5.2.3 Carbon Support Degradation

With the IL microscopy methods established, we wanted to test their strength by applying them to another type of AST test to see if a different mode of catalyst degradation could be observed under other operation conditions. For this, another set of measurements was performed, once again on industry standard Pt/C catalyst on PFSA type membrane, but this time with an AST

meant to mimic the effects of uncontrolled start-up or shutdown events, where the potential can spike up above the typical operation window. These results are presented in **Paper III** and **Paper IV**. In these measurements, the cell voltage was cycled between 1.0 and 1.5 V, where carbon corrosion is prevalent and severe fuel cell degradation is known to occur. This type of AST will be here referred to as SUSD AST.

A major difference in the effects of the SUSD AST and the normal operation AST is immediately apparent when looking at the polarisation curves and the HFR, see Figure 5.9. During the SUSD AST, the degradation and polarisation loss is severe, with a noticeable decrease in performance seen already after a few hundred cycles. After 500 cycles, the voltage at 1 A cm^{-2} has decreased from 724 mV at the BOL to 667 mV. One can note that this is already close to the 10% loss often used as an end-of-life target. Further cycling leads to even more severe degradation, with some stabilisation in (lack of) performance seen between 4000 and 10 000 cycles. A considerable increase in HFR can also be seen, with the HFR more than doubling at the EOL.

Interestingly enough, while the CVs (Figure 5.9 b) show a decrease in ECSA, the total loss of ECSA (Figure 5.14 b) is less severe than what was seen during the normal AST cycle in Figure 5.3, with about 65% of the ECSA lost after 10 000 SUSD AST cycles. As discussed above, this level of ECSA loss would only explain less than 70 mV of polarisation loss, far from the severe polarisation loss observed here.

By plotting the voltage loss per ECSA for different current densities (Figure 5.9c), it becomes clear that the voltage decay is much more severe than the -70 mV dec^{-1} loss predicted by the Tafel slope. This is true for all current densities but becomes more pronounced at higher current densities. Thus, ECSA losses are not the main contributor to the performance loss seen in Figure 5.9a. As cell resistance increased considerably during the SUSD AST, it is of interest to look at the contribution of the resistance to the voltage loss as well. Figure 5.9d shows the *iR*-corrected voltage loss vs. the specific current density (that is, the current per Pt surface area), which also should follow a loss of -70 mV dec^{-1} if the surface area decreases combined with resistance increase is the main contributor responsible for the decrease in voltage. For low current densities, at 0.01 A/cm^2 , the voltage loss in Figure 5.9d follows the 70 mV dec^{-1} loss much more closely than for the not *iR*-corrected data in Figure 5.9c. However, for higher current densities, the voltage loss only follows the -70 mV dec^{-1} trend for a few hundred cycles before it deviates strongly. Thus, while ECSA losses in combination with an increase in resistance can explain the voltage loss in the low-current region, other losses are dominant at higher current densities. Possibly, this is an effect of mass transport limitations, which becomes more noticeable as the current densities go higher.

Considerable differences in ageing behaviour between the normal operation AST and the SUSD AST are also apparent when looking at the IL-SEM images from the SUSD AST. Figure 5.10 shows the degradation of the CCL during an SUSD AST. Initially, the CCL surface is smooth, with some minor defects in

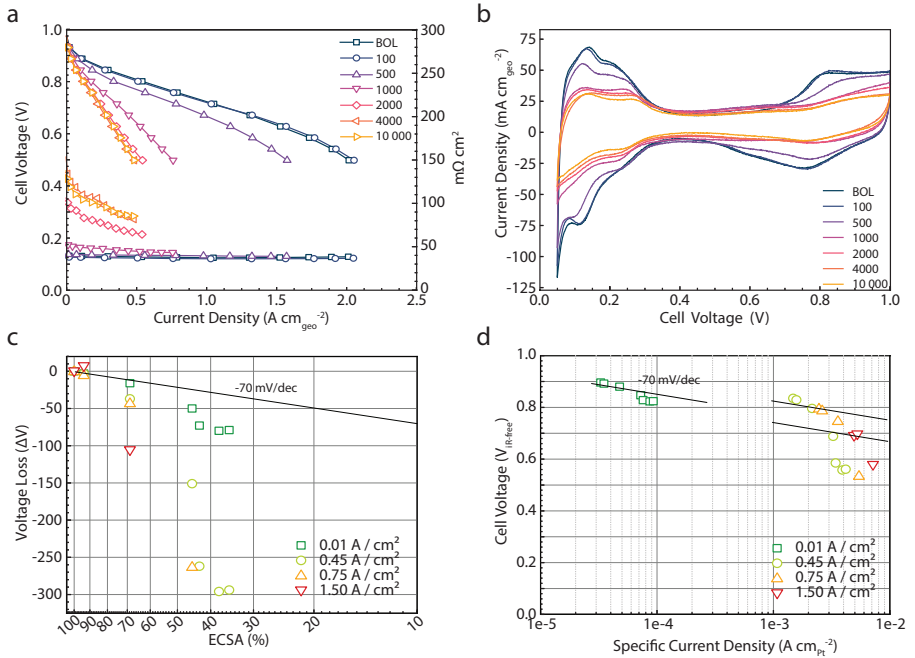


Figure 5.9: a) Polarisation curves and HFR and b) CVs during start-up/shutdown AST cycling. c) Voltage loss vs. ECSA loss for different current densities. d) iR -corrected cell voltage vs. specific current densities for different current densities. Lines with a slope of -70 mV dec^{-1} have been included in c) and d), which is the expected loss if voltage decrease comes only from loss of surface area.

the form of bumps or small cracks, either caused by the production process or mechanical handling pre-experiment. As a side note, the large-scale structure of the CL is different from the CL seen in Figure 5.4, since the MEAs used for this measurement series probably were produced by spray coating rather than decal transfer. High-magnification SEM imaging once again shows the porous structure of Pt/C, with some Pt particles distinguishable.

During SUSD AST, severe structural degradation can be observed with IL-SEM early in the process, even at the 100 μm scale, at 500 x magnification. Already after 100 SUSD AST cycles, the CCL surface shows signs of ageing, as some cracks present at the BOL have increased in size, and new cracks have emerged on the surface. These cracks are on the order of 100 μm long and 1 μm wide. After 500 cycles, more cracks have appeared and the size of the cracks has increased considerably, and the cracks are present throughout the entire surface of the CCL. These cracks have now grown so wide, ~ 10 μm , that the underlying membrane is visible, a clear sign that the cracks extend throughout the CL. Further SUSD AST cycling causes the cracks to grow wider, now ~ 50 μm wide, to the point that individual islands are formed in the CCL, which are not in contact with each other. Looking closely at the edges of these CL islands, they seem to have delaminated from the membrane underneath. This was confirmed by cutting cross sections through an aged MEA with FIB and imaging the cross sections with SEM, see Figure 5.11a. The cross section is cut over a crack in the CL and shows how the CL has delaminated from the membrane at the edge of the island near the crack. It should also be noted that while some cracks were already present in the fresh sample and that these cracks did grow over time, after 500 SUSD AST cycles these cracks did not seem to grow more severe than the numerous new cracks that had formed on the initially defect-free surface. Thus, initial defects do not appear to be a major factor in the severe degradation seen during the SUSD AST.

At 10 kx magnification, the ageing process is seen to affect the entire surface of the CCL, including the surface between the larger cracks. Smaller cracks and pits, around 10 μm long and 1–5 μm wide, forms and grows throughout the SUSD AST over the entire CCL surface. The structure of the Pt/C is, furthermore, severely degraded on the nanometre scale, visible at 250 kx magnification. Although the carbon support initially consists of spherical primary carbon particles forming a porous structure, this structure is severely affected after 500 cycles. Most of the carbon particles are no longer spherical, but have eroded to form more irregular jagged structures. With that, the pores between the carbon particles have also been affected. If similar deformation of the microstructure occurs all throughout the CL, it could indicate a loss of porosity which would contribute to mass transfer resistance. This is in line with previously published data, where the porosity of the CL has been observed to decrease. Mass-transfer resistance could also arise from loss of hydrophobicity which is known to occur due to carbon corrosion [300], which would increase issues of water accumulation and flooding [301], which would further be exacerbated by a decrease of porosity.

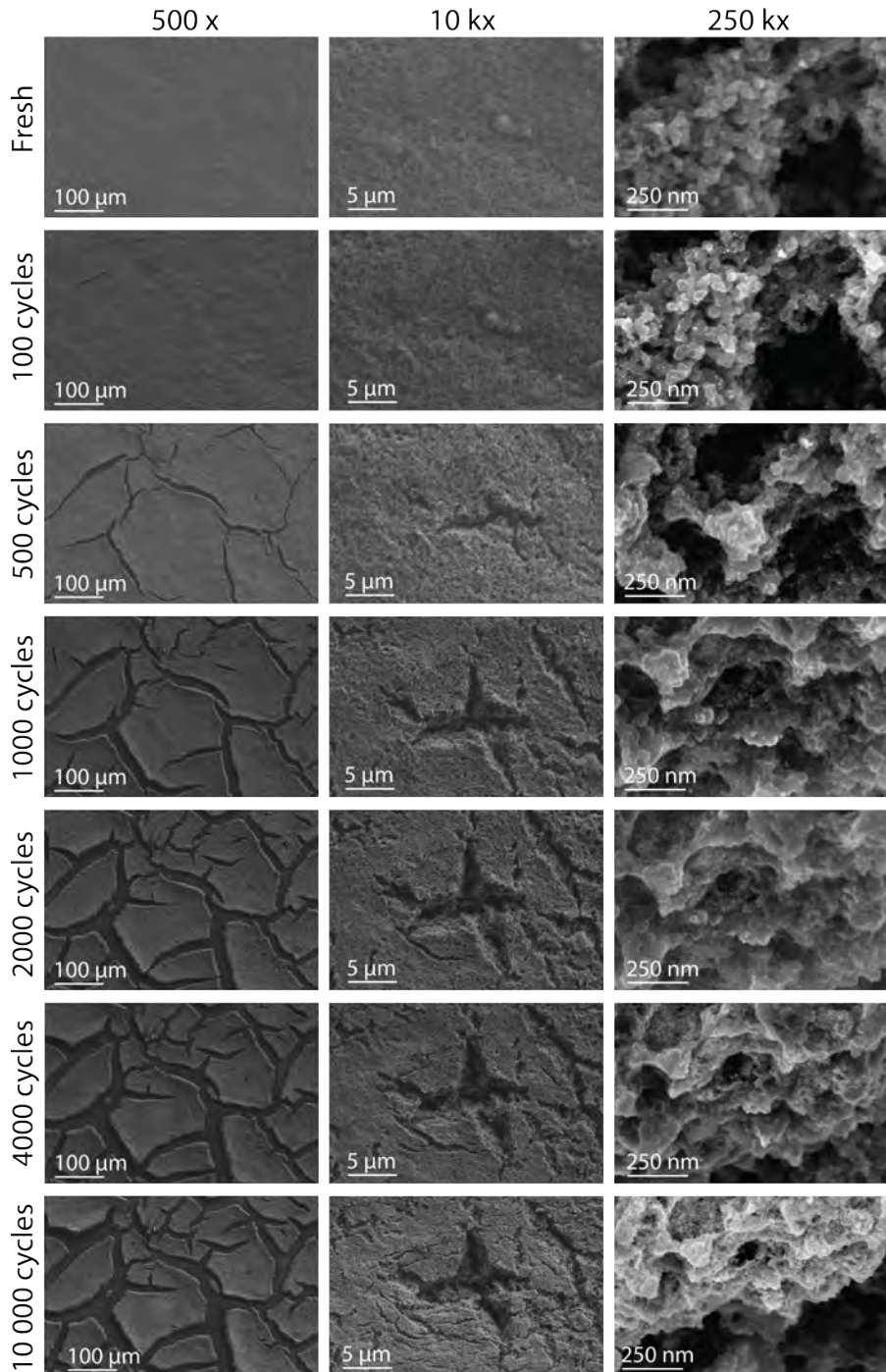


Figure 5.10: IL-SEM images showing the CCL at BOL, and after 100, 500, 1000, 2000, 4000, and 10 000 total SUSD AST cycles.

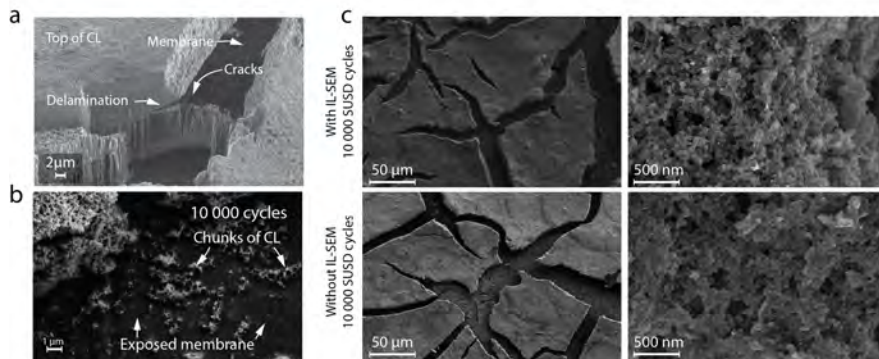


Figure 5.11: a) Cross section of MEA cut with FIB, showing how the CL is delaminating from the membrane near the cracks. b) Chunks of Pt/C catalyst are found laying on the exposed membrane exposed in the cracks. c) SEM images of the CCL surface after SUSD AST, of an MEA run with (upper row) and an MEA run without (lower row) prior disassembling or IL-SEM imaging. Both MEAs show similar types of degradation and deformation on both the microscale and the nanoscale.

A closer look at the cracks and the exposed membrane underlying (Figure 5.11 b) shows chunks of the catalyst layer that lay on the exposed membrane, without physical contact with the rest of the catalyst layer. Because these Pt/C chunks have no physical contact with the rest of the CL, they are not available for electrochemical reactions, and any Pt catalyst left on them is essentially lost.

As no crack formation or surface deformation was observed in the IL-SEM imaging during the normal operation AST, they are not caused by repeated hydration/dehydration cycles due to the vacuum during SEM imaging. To further confirm that the crack formation and severe CL degradation was caused by the SUSD AST, another MEA was run under the same conditions, but without any disassembling or SEM imaging during the SUSD AST. This MEA was imaged at the EOL, and showed similar features to the MEA run with IL-SEM, see Figure 5.11c.

Similar severe degradation of the carbon support is seen during IL-TEM imaging, see Figures 5.12 and 5.13. In the IL-TEM images, the carbon support is observed to lose volume, as indicated by some marked measurements in Figure 5.12. This loss of volume deforms the carbon support and cause it to lose its initial structure. The loss of carbon also occurs near weak points in the porous structure, leading to the weak points breaking off. This can be seen after a few hundred cycles, where some large chunks of catalyst break down, and later during the ageing, where much of the carbon structure collapses on itself. This collapse of the primary carbon particles that initially form the porous structure in the catalyst layer necessary for gas transportation indicates

a loss of porosity within the catalyst layer. The larger structures breaking at the beginning of the process can be compared with the cracks that were formed in the CL, see Figure 5.10, as the cracks could be instigated at weak points within the CL, and later to chunks of catalyst that were seen on the membrane, see Figure 5.11.

The severe degradation of the carbon support coincides with a considerable growth of Pt particles, which is particularly noticeable as there are many large Pt particles (>20 nm) present at the EOL. No such large particles were observed after the AST cycle under normal operation conditions, see Figure 5.6. This Pt growth was quantified by measuring how the particle size distribution changed during the SUSD AST, see Figures 5.14a and b. These particle size distributions were measured from more than 500 particles for each point in time from the same areas in the IL-TEM image series. The Pt particles grow from about 3.4 nm to around 5.4 nm, which is considerably more than the growth observed during normal operation AST (Figure 5.8), furthermore, the Pt grows rapidly during the initial cycles, and thereafter the rate of Pt growth slows down. Possibly, the shrinkage of the underlying carbon support reduces the distance between the particles, forcing the Pt particles closer, thus promoting coalescence and agglomeration. Compared to previously reported IL-TEM imaging of Pt/C catalyst degradation during SUSD conditions, performed in liquid half cells at room temperature, the results presented here indicate a much more severe deformation of the carbon support and loss of carbon volume [302]. Possibly, the increased rate of carbon corrosion could be an effect of the elevated temperature. In either way, this highlights the need to carefully design experiments and perform degradation studies under application-relevant conditions.

The crack coverage, that is, the amount of visible CL surface that had cracks or visible membrane, was measured from the IL-SEM images, in an attempt to characterise the propagation of crack growth, see Figure 5.14c. Cracks form and grow rapidly during the first 2000 cycles, after which the crack propagation slows down. During the last 6000 cycles, between 4000 and 10 000 cycles, the crack coverage stabilises. This behaviour is similar as seen with the decrease in performance, which worsens fast up to circa 2000 cycles, and stabilises between 4000 and 10 000 cycles. In particular, the increase in resistance follows a similar pattern as the growth of the cracks (shown together in Figure 5.14 c), with a large increase during the first 2000 cycles and a stabilisation between 4000 and 10 000 cycles. The cracks in the CL, together with the delamination to the membrane that was observed, contribute to worse physical contact within the catalyst layer and at the interfaces between the catalyst layer and the membrane. This physical decrease of contact translates to decrease of electrical contact and thus an increase of electric and ionic resistance, as indicated by the similar behaviour of crack growth and resistance increase.

To quantify the loss of carbon and the concurrent shrinkage of the carbon support, the diameter of distinct carbon particles was measured throughout the AST in the IL-SEM and IL-TEM images. Specific carbon particles were

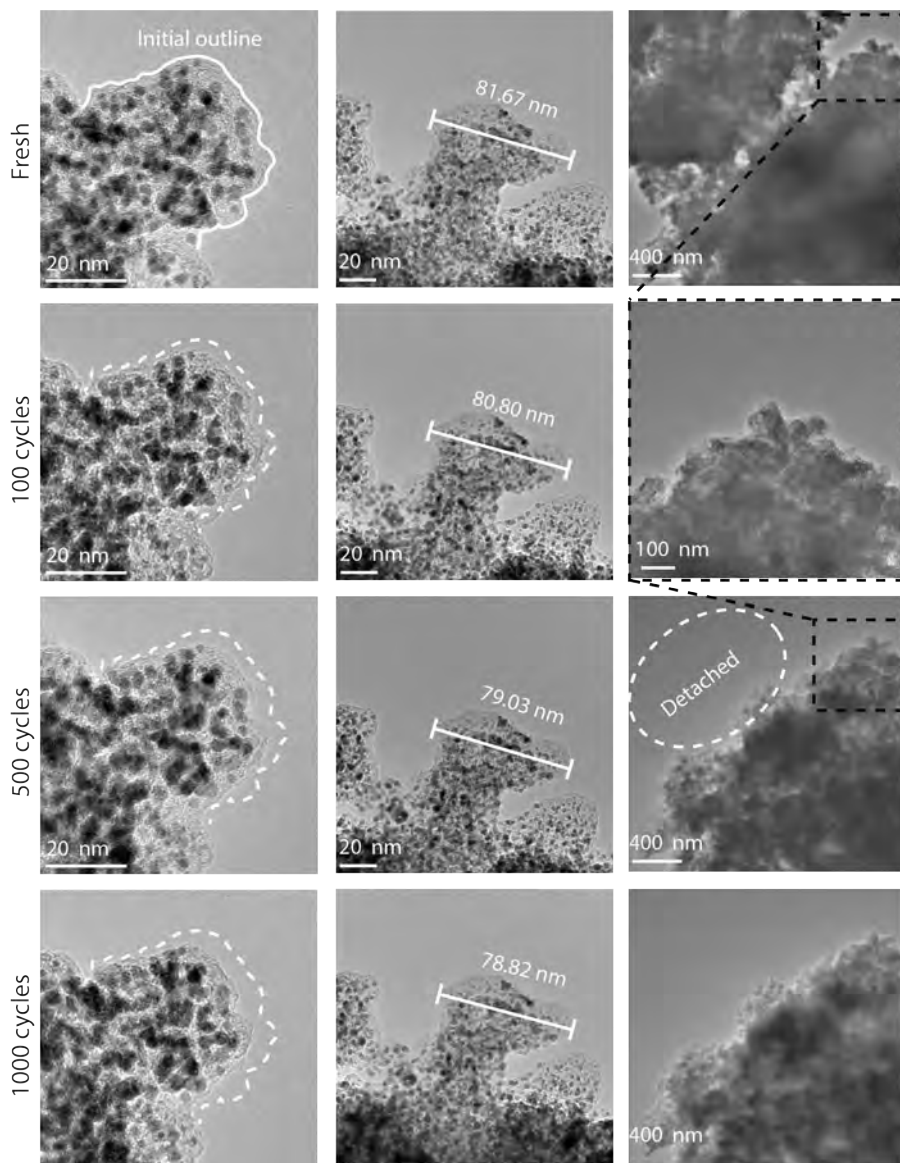


Figure 5.12: IL-TEM imaging of fresh Pt/C and after degradation during SUSD AST cycling for 100, 500, and 1000 cycles. Images from cycles 2000–10 000 can be found in Figure 5.13. Markings and measurements have been added to the images to guide the reader, though they are not comprehensive. Note that the second image in the right column has another magnification than the rest of the column. Markings have been added to indicate from from which area this image is taken in relation to the other images.

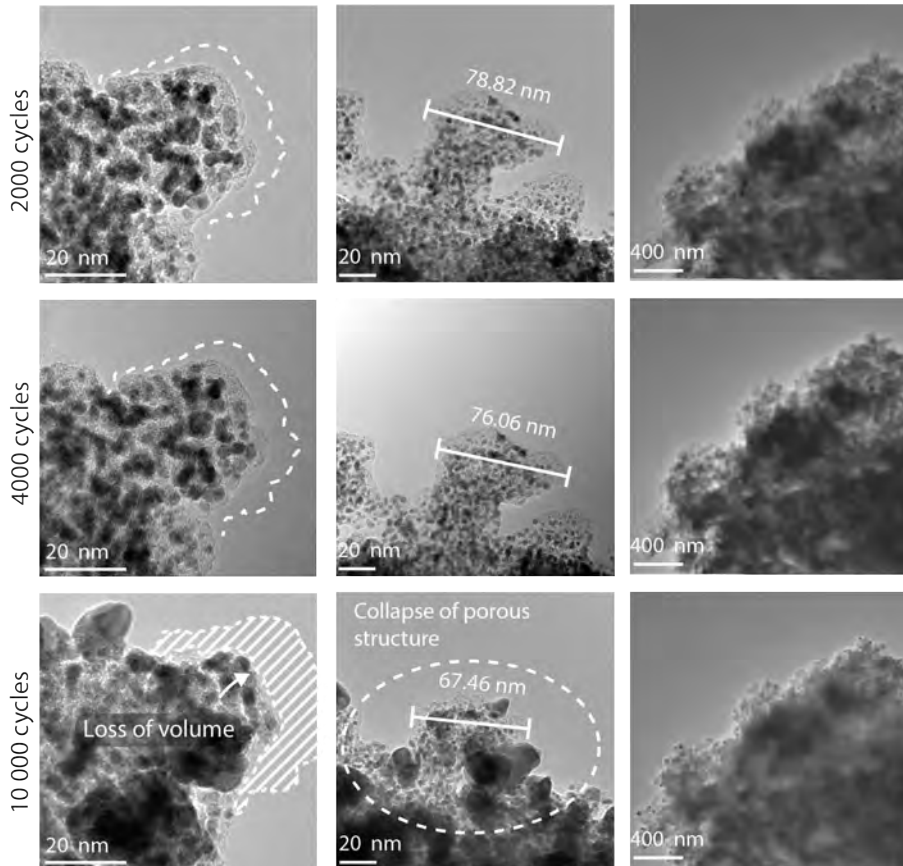


Figure 5.13: IL-TEM imaging Pt/C after degradation during SUSD AST cycling for 2000, 4000, and 10 000 cycles. Images from cycles 0–1000 can be found in Figure 5.12. Markings and measurements have been added to the images to guide the reader, though they are not comprehensive.

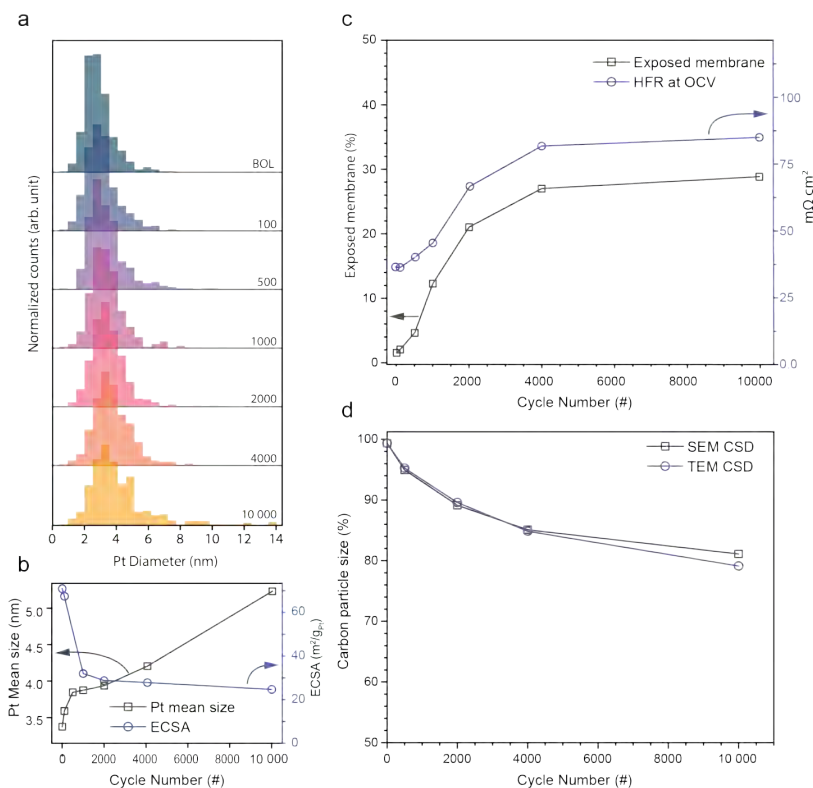


Figure 5.14: a) PSD during SUSD AST. b) average particle diameter (grey) and ECSA loss (blue). c) Percent of CL surface covered by cracks (grey squares) and HFR at OCV (blue circles). d) Decrease of carbon support volume measured from SEM images (grey) and from TEM images (blue).

identified in all images in the image series and their diameter was measured. The average decrease in the size of the carbon particles is shown in Figure 5.14d. First, one can note that the trends seen in SEM and TEM are very similar, which is a good indication that while TEM is a more localised technique, it can still be used to give good data on the catalyst behaviour and that the trends observed on the TEM grids are indicative of the processes happening on a larger scale on the catalyst layer. The carbon size gradually decreases during the first 4000 cycles, with little carbon shrinkage between 4000 and 10 000 cycles.

Overall, IL microscopy shows severe degradation of the CCL microstructure during the SUSD AST cycling, both on the microscale in the form of crack formation and growth, and on the nanoscale in the form of carbon particle shrinkage and Pt particle growth, which is concurrent with an equally severe loss of performance and increased cell resistance. Cracks in the CL, delamination between the CL and the underlying membrane, and loss of internal connection

Sample name	Membrane type	Ionomer	Cathode catalyst loading (mg cm^{-2})	Cathode catalyst type	Initial Pt particle size ^a (nm)
A	PFSA	PFSA	0.4	Pt/C	4.9 ± 1.4
B	PFSA	PFSA	0.35	Pt/C	4.9 ± 1.4
C	PFSA	PFSA	0.4	Pt/C	3.7 ± 1.0
D	PFSA	PFSA	0.4	Pt/C	3.8 ± 1.4

^aMean particle size and standard deviation of 500 particles measured from TEM images.

Table 5.1: Compositions of MEAs used to study degradation during IT-PEMFC operation.

points within the CL likely contribute to the increase in resistance. Furthermore, compaction of the CL and loss of porosity likely contribute to an increase in mass transfer resistance. The growth of Pt particles as a result of support corrosion and the loss of electrical connection to parts of the CL contribute to the loss of ECSA, although the loss of ECSA contributes less to the overall performance loss compared to the increase in resistance and the increase in mass transfer. All of these effects combined severely limit the performance of fuel cells, in particular compared to the degradation and performance loss seen during normal-condition operation.

5.3 Intermediate Temperature Operation

The final project in this thesis examines the degradation of state-of-the-art commercially available MEAs under IT operation, and is presented in **Paper V**. Specifically, four different types of MEA composition were studied during operation at 80, 100, and 120 °C. The compositions of the MEAs used for this study are detailed in Table 5.1. This study was motivated by the industry’s interest in operating PEMFCs in IT conditions for heavy-duty vehicles and aviation applications, together with a lack of data on how current state-of-the-art MEAs perform under these new operating conditions. The MEAs used for this study were provided by PowerCell Group for research purposes. The MEAs are all based on PFSA membranes of varying thicknesses, have cathodic catalyst layers based on Pt/C catalyst and PFSA ionomer, and are produced using different materials and recipes. The MEAs are originally designed and optimised for automotive operating conditions (70–90 °C, 95 °C peak).

Figure S1 (in Supporting Information to **Paper V**) presents the complete sets of polarisation curves measured at BOL, and after 1000, 5000, and 10 000 total AST cycles conducted at either 80, 100, or 120 °C for samples A, B, C and D. The polarisation curves were measured at 80 °C, 100% RH and at 1.5 barg overpressure on both the anode and cathode. The iR-corrected performance at BOL and at EOL after AST cycling at 80, 100, or 120 °C is shown in Figure

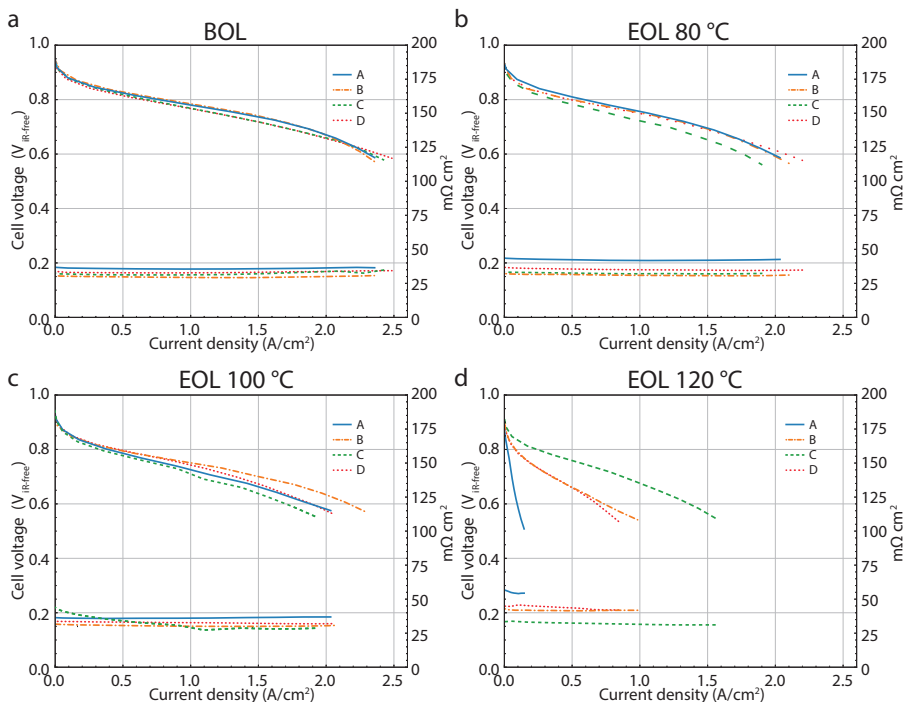


Figure 5.15: iR-corrected polarisation curves and high frequency resistance of MEA A (blue solid lines), B (orange dashed-dotted lines), C (green dashed lines) and D (red dotted lines) from a) fresh MEAs (each curve is an average of three fresh MEAs) b) MEAs subjected to 15 000 AST cycles at 80 °C, c) MEAs subjected to 15 000 AST cycles at 100 °C and d) MEAs subjected to 15 000 AST cycles at 120 °C.

5.15a–d. At BOL, the MEAs have a notably similar performance (Figure 5.15a) which can be divided into two groups. The first group of MEA A and B performs around 10–20 mV better than the second group consisting of MEA C and D between 0.0 and 2.0 A, while C and D perform slightly better at the very highest current densities. The MEAs all reach a maximum current density of around 2.35–2.50 $A cm^{-2}$ and their high-frequency resistance is around 30–40 $m\Omega cm^2$.

After AST cycling at 80 °C (Figure 5.15b), all MEAs have a decrease in performance. MEA A, B and D have similar performance at EOL 80 °C. However, since MEA D performed slightly worse than MEA A and B at BOL, it has the least overall voltage loss. MEA C shows the worst performance at EOL 80 °C, and the largest amount of voltage loss, with a voltage of around 30–40 mV below the EOL performance of MEA A, B and D. The variation in EOL performance between MEAs is more pronounced after AST cycling at 100 °C (Figure 5.15c) compared to 80 °C. At 100 °C, all MEAs show slightly greater degradation than they did at 80 °C. MEA C continues to show the worst EOL

performance, while MEA B shows the best. MEA A and MEA E show similar performance to each other. However, after cycling at 120 °C (Figure 5.15 d), the trends are considerably different. First, it is clear that all MEAs degrade considerably worse at 120 °C than they did at either 100 or 80 °C. However, the difference in degradation between the MEAs is considerably more pronounced. Surprisingly, in opposition to the trends observed at 80 °C and 100 °C, MEA C here outperforms all other MEAs significantly, still reaching around 1.35 A cm⁻² at 0.6 V. This can be compared to the worst performance which is seen in MEA A, that barely reaches 0.1 A cm⁻² at 0.6 V. MEA B and D, while still exhibiting severe degradation, does better than MEA A, and both reaches around 0.7 A cm⁻² at 0.6 V. Furthermore, MEA A, B, and D show increased resistance after AST cycling at 120 °C, reaching approximately 55 mΩ cm² for A and 40–45 mΩ cm² for B and D, a change not observed in MEA C. It is clear that an increase in operation temperature has a strong effect on MEA performance and degradation behaviour.

The effect of temperature on the ECSA was investigated using CVs. Figure 5.16 a–d show the ECSA losses (absolute and percentage) of MEA A, B, C and D, measured at BOL and after 1000, 5000, and 15 000 AST cycles at 80, 100, or 120 °C. The full set of CVs used to calculate the ECSA can be found in supporting information of **Paper V** (Figure S2). Two types of ECSA decay pattern can be identified, and once again, the behaviour can be divided into two groups, with MEA A and B in the first group and MEA C and D in the second. MEA A and B have initial ECSA of around 40–50 m² g_{Pt}⁻¹, with a ECSA loss pattern that is roughly linear with the number of cycles. MEA C and D, on the other hand, have a much larger initial ECSA of 65–78 m² g_{Pt}⁻¹, with a decay pattern with rapid initial decrease and a gradual stagnation, much more similar to the decay pattern seen in Figure 5.3 and Figure 5.14b. For both groups, these ECSA losses increase with temperature, and they maintain their overall pattern, that is, a linear loss for MEA A and B and a rapid initial loss with a gradual stagnation for MEA C and D. At 80 °C, MEA C and D show higher ECSA losses than MEA A and B, of around 35–50% ECSA losses for MEA C and D compared to 20–25% ECSA losses for MEA A and B. However, at 120 °C this trend shift and MEA A and B exhibit more ECSA losses than MEA C and D, with more than 90% ECSA losses for MEA A and B and around 80% ECSA losses for MEA C and D.

The increase in ECSA losses was assumed to correlate with a larger growth of Pt particles. This was confirmed by imaging catalyst powders from fresh samples, and samples that had undergone 15 000 AST cycles at either 80 °C, 100 °C, or 120 °C with TEM, see Figure 5.17 for representative TEM images. For each sample, the diameter of more than 500 Pt particles was measured to form histograms (see Figure S3 in Supporting Information of **Paper V**) and to measure the average Pt diameter (see Figure 5.18). Much like the ECSA, two groups of Pt growth can be identified. MEA A and B have a larger initial Pt size, with an average Pt diameter of around 4.9 nm, corresponding to the smaller initial ECSA. In comparison, MEA C and D, have a smaller initial Pt size, of around 3.7–3.8 nm on average, corresponding to the larger initial

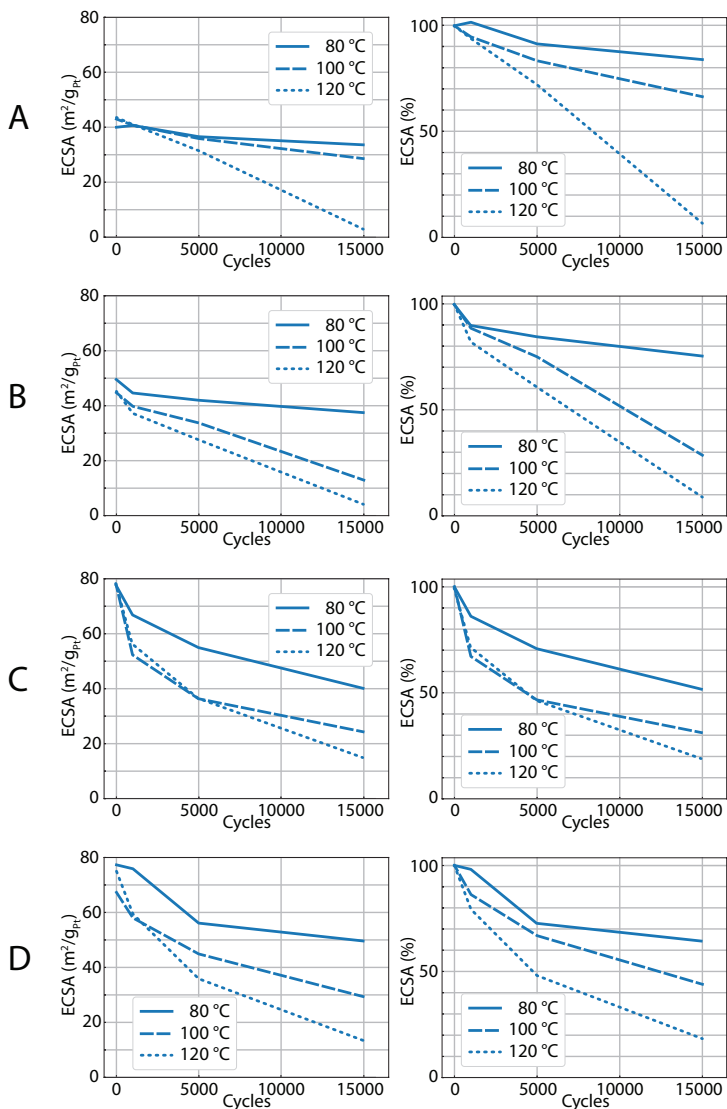


Figure 5.16: Absolute and relative ECSA measured at BOL and after 1000, 5000, and 15 000 AST cycles at 80 °C, 100 °C, or 120 °C from MEA A, B, C and D.

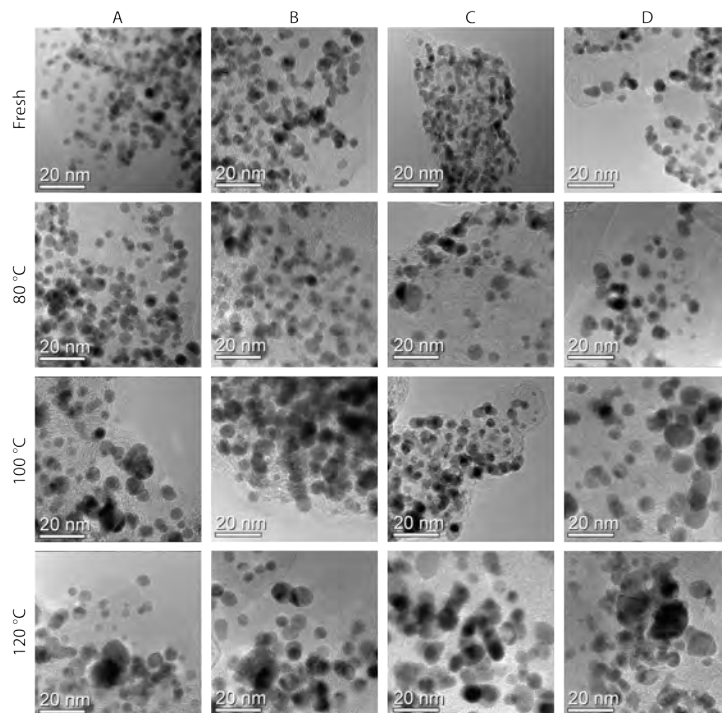


Figure 5.17: Representative TEM images of powders from the cathode catalyst layers of MEA A, B, C, and D from fresh MEAs, and MEAs that had undergone AST cycling at 80 °C, 100 °C, or 120 °C.

ECSA. At 80 °C, MEA A and B show little Pt growth, of only 4–5% to around 5.1 nm. MEA C and D show a larger growth of around 18–23%, to around 4.5 and 4.7 nm, respectively. However, while the relative growth of MEA A and B is smaller, they are still larger after AST cycling at 80 °C compared to MEA C and D, as they have a larger initial size. Likely, the increased stability of MEA A and B comes from the initial larger Pt particle size, as larger particles are known to be more stable [162].

At 100 °C, the average Pt diameter of all samples grows substantially more than at 80 °C. Additionally, the size difference between the initial larger samples (A and B) and the initial smaller samples (C and D) diminishes, resulting in more similar size distribution, with mean diameters ranging from 6.2 to 6.7 nm. However, A and B still show less relative growth of 27% and 36% respectively, while C and D grow by 70% and 71% respectively. At 120 °C, the samples grow slightly more than at 100 °C, with average diameters ranging from 6.3 to 7 nm. However, increasing the temperature from 100 to 120 °C has a much smaller impact on growth rate compared to increasing from 80 to 100 °C. Furthermore, at 120 °C, there is no clear correlation between the initial and final particle sizes, although A and B continue to show less relative growth due to their initially larger sizes. The accelerated growth of Pt particles at

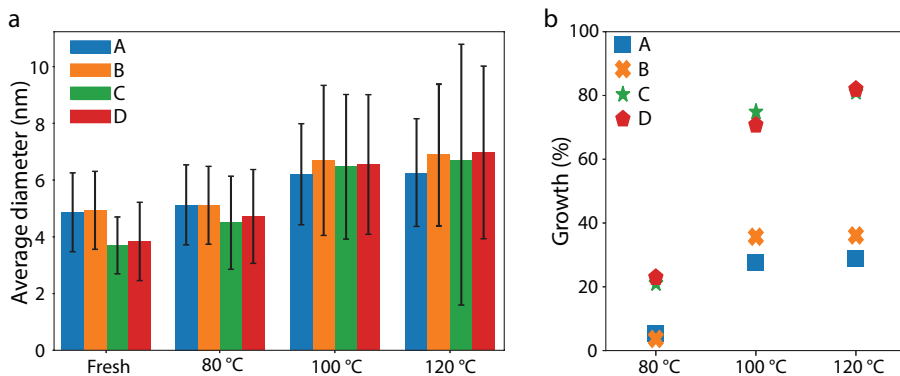


Figure 5.18: a) Average diameter and b) relative growth of Pt particles for MEA A (blue), B (orange), C (green), and D (red), calculated by measuring over 500 Pt particles from TEM images for each sample.

100 and 120 °C, compared to 80 °C, is likely due to increased ion mobility at higher temperatures. The increased Pt growth contributes to the increased rates of ECSA losses observed for all samples at higher temperatures. Increased ion mobility may also promote deposition of Pt in the membrane, forming Pt bands, as is well reported to occur at operation at lower operation temperatures (≤ 80 °C) [239–241], further contributing to increased ECSA losses and increase ionic resistance through the membrane.

Comparing voltage losses with the decrease in ECSA, see Figure 5.19, shows that the majority of the performance loss at 80 °C and 100 °C can be explained by ECSA losses, i.e., the voltage loss roughly follows a trend of loss of -70 mV dec $^{-1}$ ECSA. Hence, also the differences in performance loss can to a large extent be explained by the different behaviour in ECSA. However, this is not true at 120 °C. Only sample C follows a -70 mV dec $^{-1}$ loss at 120 °C, while MEA A, B and D deviates strongly, especially at higher current densities. Although samples A, B, and D exhibited resistance increases at 120 °C, this is still not enough to explain the large performance decrease. In particular, the deviation from the expected voltage decrease is greater at higher current densities, that is, where mass transport limitations are more prevalent.

It is interesting to note that the MEA that experienced the greatest degradation at 80 °C (MEA C) outperformed the other MEAs at 120 °C, while the MEAs that were best at 80 °C performed significantly worse at 120 °C. This underlines the importance of adapting MEAs to specific working conditions. Catalysts that exhibit good corrosion resistance at 80 °C do not necessarily maintain this resistance at 100 or 120 °C. When designing an MEA for a wide temperature range, a balance between performance and stability is critical, which means that performance and durability at 80 °C may have to be sacrificed to ensure stability at higher temperatures.

As a side note, although the original plan included IL microscopy as part of

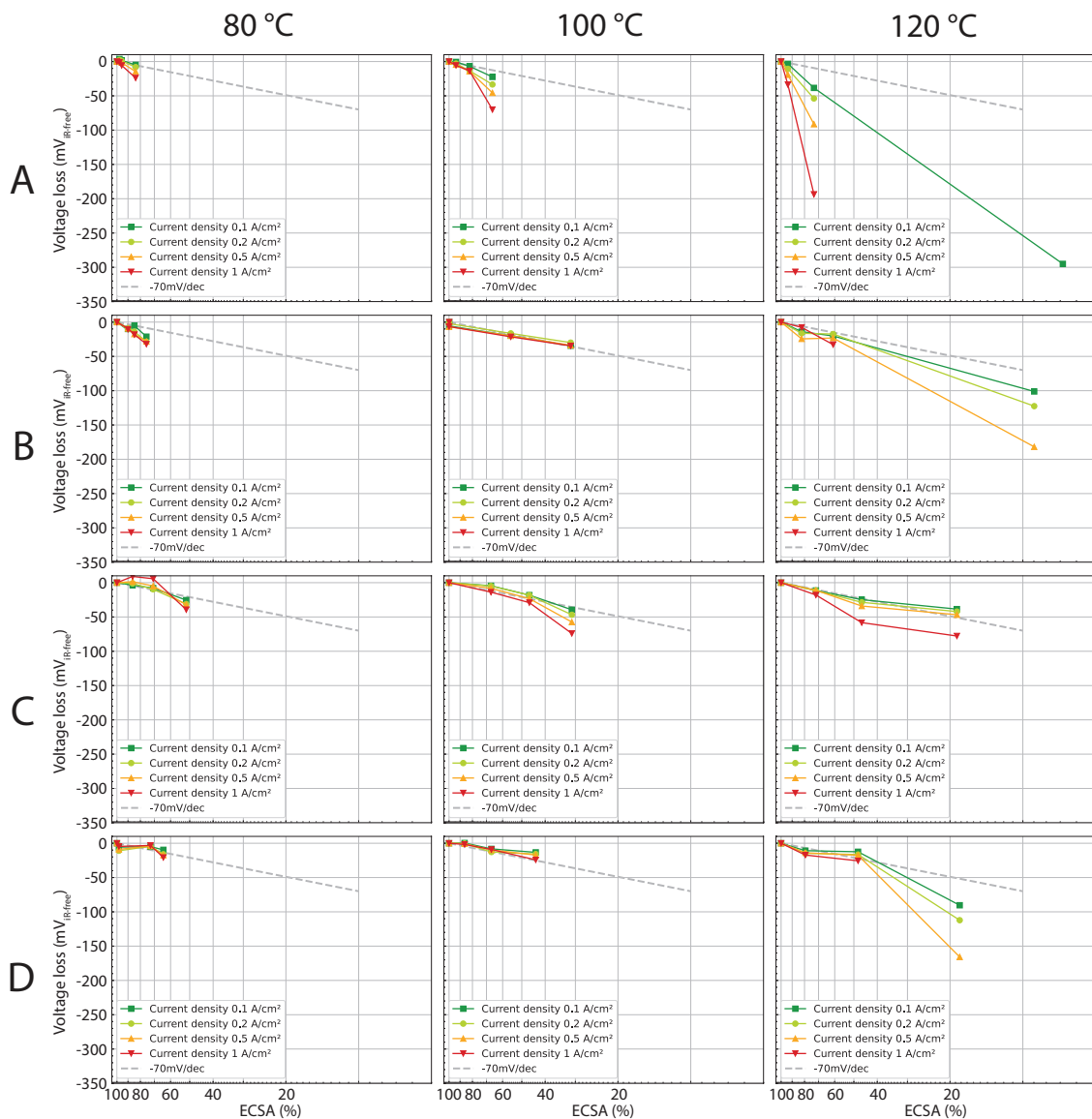


Figure 5.19: Voltage loss vs. ECSA at different current densities for sample A, B, C and D during AST cycling at 80 °C, 100 °C or 120 °C.

this study, technical issues with the microscopes and prolonged repair times led to the abandonment of this aspect of the investigation, and only MEA A was fully investigated using the IL-SEM technique. However, preliminary IL-SEM imaging of MEA A at various temperatures revealed intriguing effects on large-scale surface structures. Figure 5.20 shows representative IL-SEM images of MEA A. At 80 °C, the large-scale structure was found to be stable, similar to what was observed in our previous study carried out under similar conditions; see Figure 5.4. However, at 100 °C, cracks are seen to form in the cathode CL surface. What is notable is that these cracks form at two distinct size scales and behave differently. Some larger cracks, circa 100 μm long and 5–10 μm wide, have formed between 5000 and 15 000 AST cycles, although at this size scale the surface is still mostly intact. On the 10 μm scale, cracks are formed as well. However, on this scale, cracks are noticeable already after 5000 cycles, and more unexpectedly, the cracks seem to close up and reduce in size between 5000 and 15 000 cycles. This behaviour was observed at several locations. Why this self-healing takes place is unclear, but a continuation of the IL-SEM study including, e.g., more frequent imaging of the sample may confirm if this is commonly present, and if so how and when this process takes place. During AST cycling at 120 °C, cracks can similarly be observed to form at two distinct size scales, roughly 100 μm and 10 μm long, respectively. However, larger cracks (around 100 μm long) are noticeably present already after 5000 cycles, and they grow noticeably wider at 15 000 cycles, to around 20 μm . Smaller cracks (around 10 μm) are also noticeable after 5000 cycles, but no self-healing or closing of these cracks were observed at 120 °C, and they continue to grow in size until 15 000 cycles.

Although the other MEAs were not imaged with IL-SEM due to issues with the instrumentation during the testing, they were imaged with SEM post-mortem, see Figure S4 in Supporting Information of **Paper V**. In addition to MEA A, the other MEAs showed no signs of crack formation or other morphological changes to the cathode CL. This could be an indication that MEA A has issues with structural stability, due to e.g., ink formulation. Ink formulation is known to have an impact on catalyst microstructure, cell performance, stability and crack formation at normal operation temperatures (<80 °C) [173, 303], and it is possible that ink recipes that prove sufficient at 80 °C can result in crack formation at intermediate temperature operation, as MEA A did. Although crack formation at 100 °C for MEA A did not translate to a considerable performance loss, it indicates structural instabilities of the CL. Poor microstructural stability at 120 °C could explain part of the severe performance degradation observed for MEA A at this temperature, e.g., by promoting water accumulation and exacerbating issues of mass transport limitations.

Hydrogen crossover was ruled out as a significant contributor to the increase in performance loss at elevated temperatures, as it showed no correlation with the increase in temperature or the number of cycles, see Figure S5 in Supporting Information of **Paper V**. Changes in the double layer suggest that carbon area is lost during the degradation, and that this decrease of carbon area scales with temperature, see Figure S6 in Supporting Information of **Paper**

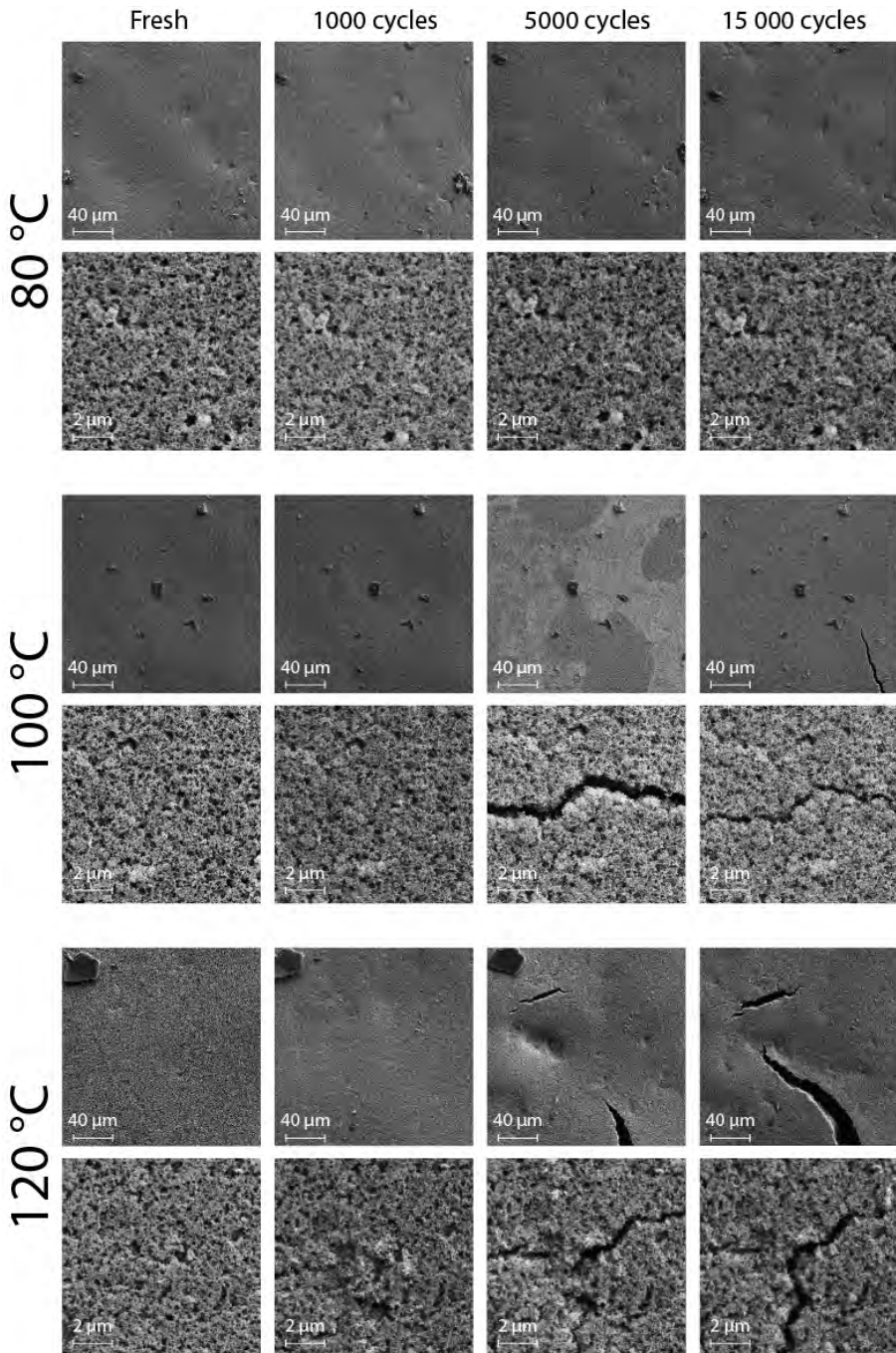


Figure 5.20: IL-SEM images of MEA A at BOL and after 1000, 5000, and 15 000 AST cycles at 80, 100, and 120 °C.

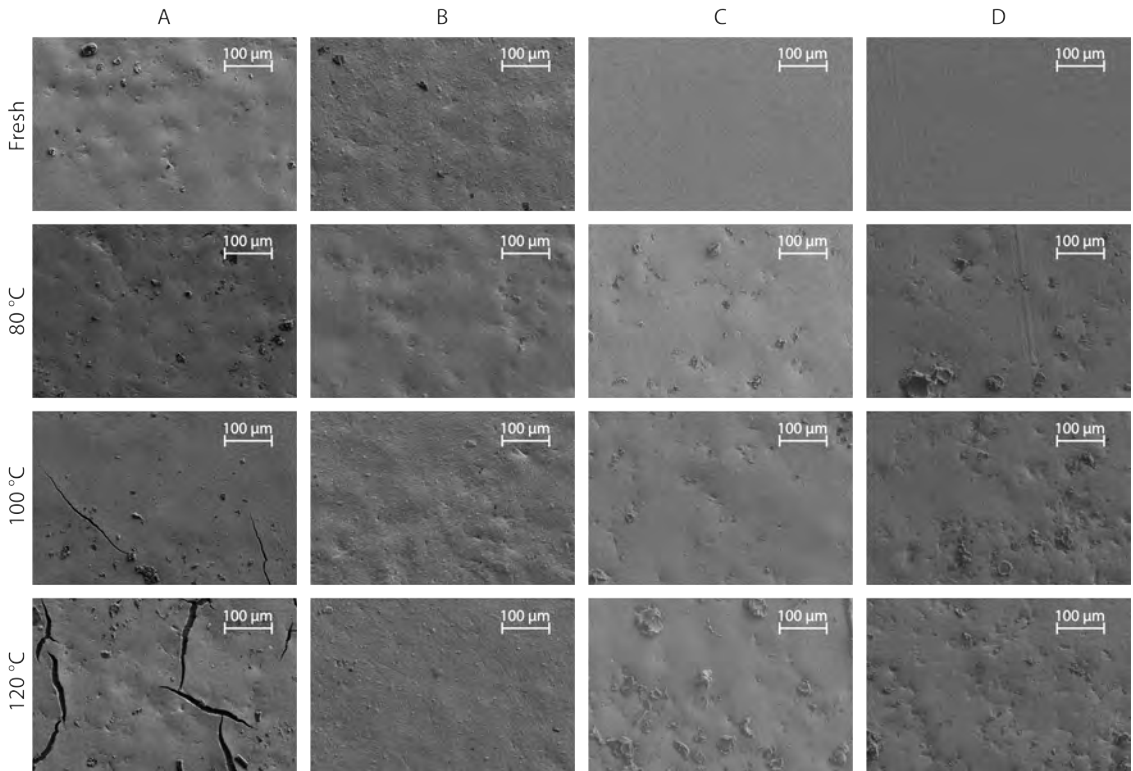


Figure 5.21: SEM images of the cathode catalyst layer of fresh MEAs and MEAs that have undergone 15 000 AST cycles between 0.6 and 0.95 V at 80, 100, or 120 °C for MEA A, B, C, and D.

V, which could suggest either that carbon has been lost via carbon oxidation or that the porous structure of the carbon support has collapsed. However, the general behaviour is similar for all samples and no clear correlation is seen between the capacitance decrease and the performance difference between the samples.

In summary, the intermediate temperature operation was shown to increase the degradation rates of performance for all MEAs tested. At 80 and 100 °C, this performance decrease can be explained by ECSA losses, which increase at elevated temperatures due to increased Pt particle growth, likely due to increased ion mobility. However, at 120 °C MEA A, B and D showed much more performance loss than can be explained by only ECSA losses or resistance increase, indicating problems with mass transport limitations. Furthermore, MEA C, which performed the worst at 80 and 100 °C, significantly outperformed the other MEAs at 120 °C

Although discussions of intermediate temperature operation often focus on the performance of the PFSA membrane and ionomer, the results here show that the catalyst layer plays a key role in endurance at these temperatures. This must be taken into account when designing fuel cells for intermediate temperature operation. Catalysts with strong corrosion resistance at 80 °C may have inadequate stability at higher temperatures compared to those that performed worse at 80 °C, highlighting the need for catalyst layers specifically designed for intermediate temperature conditions.

Chapter 6

Conclusions & Outlook

Fuel cells, and in particular proton exchange membrane fuel cells (PEMFCs), are expected to be important for the decarbonisation of the energy and transport sectors. However, PEMFCs suffer from issues related to degradation. To design more durable materials and better mitigation strategies, the degradation mechanisms of the different PEMFC components must be better understood.

By combining identical location (IL) scanning electron microscopy and IL-transmission electron microscopy (TEM) imaging with single cell fuel cell measurements, we have managed to follow the degradation of the cathodic catalytic layer (CL) of a PEMFC under real operation conditions. We have demonstrated that it is possible to open the fuel cell, disassemble the membrane electrode assembly, and image the CL in vacuum, without harming the fuel cell performance or changing the electrochemical characteristics. So far, we have used these methods to study CL degradation during two different types of accelerated stress tests (ASTs). One focussing on degradation during normal operation conditions and one mimicking degradation during start-up/shutdown events. We showed that the CL degrades by different mechanisms during respective AST. In particular, we showed that during start-up/shutdown conditions, the carbon support loses volume, which brings Pt particles closer to each other, which in turn promotes Pt agglomeration, coalescence, and particle growth, and that cracks are formed in the cathodic catalyst layer. These effects correlate to behaviours observed via electrochemical characterisation. Overall, these results demonstrate the possibility of performing IL electron microscopy under realistic fuel cell conditions, and the strength of combining macro- and nanoscale imaging with electrochemical analysis. However, the methods are not perfect and there is room for improvement. One issue is the fact that we observe only the top of the catalyst layer farthest from the membrane, and the degradation is known to differ throughout the cross section of the CL. Optimally, similar measurements would be performed while looking at the degradation at different depths in the CL. However, because of the way the

membrane electrode assembly (MEA) is constructed, it is difficult to image the CL closer to the membrane without permanently damaging the sample, which would make the repeated tests necessary for IL imaging troublesome. Furthermore, the introduction of TEM grids into the MEA does change the local environment by introducing different materials in the form of the gold TEM grid and can change the local transportation of gases. This could affect the results and should be kept in mind. However, the same could certainly be said for IL imaging done in a liquid electrolyte, and the results presented here should give an indication of how degradation in PEMFC environments transpires compared to previous liquid half-cell testing. The effects of TEM grids on the local environment, and how that potentially affects the degradation of the sample, should be investigated further to gain an even better understanding of the true degradation processes transpiring inside the PEMFC CL.

Furthermore, we have studied the behaviour of Pt thin films in acidic and alkaline environments using electrochemical quartz crystal microbalance. The Pt thin films gain more mass during oxidation in alkaline environments than in acidic environments, and the point of minimum mass is located at a higher potential in the alkaline electrolyte, which coincides with the differences in CVs in either electrolyte. Furthermore, Pt starts to dissolve noticeably when the potential is cycled to above 1.1 V in both 0.5 M H₂SO₄ and 1 M KOH, and the dissolution rates are similar in either electrolyte despite the difference in oxide formation.

Our studies of degradation at intermediate temperature show that the degradation of the catalyst layer is highly dependent on operation temperature. In particular, catalysts that are optimised for good performance and stability at 80 °C do not necessarily exhibit good corrosion resistance at elevated temperatures, and may even perform significantly worse than catalysts they outperformed at lower temperatures. Thus, the whole MEA might need to be redesigned if operation at elevated temperatures is desired, and care should be taken when choosing how to trade off between performance and durability.

For future work, it would be interesting if we could continue to develop the IL techniques presented in this thesis, to delve further into the degradation mechanisms in real fuel cell conditions, and possibly investigate how such behaviour differs between real fuel cell set-ups and model systems. In particular, it would be of interest to use IL-microscopy to study degradation behaviour of PEMFCs under higher temperatures in more detail, as my initial result indicate, there are differences in how the microscale structure changes over time. Ultimately, it would be interesting to use these methods to study the degradation of more novel catalyst materials in real PEMFC conditions to see how their stability compares to that of the industry standard Pt.

Acknowledgment

This work is financially supported by the the Sweden Foundation for Strategic Research (Stiftelsen för strategisk forskning, SSF).

First, I would like to thank my supervisor Björn Wickman, for giving me the opportunity to pursue this PhD, and supporting me throughout it. My thanks also go to my examiner Henrik Grönbeck.

I am grateful to the members of KF and the electrochemistry group for their continuous support, advice, and for fostering an encouraging and collaborative working environment. In particular, I would like to extend my gratitude to all past and present office mates for the motivating and energizing conversations we shared. Your camaraderie and insights have been invaluable, bringing encouragement and positivity to my days. Thank you for making the workspace such a supportive and inspiring environment. A special thanks goes to Victor Shokhen, for teaching me much of what I know of fuel cells and electron microscopy, and not least at all for helping me make some beautiful illustrations for this thesis.

My heartfelt thanks go to my friends, fellow musicians, dancers, scout leaders, and acquaintances, who have been a source of balance and joy. Thank you for being a constant reminder of the world beyond my work.

Last but not least, I would like to thank my family, for being there for me at all times, in good times and bad. Especially to my brothers, for inspiring and motivating me to be a better me, and whom without I would not have tried pursuing a PhD in the first place.

Each of you has played a part in bringing me to where I am today, Thank you all, truly.

Bibliography

- [1] M. Kappelle *et al.*, *WMO Statement on the State of the Global Climate in 2019*, 2020.
- [2] UNFCCC, “Paris agreement,” in *Report of the Conference of the Parties to the United Nations Framework Convention on Climate Change (21st Session, 2015: Paris)*, vol. 4, 2015, p. 2017.
- [3] NOAA National Centers for Environmental information. “Climate at a glance: Global time series.” (2022), [Online]. Available: <https://www.ncdc.noaa.gov/cag/> (visited on 20/10/2022).
- [4] P. Friedlingstein *et al.*, “Global carbon budget 2021,” *Earth System Science Data*, vol. 14, no. 4, pp. 1917–2005, 2022.
- [5] United Nations, “Transforming our world: The 2030 agenda for sustainable development,” *New York: United Nations, Department of Economic and Social Affairs*, 2015.
- [6] Government Offices of Sweden, Ministry of the Environment and Energy, “Sweden’s draft integrated national energy and climate plan: According to regulation (eu) 2018/1999 of the european parliament and of the council on the governance of the energy union and climate action,” Government Offices of Sweden, 2017, [Accessed 17-01-2025]. [Online]. Available: [www.government.se/contentassets/e731726022cd4e0b8ffa0f8229893115/swedens-draft-integrated-national-energy-and-climate-plan/#:~:text=By%202030%2C%20Sweden's%20energy%20use,gross%20domestic%20product%20\(GDP\).&text=The%20target%20by%202040%20is%20100%20per%20cent%20renewable%20electricity%20production..](http://www.government.se/contentassets/e731726022cd4e0b8ffa0f8229893115/swedens-draft-integrated-national-energy-and-climate-plan/#:~:text=By%202030%2C%20Sweden's%20energy%20use,gross%20domestic%20product%20(GDP).&text=The%20target%20by%202040%20is%20100%20per%20cent%20renewable%20electricity%20production..)
- [7] C. Fetting, “The european green deal,” *ESDN Report, December*, vol. 2, no. 9, 2020.
- [8] Energimyndigheten. “Sverige har överträffat målet om andel förnybar energi för 2020.” (2022), [Online]. Available: <https://www.energimyndigheten.se/nyhetsarkiv/2022/sverige-har-overtraffat-malet-om-andel-fornybar-energi-for-2020/> (visited on 05/10/2022).

- [9] Statistikmyndigheten SCB. “Elproduktion och förbrukning i Sverige.” (2022), [Online]. Available: <https://www.scb.se/hitta-statistik/sverige-i-siffror/miljo/elektricitet-i-sverige/> (visited on 05/10/2022).
- [10] Energiföretagen Sverige. “Elproduktion.” (2018), [Online]. Available: <https://www.energiforetagen.se/energifakta/elsystemet/produktion/#:~:text=Den%20el%20som%20produceras%20i,kraftslagen%20som%20sol%20och%20vind.> (visited on 05/10/2022).
- [11] H. Ritchie, *Cars, planes, trains: Where do co emissions from transport come from?* [Accessed 12-01-2025], 2020. [Online]. Available: <https://ourworldindata.org/co2-emissions-from-transport>.
- [12] X. Zeng *et al.*, “Commercialization of lithium battery technologies for electric vehicles,” *Advanced Energy Materials*, vol. 9, no. 27, p. 1900161, 2019.
- [13] K. Forrest, M. Mac Kinnon, B. Tarroja and S. Samuelsen, “Estimating the technical feasibility of fuel cell and battery electric vehicles for the medium and heavy duty sectors in california,” *Applied Energy*, vol. 276, p. 115439, 2020.
- [14] N. Gray, S. McDonagh, R. O’Shea, B. Smyth and J. D. Murphy, “Decarbonising ships, planes and trucks: An analysis of suitable low-carbon fuels for the maritime, aviation and haulage sectors,” *Advances in Applied Energy*, vol. 1, p. 100008, 2021.
- [15] G. Guandalini and S. Campanari, “Well-to-wheel driving cycle simulations for freight transportation: Battery and hydrogen fuel cell electric vehicles,” in *2018 International Conference of Electrical and Electronic Technologies for Automotive*, IEEE, 2018, pp. 1–6.
- [16] D. A. Cullen *et al.*, “New roads and challenges for fuel cells in heavy-duty transportation,” *Nature energy*, vol. 6, no. 5, pp. 462–474, 2021.
- [17] Office of Fossil Energy, United States Department of Energy. “Hydrogen Strategy, Enabling a Low-Carbon Economy.” (2020), [Online]. Available: https://www.energy.gov/sites/prod/files/2020/07/f76/USDOE_FE_Hydrogen_Strategy_July2020.pdf (visited on 03/11/2022).
- [18] D. R. Palo, R. A. Dagle and J. D. Holladay, “Methanol steam reforming for hydrogen production,” *Chemical reviews*, vol. 107, no. 10, pp. 3992–4021, 2007.
- [19] F. S. AlHumaidan, M. A. Halabi, M. S. Rana and M. Vinoba, “Blue hydrogen: Current status and future technologies,” *Energy Conversion and Management*, vol. 283, p. 116840, 2023.
- [20] A. M. Oliveira, R. R. Beswick and Y. Yan, “A green hydrogen economy for a renewable energy society,” *Current Opinion in Chemical Engineering*, vol. 33, p. 100701, 2021.
- [21] M. R. Usman, “Hydrogen storage methods: Review and current status,” *Renewable and Sustainable Energy Reviews*, vol. 167, p. 112743, 2022.

- [22] R. Guo, Q. Li and N. Zhao, “An overview of grid-connected fuel cell system for grid support,” *Energy Reports*, vol. 8, pp. 884–892, 2022.
- [23] Z. Abdin, A. Zafaranloo, A. Rafiee, W. Mérida, W. Lipiński and K. R. Khalilpour, “Hydrogen as an energy vector,” *Renewable and sustainable energy reviews*, vol. 120, p. 109620, 2020.
- [24] T. K. Mandal and D. H. Gregory, “Hydrogen: A future energy vector for sustainable development,” *Proceedings of the institution of mechanical engineers, part C: journal of mechanical engineering science*, vol. 224, no. 3, pp. 539–558, 2010.
- [25] Í. Martín-García, E. Rosales-Asensio, A. González-Martínez, S. Bracco, F. Delfino and M. de Simón-Martín, “Hydrogen as an energy vector to optimize the energy exploitation of a self-consumption solar photovoltaic facility in a dwelling house,” *Energy Reports*, vol. 6, pp. 155–166, 2020.
- [26] 2021. [Online]. Available: <https://fuelcellworks.com/news/south-korea-worlds-largest-hydrogen-fuel-cell-power-plant-opened-by-korean-southern-power-kospo/>.
- [27] Wikipedia. “Energy density.” (2022), [Online]. Available: https://en.wikipedia.org/wiki/Energy_density (visited on 20/10/2022).
- [28] P. Preuster, A. Alekseev and P. Wasserscheid, “Hydrogen storage technologies for future energy systems,” *Annual review of chemical and biomolecular engineering*, vol. 8, pp. 445–471, 2017.
- [29] P. T. Aakko-Saksa, C. Cook, J. Kiviaho and T. Repo, “Liquid organic hydrogen carriers for transportation and storing of renewable energy—review and discussion,” *Journal of Power Sources*, vol. 396, pp. 803–823, 2018.
- [30] N. Rusman and M Dahari, “A review on the current progress of metal hydrides material for solid-state hydrogen storage applications,” *International Journal of Hydrogen Energy*, vol. 41, no. 28, pp. 12108–12126, 2016.
- [31] K. T. Møller, T. R. Jensen, E. Akiba and H.-w. Li, “Hydrogen—a sustainable energy carrier,” *Progress in Natural Science: Materials International*, vol. 27, no. 1, pp. 34–40, 2017.
- [32] D. Papageorgopoulos, “Fuel Cell RD Overview 2019 Annual Merit Review and Peer Evaluation Meeting,” U.S. Department of Energy, Salt Lake City, UT, Tech. Rep., 2019. [Online]. Available: https://www.hydrogen.energy.gov/pdfs/review19/plenary_fuel_cell_papageorgopoulos_2019.pdf.
- [33] A. Wilson, G. Kleen and D. Papageorgopoulos, *Fuel Cell System Cost - 2017*. Department of Energy, 2017.
- [34] United States Department of Energy, “Fuel Cell Technical Team Roadmap,” Jun. 2013. DOI: 10.2172/1220127. [Online]. Available: <https://www.osti.gov/biblio/1220127>.

- [35] U.S. DRIVE, “Fuel Cell Technical Team Roadmap,” Nov. 2017. DOI: 10.2172/1220127. [Online]. Available: <https://www.energy.gov/eere/vehicles/articles/us-drive-fuel-cell-technical-team-roadmap>.
- [36] B. G. Pollet, S. S. Kocha and I. Staffell, “Current status of automotive fuel cells for sustainable transport,” *Current opinion in Electrochemistry*, vol. 16, pp. 90–95, 2019.
- [37] M. Omrani, M. Goriaux, Y. Liu, S. Martinet, L. Jean-Soro and V. Ruban, “Platinum group elements study in automobile catalysts and exhaust gas samples,” *Environmental Pollution*, vol. 257, p. 113 477, 2020.
- [38] Clean Hydrogen Joint Undertaking, “Clean Hydrogen joint undertaking (Clean Hydrogen JU) work programme 2022,” 2022.
- [39] A. J. Verhage, J. F. Coolegem, M. J. Mulder, M. H. Yildirim and F. A. de Bruijn, “30,000 h operation of a 70 kW stationary PEM fuel cell system using hydrogen from a chlorine factory,” *International Journal of Hydrogen Energy*, vol. 38, no. 11, pp. 4714–4724, 2013.
- [40] Y. Qiao and C. M. Li, “Nanostructured catalysts in fuel cells,” *Journal of Materials Chemistry*, vol. 21, no. 12, pp. 4027–4036, 2011.
- [41] V. R. Stamenkovic *et al.*, “Improved oxygen reduction activity on Pt₃Ni (111) via increased surface site availability,” *science*, vol. 315, no. 5811, pp. 493–497, 2007.
- [42] F. Zhou, Y. Yan, S. Guan, W. Guo, M. Sun and M. Pan, “Solving Nafion poisoning of ORR catalysts with an accessible layer: designing a nanostructured core-shell Pt/C catalyst via a one-step self-assembly for PEMFC,” *International Journal of Energy Research*, vol. 44, no. 13, pp. 10 155–10 167, 2020.
- [43] K. Wang *et al.*, “Iron oxide@ graphitic carbon core-shell nanoparticles embedded in ordered mesoporous N-doped carbon matrix as an efficient cathode catalyst for PEMFC,” *Applied Catalysis B: Environmental*, vol. 264, p. 118 468, 2020.
- [44] C. Chen *et al.*, “Highly crystalline multimetallic nanoframes with three-dimensional electrocatalytic surfaces,” *Science*, vol. 343, no. 6177, pp. 1339–1343, 2014.
- [45] F. Xiao *et al.*, “Recent advances in electrocatalysts for proton exchange membrane fuel cells and alkaline membrane fuel cells,” *Advanced Materials*, vol. 33, no. 50, p. 2 006 292, 2021.
- [46] J. K. Nørskov *et al.*, “Origin of the overpotential for oxygen reduction at a fuel-cell cathode,” *The Journal of Physical Chemistry B*, vol. 108, no. 46, pp. 17 886–17 892, 2004.
- [47] I. E. Stephens, A. S. Bondarenko, L. Bech and I. Chorkendorff, “Oxygen electroreduction activity and x-ray photoelectron spectroscopy of platinum and early transition metal alloys,” *ChemCatChem*, vol. 4, no. 3, pp. 341–349, 2012.

- [48] M. Escudero-Escribano *et al.*, “Tuning the activity of Pt alloy electrocatalysts by means of the lanthanide contraction,” *Science*, vol. 352, no. 6281, pp. 73–76, 2016.
- [49] M. Escudero-Escribano *et al.*, “Pt₅Gd as a highly active and stable catalyst for oxygen electroreduction,” *Journal of the American Chemical Society*, vol. 134, no. 40, pp. 16 476–16 479, 2012.
- [50] J Greeley *et al.*, “Alloys of platinum and early transition metals as oxygen reduction electrocatalysts,” *Nature chemistry*, vol. 1, no. 7, pp. 552–556, 2009.
- [51] P. Yu, M. Pemberton and P. Plasse, “PtCo/C cathode catalyst for improved durability in PEMFCs,” *Journal of Power Sources*, vol. 144, no. 1, pp. 11–20, 2005.
- [52] M. Gummalla *et al.*, “Effect of particle size and operating conditions on Pt₃Co PEMFC cathode catalyst durability,” *Catalysts*, vol. 5, no. 2, pp. 926–948, 2015.
- [53] Y. Xing, L. Liu, Z. Li, Y. Li, Z. Fu and H. Li, “Performance of an ePTFE-reinforced membrane electrode assembly for proton-exchange membrane fuel cells,” *Energy & Fuels*, vol. 36, no. 18, pp. 11 177–11 185, 2022.
- [54] Z. Rui and J. Liu, “Understanding of free radical scavengers used in highly durable proton exchange membranes,” *Progress in Natural Science: Materials International*, vol. 30, no. 6, pp. 732–742, 2020.
- [55] M. S. K. Chowdury, Y. Park, S. B. Park and Y.-i. Park, “Degradation mechanisms, long-term durability challenges, and mitigation methods for proton exchange membranes and membrane electrode assemblies with pt/c electrocatalysts in low-temperature and high-temperature fuel cells: A comprehensive review,” *Journal of Electroanalytical Chemistry*, p. 118 712, 2024.
- [56] C. Sheng *et al.*, “Energy management strategy based on health state for a pemfc/lithium-ion batteries hybrid power system,” *Energy Conversion and Management*, vol. 271, p. 116 330, 2022.
- [57] Z. Liu, H. Chen and T. Zhang, “Review on system mitigation strategies for start-stop degradation of automotive proton exchange membrane fuel cell,” *Applied Energy*, vol. 327, p. 120 058, 2022.
- [58] F. Wang, H. Zhang, M. Liu, X. Zhang, D. Yang and C. Zhang, “An effective pemfc system shutdown purge strategy for improving the purging effect of liquid water and the dehydration of stack,” *International Journal of Hydrogen Energy*, vol. 48, no. 74, pp. 28 891–28 905, 2023.
- [59] L. Strandberg, “Electrode Degradation in Polymer Electrolyte Fuel Cells,” Ph.D. dissertation, Chalmers Tekniska Hogskola (Sweden), 2023.
- [60] J. Niemantsverdriet and I Chorkendorff, *Concepts of modern catalysis and kinetics*. John Wiley & Sons, 2006.

- [61] S. Ghosh, "Fertiliser Technology: Fractured Profile of Self-Reliance," *Economic and Political Weekly*, pp. 698–705, 1986.
- [62] F. H. Blanding, "Reaction rates in catalytic cracking of petroleum," *Industrial & Engineering Chemistry*, vol. 45, no. 6, pp. 1186–1197, 1953.
- [63] N. Corrigan, S. Shanmugam, J. Xu and C. Boyer, "Photocatalysis in organic and polymer synthesis," *Chemical Society Reviews*, vol. 45, no. 22, pp. 6165–6212, 2016.
- [64] J. P. Lutz, M. D. Hannigan and A. J. McNeil, "Polymers synthesized via catalyst-transfer polymerization and their applications," *Coordination Chemistry Reviews*, vol. 376, pp. 225–247, 2018.
- [65] J. R. Rostrup-Nielsen, "Catalytic steam reforming," in *Catalysis*, Springer, 1984, pp. 1–117.
- [66] S. Sá, H. Silva, L. Brandão, J. M. Sousa and A. Mendes, "Catalysts for methanol steam reforming—A review," *Applied Catalysis B: Environmental*, vol. 99, no. 1–2, pp. 43–57, 2010.
- [67] J. Li, X. Meng and F.-S. Xiao, "Zeolites for control of NO_x emissions: Opportunities and challenges," *Chem Catalysis*, 2021.
- [68] L. Zhang *et al.*, "Recent advances in the preparation of zeolites for the selective catalytic reduction of NO_x in diesel engines," *Reaction Chemistry & Engineering*, vol. 4, no. 6, pp. 975–985, 2019.
- [69] J. Wang, H. Chen, Z. Hu, M. Yao and Y. Li, "A review on the Pd-based three-way catalyst," *Catalysis Reviews*, vol. 57, no. 1, pp. 79–144, 2015.
- [70] S. Rood, S. Eslava, A. Manigrasso and C. Bannister, "Recent advances in gasoline three-way catalyst formulation: A review," *Proceedings of the Institution of Mechanical Engineers, Part D: Journal of Automobile Engineering*, vol. 234, no. 4, pp. 936–949, 2020.
- [71] I. Chorkendorff and J. W. Niemantsverdriet, *Concepts of modern catalysis and kinetics*. John Wiley & Sons, 2017.
- [72] E. Roduner, "Understanding catalysis," *Chemical Society Reviews*, vol. 43, no. 24, pp. 8226–8239, 2014.
- [73] K. J. Laidler, "The development of the arrhenius equation," *Journal of chemical Education*, vol. 61, no. 6, p. 494, 1984.
- [74] H. Ooka, J. Huang and K. S. Exner, "The Sabatier principle in electrocatalysis: Basics, limitations, and extensions," *Frontiers in Energy Research*, vol. 9, p. 654460, 2021.
- [75] E. Whittaker, *A History of the Theories of Aether and Electricity: Vol. I: The Classical Theories; Vol. II: The Modern Theories, 1900–1926*. Courier Dover Publications, 1989, vol. 1.
- [76] A. Volta and J. Banks, "I. On the electricity excited by the mere contact of conducting substances of different kinds," *The Philosophical Magazine*, vol. 7, no. 28, pp. 289–311, 1800.

- [77] A. Tribe, "III. experimental contributions to the theory of electrolysis," *Proceedings of the Royal Society of London*, vol. 24, no. 164-170, pp. 308-315, 1876.
- [78] E. Fabbri and T. J. Schmidt, *Oxygen evolution reaction—the enigma in water electrolysis*, 2018.
- [79] W. R. Grove, "Lxxii. on a gaseous voltaic battery," *The London, Edinburgh, and Dublin Philosophical Magazine and Journal of Science*, vol. 21, no. 140, pp. 417-420, 1842.
- [80] Cambridge Independent. "Apollo 11 mission 50 years on: The Cambridge scientist who helped put man on the moon." (2019), [Online]. Available: <https://www.cambridgeindependent.co.uk/news/apollo-11-mission-50-years-on-the-cambridge-scientist-who-helped-put-man-on-the-moon-9077166/> (visited on 10/10/2022).
- [81] A. J. Bard, L. R. Faulkner and H. S. White, *Electrochemical methods: fundamentals and applications*. John Wiley & Sons, 2022.
- [82] E. J. Dickinson and A. J. Wain, "The butler-volmer equation in electrochemical theory: Origins, value, and practical application," *Journal of Electroanalytical Chemistry*, vol. 872, p. 114 145, 2020.
- [83] S. Anantharaj and S. Noda, "How properly are we interpreting the tafel lines in energy conversion electrocatalysis?" *Materials today energy*, vol. 29, p. 101 123, 2022.
- [84] M. Pourbaix, *ATLAS OF ELECTROCHEMICAL EQUILIBRIA IN AQUEOUS SOLUTIONS*. National Association of Corrosion Engineers, 1974.
- [85] G. McLean, T. Niet, S. Prince-Richard and N. Djilali, "An assessment of alkaline fuel cell technology," *International Journal of Hydrogen Energy*, vol. 27, no. 5, pp. 507-526, 2002.
- [86] N. Sazali, W. N. Wan Salleh, A. S. Jamaludin and M. N. Mhd Razali, "New perspectives on fuel cell technology: A brief review," *Membranes*, vol. 10, no. 5, p. 99, 2020.
- [87] A. Choudhury, H. Chandra and A. Arora, "Application of solid oxide fuel cell technology for power generation—a review," *Renewable and Sustainable Energy Reviews*, vol. 20, pp. 430-442, 2013.
- [88] M. L. Perry, T. F. Fuller *et al.*, "A historical perspective of fuel cell technology in the 20th century," *Journal-Electrochemical Society*, vol. 149, no. 7, S59-S67, 2002.
- [89] K. Jiao *et al.*, "Designing the next generation of proton-exchange membrane fuel cells," *Nature*, vol. 595, no. 7867, pp. 361-369, 2021.
- [90] S. Katayama, M. Matsumoto, H. Imai, T. Asaoka and K. Amemiya, "Comparison of MEA Degradation through FCV Actual Driving Test and Load-Cycle Durability Test," *ECS Transactions*, vol. 112, no. 4, p. 157, 2023.

- [91] J Marcinkoski, R Vijayagopal, J Adams, B James, J Kopasz and R Ahluwalia, "DOE Advanced Truck Technologies-Subsection of the Electrified Powertrain Roadmap," *DOE, Argonne*, 2019.
- [92] L. Eudy and M. B. Post, "Fuel cell buses in us transit fleets: Current status 2017," National Renewable Energy Lab.(NREL), Golden, CO (United States), Tech. Rep., 2017.
- [93] A. Lozanovski, N. Whitehouse, N. Ko and S. Whitehouse, "Sustainability assessment of fuel cell buses in public transport," *Sustainability*, vol. 10, no. 5, p. 1480, 2018.
- [94] Scania, [Accessed 17-01-2025], 2020. [Online]. Available: <https://www.scania.com/group/en/home/newsroom/news/2020/norwegian-wholesaler-asko-puts-hydrogen-powered-fuel-cell-electric-scania-trucks-on-the-road.html>.
- [95] H. M. Company, [Accessed 17-01-2025], 2024. [Online]. Available: <https://www.hyundaimotorgroup.com/story/CONT000000000161400>.
- [96] U.S Department of Energy, *DOE H₂ Heavy Duty Truck Targets*, <https://www.energy.gov/sites/prod/files/2020/02/f71/fcto-compressed-gas-storage-workshop-2020-adams.pdf>, [Accessed 04-06-2024], 2020.
- [97] A. C. Frey, D. Bosak, J. Stonham, C. M. Sangan and O. J. Pountney, "Liquid cooling of fuel cell powered aircraft: The effect of coolants on thermal management," *Journal of Engineering for Gas Turbines and Power*, vol. 146, no. 11, 2024.
- [98] V. Cigolotti, M. Genovese and P. Fragiaco, "Comprehensive review on fuel cell technology for stationary applications as sustainable and efficient poly-generation energy systems," *Energies*, vol. 14, no. 16, p. 4963, 2021.
- [99] J Narayana Das, "Fuel cell technologies for defence applications," in *Energy Engineering: Proceedings of CAETS 2015 Convocation on Pathways to Sustainability*, Springer, 2017, pp. 9–18.
- [100] N. Dyantyi, A. Parsons, C. Sita and S. Pasupathi, "Pemfc for aeronautic applications: A review on the durability aspects," *Open Engineering*, vol. 7, no. 1, pp. 287–302, 2017.
- [101] F. Calili-Cankir, M. S. Ismail, D. B. Ingham, K. J. Hughes, L. Ma and M. Pourkashanian, "Air-breathing polymer electrolyte fuel cells: A review," *Renewable Energy*, vol. 213, pp. 86–108, 2023.
- [102] T. Yoshida and K. Kojima, "Toyota MIRAI fuel cell vehicle and progress toward a future hydrogen society," *The Electrochemical Society Interface*, vol. 24, no. 2, p. 45, 2015.
- [103] L. Doosan Fuel Cell Co., *World's Largest Hydrogen Fuel Cell Power Plant Jointly Built By Doosan Fuel Cell Put Into Service*, https://www.doosanfuelcell.com/en/media-center/medi-0101_view/?id=57, [Accessed 01-10-2024], 2021.

- [104] R. M. Ormerod, "Solid oxide fuel cells," *Chemical Society Reviews*, vol. 32, no. 1, pp. 17–28, 2003.
- [105] S. J. Hamrock and M. A. Yandrasits, "Proton exchange membranes for fuel cell applications," *Journal of Macromolecular Science, Part C: Polymer Reviews*, vol. 46, no. 3, pp. 219–244, 2006.
- [106] V. Vishnyakov, "Proton exchange membrane fuel cells," *Vacuum*, vol. 80, no. 10, pp. 1053–1065, 2006.
- [107] K. Miyatake, "Membrane Electrolytes, from Perfluoro Sulfonic Acid (PFSA) to Hydrocarbon Ionomers," in *Fuel Cells: Selected Entries from the Encyclopedia of Sustainability Science and Technology*, Springer, 2012, pp. 179–215.
- [108] W. Grot, *Fluorinated ionomers*. William Andrew, 2011.
- [109] N Yoshida, T Ishisaki, A Watakabe and M Yoshitake, "Characterization of Flemion® membranes for PEFC," *Electrochimica Acta*, vol. 43, no. 24, pp. 3749–3754, 1998.
- [110] Y. Garsany, R. W. Atkinson, M. B. Sassin, R. M. Hjelm, B. D. Gould and K. E. Swider-Lyons, "Improving PEMFC performance using short-side-chain low-equivalent-weight PFSA ionomer in the cathode catalyst layer," *Journal of The Electrochemical Society*, vol. 165, no. 5, F381–F391, 2018.
- [111] E. O. Balogun, N. Hussain, J. Chamier and P. Barendse, "Performance and durability studies of perfluorosulfonic acid ionomers as binders in PEMFC catalyst layers using Electrochemical Impedance Spectroscopy," *International Journal of Hydrogen Energy*, vol. 44, no. 60, pp. 32 219–32 230, 2019.
- [112] V. Arcella, C. Troglia and A. Ghielmi, "Hyflon ion membranes for fuel cells," *Industrial & engineering chemistry research*, vol. 44, no. 20, pp. 7646–7651, 2005.
- [113] *Driving Fuel Cell Industry Change with GORE-SELECT® Membranes*, W. L. Gore & Associates, 2023. [Online]. Available: https://www.gore.com/system/files/2023-08/GORE-AES-Fuel-Cell-Portfolio-Datasheet-EN_0.pdf (visited on 12/04/2024).
- [114] A. Kusoglu and A. Z. Weber, "New insights into perfluorinated sulfonic-acid ionomers," *Chemical reviews*, vol. 117, no. 3, pp. 987–1104, 2017.
- [115] M. A. Hickner, H. Ghassemi, Y. S. Kim, B. R. Einsla and J. E. McGrath, "Alternative polymer systems for proton exchange membranes (PEMs)," *Chemical reviews*, vol. 104, no. 10, pp. 4587–4612, 2004.
- [116] T. A. Zawodzinski *et al.*, "Water uptake by and transport through Nafion® 117 membranes," *Journal of the electrochemical society*, vol. 140, no. 4, p. 1041, 1993.
- [117] M. Saito, K. Hayamizu and T. Okada, "Temperature dependence of ion and water transport in perfluorinated ionomer membranes for fuel cells," *The Journal of Physical Chemistry B*, vol. 109, no. 8, pp. 3112–3119, 2005.

- [118] M. K. Petersen and G. A. Voth, "Characterization of the solvation and transport of the hydrated proton in the perfluorosulfonic acid membrane Nafion," *The Journal of Physical Chemistry B*, vol. 110, no. 37, pp. 18 594–18 600, 2006.
- [119] K. D. Baik, B. K. Hong and M. S. Kim, "Effects of operating parameters on hydrogen crossover rate through Nafion® membranes in polymer electrolyte membrane fuel cells," *Renewable Energy*, vol. 57, pp. 234–239, 2013.
- [120] C. Francia, V. S. Ijeri, S. Specchia and P. Spinelli, "Estimation of hydrogen crossover through Nafion® membranes in PEMFCs," *Journal of Power Sources*, vol. 196, no. 4, pp. 1833–1839, 2011.
- [121] J. Zhang, Y. Tang, C. Song, J. Zhang and H. Wang, "PEM fuel cell open circuit voltage (OCV) in the temperature range of 23 °C to 120 °C," *Journal of power sources*, vol. 163, no. 1, pp. 532–537, 2006.
- [122] D. F. Cells, *DuPont Nafion PFSA membranes N 115, N 117, N 1110*, 2012.
- [123] J. Peron *et al.*, "Properties of Nafion® NR-211 membranes for PEMFCs," *Journal of Membrane Science*, vol. 356, no. 1-2, pp. 44–51, 2010.
- [124] D. Qiu, L. Peng, X. Lai, M. Ni and W. Lehnert, "Mechanical failure and mitigation strategies for the membrane in a proton exchange membrane fuel cell," *Renewable and Sustainable Energy Reviews*, vol. 113, p. 109 289, 2019.
- [125] Y. Nonobe, "Development of the fuel cell vehicle mirai," *IEEEJ Transactions on Electrical and Electronic Engineering*, vol. 12, no. 1, pp. 5–9, 2017.
- [126] C Yang, P Costamagna, S Srinivasan, J Benziger and A. B. Bocarsly, "Approaches and technical challenges to high temperature operation of proton exchange membrane fuel cells," *Journal of Power Sources*, vol. 103, no. 1, pp. 1–9, 2001.
- [127] C. Schmidt, T. Glück and G. Schmidt-Naake, "Modification of Nafion membranes by impregnation with ionic liquids," *Chemical Engineering & Technology: Industrial Chemistry-Plant Equipment-Process Engineering-Biotechnology*, vol. 31, no. 1, pp. 13–22, 2008.
- [128] A. Sahu, S Pitchumani, P Sridhar and A. Shukla, "Nafion and modified-Nafion membranes for polymer electrolyte fuel cells: An overview," *Bulletin of Materials Science*, vol. 32, no. 3, pp. 285–294, 2009.
- [129] A. Chandan *et al.*, "High temperature (HT) polymer electrolyte membrane fuel cells (PEMFC)—A review," *Journal of Power Sources*, vol. 231, pp. 264–278, 2013.
- [130] R. Rosli *et al.*, "A review of high-temperature proton exchange membrane fuel cell (HT-PEMFC) system," *International Journal of Hydrogen Energy*, vol. 42, no. 14, pp. 9293–9314, 2017.

- [131] J. Zhang, Y. Tang, C. Song, X. Cheng, J. Zhang and H. Wang, "Pem fuel cells operated at 0% relative humidity in the temperature range of 23–120 c," *Electrochimica acta*, vol. 52, no. 15, pp. 5095–5101, 2007.
- [132] S. C. Yeo and A Eisenberg, "Physical properties and supermolecular structure of perfluorinated ion-containing (Nafion) polymers," *Journal of applied polymer science*, vol. 21, no. 4, pp. 875–898, 1977.
- [133] H.-Y. Jung and J. W. Kim, "Role of the glass transition temperature of Nafion 117 membrane in the preparation of the membrane electrode assembly in a direct methanol fuel cell (DMFC)," *International Journal of Hydrogen Energy*, vol. 37, no. 17, pp. 12 580–12 585, 2012.
- [134] S. J. Osborn, M. K. Hassan, G. M. Divoux, D. W. Rhoades, K. A. Mauritz and R. B. Moore, "Glass transition temperature of perfluorosulfonic acid ionomers," *Macromolecules*, vol. 40, no. 10, pp. 3886–3890, 2007.
- [135] Z. Xu *et al.*, "Strategies for mitigating phosphoric acid leaching in high-temperature proton exchange membrane fuel cells," *Molecules*, vol. 29, no. 18, p. 4480, 2024.
- [136] ECHA European Chemicals Agency, *Next steps for PFAS restriction proposal*, <https://echa.europa.eu/-/next-steps-for-pfas-restriction-proposal>, [Accessed 27-03-2024], 2024.
- [137] H. Brunn, G. Arnold, W. Körner, G. Rippen, K. G. Steinhäuser and I. Valentin, "PFAS: forever chemicals—persistent, bioaccumulative and mobile. Reviewing the status and the need for their phase out and remediation of contaminated sites," *Environmental Sciences Europe*, vol. 35, no. 1, pp. 1–50, 2023.
- [138] A. J. Lewis, X. Yun, D. E. Spooner, M. J. Kurz, E. R. McKenzie and C. M. Sales, "Exposure pathways and bioaccumulation of per- and polyfluoroalkyl substances in freshwater aquatic ecosystems: Key considerations," *Science of the Total Environment*, vol. 822, p. 153 561, 2022.
- [139] L. Lesmeister, F. T. Lange, J. Breuer, A. Biegel-Engler, E. Giese and M. Scheurer, "Extending the knowledge about pfas bioaccumulation factors for agricultural plants—a review," *Science of The Total Environment*, vol. 766, p. 142 640, 2021.
- [140] M. Hwang, K. Nixon, R. Sun, C. Willis and Y. A. Elabd, "Sulfonated pentablock terpolymers as membranes and ionomers in hydrogen fuel cells," *Journal of Membrane Science*, vol. 633, p. 119 330, 2021.
- [141] J. Peron, Z. Shi and S. Holdcroft, "Hydrocarbon proton conducting polymers for fuel cell catalyst layers," *Energy & Environmental Science*, vol. 4, no. 5, pp. 1575–1591, 2011.
- [142] H. Nguyen *et al.*, "Hydrocarbon-based Pemion™ proton exchange membrane fuel cells with state-of-the-art performance," *Sustainable Energy & Fuels*, vol. 5, no. 14, pp. 3687–3699, 2021.

- [143] H. Nguyen, D. Dultanova, P. A. Heizmann, S. Vierrath and M. Breitwieser, "Improving the efficiency of fully hydrocarbonbased proton-exchange membrane fuel cells by ionomer content gradients in cathode catalyst layers," *Materials Advances*, no. 3, 8460–8468, 2022.
- [144] H. Liepold, H. Nguyen, P. A. Heizmann, C. Klose, S. Vierrath and A. Münchinger, "Gas transport resistance of hydrocarbon-based catalyst layers in proton-exchange membrane fuel cells," *Journal of The Electrochemical Society*, vol. 171, no. 5, p. 054509, 2024.
- [145] H. A. Gasteiger, S. S. Kocha, B. Sompalli and F. T. Wagner, "Activity benchmarks and requirements for Pt, Pt-alloy, and non-Pt oxygen reduction catalysts for PEMFCs," *Applied Catalysis B: Environmental*, vol. 56, no. 1-2, pp. 9–35, 2005.
- [146] E. Antolini, "Formation of carbon-supported PtM alloys for low temperature fuel cells: a review," *Materials chemistry and physics*, vol. 78, no. 3, pp. 563–573, 2003.
- [147] X. Yu and S. Ye, "Recent advances in activity and durability enhancement of Pt/C catalytic cathode in PEMFC: Part I. Physico-chemical and electronic interaction between Pt and carbon support, and activity enhancement of Pt/C catalyst," *Journal of power sources*, vol. 172, no. 1, pp. 133–144, 2007.
- [148] X. Yu and S. Ye, "Recent advances in activity and durability enhancement of Pt/C catalytic cathode in PEMFC: Part II: Degradation mechanism and durability enhancement of carbon supported platinum catalyst," *Journal of power sources*, vol. 172, no. 1, pp. 145–154, 2007.
- [149] D. Y. Chung, J. M. Yoo and Y.-E. Sung, "Highly durable and active Pt-based nanoscale design for fuel-cell oxygen-reduction electrocatalysts," *Advanced materials*, vol. 30, no. 42, p. 1704123, 2018.
- [150] S. C. Ball, S. L. Hudson, B. R. Theobald and D. Thompsett, "PtCo, a durable catalyst for automotive PEMFC?" *ECS Transactions*, vol. 11, no. 1, p. 1267, 2007.
- [151] F. Maillard, L. Dubau, J. Durst, M. Chatenet, J. André and E. Rossinot, "Durability of Pt₃Co/C nanoparticles in a proton-exchange membrane fuel cell: Direct evidence of bulk Co segregation to the surface," *Electrochemistry Communications*, vol. 12, no. 9, pp. 1161–1164, 2010.
- [152] S. Chen, H. A. Gasteiger, K. Hayakawa, T. Tada and Y. Shao-Horn, "Platinum-alloy cathode catalyst degradation in proton exchange membrane fuel cells: Nanometer-scale compositional and morphological changes," *Journal of the Electrochemical Society*, vol. 157, no. 1, A82, 2009.
- [153] K. Jayasayee, J. R. Van Veen, T. G. Manivasagam, S. Celebi, E. J. Hensen and F. A. De Bruijn, "Oxygen reduction reaction (ORR) activity and durability of carbon supported PtM (Co, Ni, Cu) alloys: Influence of particle size and non-noble metals," *Applied Catalysis B: Environmental*, vol. 111, pp. 515–526, 2012.

- [154] D. Li *et al.*, “Functional links between pt single crystal morphology and nanoparticles with different size and shape: The oxygen reduction reaction case,” *Energy & Environmental Science*, vol. 7, no. 12, pp. 4061–4069, 2014.
- [155] Y. Bing, H. Liu, L. Zhang, D. Ghosh and J. Zhang, “Nanostructured Pt-alloy electrocatalysts for PEM fuel cell oxygen reduction reaction,” *Chemical Society Reviews*, vol. 39, no. 6, pp. 2184–2202, 2010.
- [156] R. Brown *et al.*, “Unraveling the surface chemistry and structure in highly active sputtered Pt3Y catalyst films for the oxygen reduction reaction,” *ACS applied materials & interfaces*, vol. 12, no. 4, pp. 4454–4462, 2019.
- [157] R Brown *et al.*, “Surface composition of a highly active Pt3Y alloy catalyst for application in low temperature fuel cells,” *Fuel Cells*, vol. 20, no. 4, pp. 413–419, 2020.
- [158] P. Hernandez-Fernandez *et al.*, “Mass-selected nanoparticles of Pt x Y as model catalysts for oxygen electroreduction,” *Nature chemistry*, vol. 6, no. 8, pp. 732–738, 2014.
- [159] M. Nesselberger, S. Ashton, J. C. Meier, I. Katsounaros, K. J. Mayrhofer and M. Arenz, “The particle size effect on the oxygen reduction reaction activity of Pt catalysts: Influence of electrolyte and relation to single crystal models,” *Journal of the American Chemical Society*, vol. 133, no. 43, pp. 17 428–17 433, 2011.
- [160] S Garbarino, A Pereira, C Hamel, E Irissou, M Chaker and D Guay, “Effect of size on the electrochemical stability of Pt nanoparticles deposited on gold substrate,” *The Journal of Physical Chemistry C*, vol. 114, no. 7, pp. 2980–2988, 2010.
- [161] K. Wikander, H. Ekström, A. E. Palmqvist and G. Lindbergh, “On the influence of Pt particle size on the pemfc cathode performance,” *Electrochimica Acta*, vol. 52, no. 24, pp. 6848–6855, 2007.
- [162] Z Yang, S Ball, D Condit and M Gummalla, “Systematic study on the impact of Pt particle size and operating conditions on pemfc cathode catalyst durability,” *Journal of The Electrochemical Society*, vol. 158, no. 11, B1439, 2011.
- [163] Z. Xu, H. Zhang, H. Zhong, Q. Lu, Y. Wang and D. Su, “Effect of particle size on the activity and durability of the Pt/C electrocatalyst for proton exchange membrane fuel cells,” *Applied Catalysis B: Environmental*, vol. 111, pp. 264–270, 2012.
- [164] S. Sharma and B. G. Pollet, “Support materials for pemfc and dmfc electrocatalysts—a review,” *Journal of Power Sources*, vol. 208, pp. 96–119, 2012.
- [165] “Carbon Black - Ketjenblack EC-600JD.” (2022), [Online]. Available: <https://www.fuelcellstore.com/ketjenblack-carbon-black-ec600jd> (visited on 01/11/2022).

- [166] A. Kongkanand and M. F. Mathias, "The priority and challenge of high-power performance of low-platinum proton-exchange membrane fuel cells," *The journal of physical chemistry letters*, vol. 7, no. 7, pp. 1127–1137, 2016.
- [167] G.-F. Li, D. Yang and P.-Y. Abel Chuang, "Defining nafion ionomer roles for enhancing alkaline oxygen evolution electrocatalysis," *ACS Catalysis*, vol. 8, no. 12, pp. 11 688–11 698, 2018.
- [168] K. Shinozaki, Y. Morimoto, B. S. Pivovar and S. S. Kocha, "Suppression of oxygen reduction reaction activity on Pt-based electrocatalysts from ionomer incorporation," *Journal of Power Sources*, vol. 325, pp. 745–751, 2016.
- [169] Y. Song, H. Xu, Y. Wei, H. R. Kunz, L. J. Bonville and J. M. Fenton, "Dependence of high-temperature pem fuel cell performance on nafion® content," *Journal of Power Sources*, vol. 154, no. 1, pp. 138–144, 2006.
- [170] Y. V. Yakovlev *et al.*, "Ionomer content effect on charge and gas transport in the cathode catalyst layer of proton-exchange membrane fuel cells," *Journal of Power Sources*, vol. 490, p. 229 531, 2021.
- [171] M.-R. Lee *et al.*, "Effects of ionomer carbon ratio and ionomer dispersity on the performance and durability of meas," *Fuel cells*, vol. 18, no. 2, pp. 129–136, 2018.
- [172] T. Hayashi, Y. Tabe and T. Chikahisa, "Model and experimental analysis of transport resistances of oxygen in various structures of pefc catalyst layer," *ECS Transactions*, vol. 75, no. 14, p. 373, 2016.
- [173] M. Chen, C. Zhao, F. Sun, J. Fan, H. Li and H. Wang, "Research progress of catalyst layer and interlayer interface structures in membrane electrode assembly (mea) for proton exchange membrane fuel cell (pemfc) system," *ETransportation*, vol. 5, p. 100 075, 2020.
- [174] L Cindrella *et al.*, "Gas diffusion layer for proton exchange membrane fuel cells—A review," *Journal of Power Sources*, vol. 194, no. 1, pp. 146–160, 2009.
- [175] G. Kaur, *PEM Fuel Cells: Fundamentals, Advanced Technologies, and Practical Application*. Elsevier, 2021.
- [176] F Basile, A Barbir and T. Veziroglu, *Compendium of Hydrogen Energy, Volume 3: Hydrogen Energy Conversion*. Elsevier, Woodgead Publishing, 2016.
- [177] P. C. Okonkwo and C. Otor, "A review of gas diffusion layer properties and water management in proton exchange membrane fuel cell system," *International Journal of Energy Research*, vol. 45, no. 3, pp. 3780–3800, 2021.
- [178] H. Li *et al.*, "A review of water flooding issues in the proton exchange membrane fuel cell," *Journal of Power Sources*, vol. 178, no. 1, pp. 103–117, 2008.

- [179] R. G. Akay and A. B. Yurtcan, *Direct Liquid Fuel Cells: Fundamentals, Advances and Future*. Academic Press, 2020.
- [180] K.-Q. Zhu *et al.*, “Optimization of gas diffusion layer thickness for proton exchange membrane fuel cells under steady-state and load-varying conditions,” *Energy Conversion and Management*, vol. 267, p. 115915, 2022.
- [181] H. Liu, Z. Hu, J. Li, L. Xu, Y. Shao and M. Ouyang, “Investigation on the optimal GDL thickness design for PEMFCs considering channel/rib geometry matching and operating conditions,” *Energy*, vol. 282, p. 128780, 2023.
- [182] B. H. Lim *et al.*, “Comparison of catalyst-coated membranes and catalyst-coated substrate for PEMFC membrane electrode assembly: A review,” *Chinese Journal of Chemical Engineering*, vol. 33, pp. 1–16, 2021.
- [183] X. Li and I. Sabir, “Review of bipolar plates in pem fuel cells: Flow-field designs,” *International journal of hydrogen energy*, vol. 30, no. 4, pp. 359–371, 2005.
- [184] H. Kahraman and M. F. Orhan, “Flow field bipolar plates in a proton exchange membrane fuel cell: Analysis & modeling,” *Energy Conversion and Management*, vol. 133, pp. 363–384, 2017.
- [185] J Scholta, B Rohland, V Trapp and U Focken, “Investigations on novel low-cost graphite composite bipolar plates,” *Journal of Power Sources*, vol. 84, no. 2, pp. 231–234, 1999.
- [186] Y. Song *et al.*, “Review on current research of materials, fabrication and application for bipolar plate in proton exchange membrane fuel cell,” *International Journal of Hydrogen Energy*, vol. 45, no. 54, pp. 29832–29847, 2020.
- [187] S. Kim and I. Hong, “Effects of humidity and temperature on a proton exchange membrane fuel cell (pemfc) stack,” *Journal of Industrial and Engineering Chemistry*, vol. 14, no. 3, pp. 357–364, 2008.
- [188] K. Neyerlin, H. A. Gasteiger, C. K. Mittelsteadt, J. Jorne and W. Gu, “Effect of relative humidity on oxygen reduction kinetics in a pemfc,” *Journal of The Electrochemical Society*, vol. 152, no. 6, A1073, 2005.
- [189] R Eckl, W Zehntner, C Leu and U Wagner, “Experimental analysis of water management in a self-humidifying polymer electrolyte fuel cell stack,” *Journal of Power Sources*, vol. 138, no. 1-2, pp. 137–144, 2004.
- [190] Y. H. Park and J. A. Caton, “An experimental investigation of electro-osmotic drag coefficients in a polymer electrolyte membrane fuel cell,” *International Journal of Hydrogen Energy*, vol. 33, no. 24, pp. 7513–7520, 2008.
- [191] G. W. Thomson, “The antoine equation for vapor-pressure data.,” *Chemical reviews*, vol. 38, no. 1, pp. 1–39, 1946.

- [192] S Rodosik, J.-P. Poirot-Crouvezier and Y Bultel, "Impact of humidification by cathode exhaust gases recirculation on a pemfc system for automotive applications," *International journal of hydrogen energy*, vol. 44, no. 25, pp. 12 802–12 817, 2019.
- [193] M. V. Williams, H. R. Kunz and J. M. Fenton, "Operation of Nafion®-based PEM fuel cells with no external humidification: influence of operating conditions and gas diffusion layers," *Journal of Power Sources*, vol. 135, no. 1-2, pp. 122–134, 2004.
- [194] H. Kanani, M. Shams, M. Hasheminasab and A. Bozorgnezhad, "Model development and optimization of operating conditions to maximize PEMFC performance by response surface methodology," *Energy Conversion and Management*, vol. 93, pp. 9–22, 2015.
- [195] H. Xu, R. Boroup, E. Broscha, F. Gazon and B. Pivovar, "Effect of relative humidity on membrane degradation rate and mechanism in pem fuel cells," *Ecs Transactions*, vol. 6, no. 13, p. 51, 2007.
- [196] U. Basuli *et al.*, "Properties and degradation of the gasket component of a proton exchange membrane fuel cell—a review," *Journal of Nanoscience and Nanotechnology*, vol. 12, no. 10, pp. 7641–7657, 2012.
- [197] S Asghari, M. Shahsamandi and M. A. Khorasani, "Design and manufacturing of end plates of a 5 kw pem fuel cell," *International journal of hydrogen energy*, vol. 35, no. 17, pp. 9291–9297, 2010.
- [198] Y.-J. Sohn *et al.*, "Operating characteristics of an air-cooling pemfc for portable applications," *Journal of Power Sources*, vol. 145, no. 2, pp. 604–609, 2005.
- [199] R. D. Dicks A., *Fuel Cell Systems Explained*. Wiley, 2018.
- [200] M. H. Bargal, M. A. Abdelkareem, Q. Tao, J. Li, J. Shi and Y. Wang, "Liquid cooling techniques in proton exchange membrane fuel cell stacks: A detailed survey," *Alexandria Engineering Journal*, vol. 59, no. 2, pp. 635–655, 2020.
- [201] R. Adžić, *Recent advances in the kinetics of oxygen reduction*. Wiley-VCH, New York, 1998, vol. 197.
- [202] L. Gubler, S. M. Dockheer and W. H. Koppenol, "Radical (HO•, H• and HOO•) formation and ionomer degradation in polymer electrolyte fuel cells," *Journal of The Electrochemical Society*, vol. 158, no. 7, B755, 2011.
- [203] X. Wang *et al.*, "Review of metal catalysts for oxygen reduction reaction: From nanoscale engineering to atomic design," *Chem*, vol. 5, no. 6, pp. 1486–1511, 2019.
- [204] A. R. Kucernak and C. Zalitis, "General models for the electrochemical hydrogen oxidation and hydrogen evolution reactions: Theoretical derivation and experimental results under near mass-transport free conditions," *The Journal of Physical Chemistry C*, vol. 120, no. 20, pp. 10 721–10 745, 2016.

- [205] J. Durst, C. Simon, F. Hasché and H. A. Gasteiger, “Hydrogen oxidation and evolution reaction kinetics on carbon supported Pt, Ir, Rh, and Pd electrocatalysts in acidic media,” *Journal of The Electrochemical Society*, vol. 162, no. 1, F190, 2014.
- [206] J. Wang, a. N. Markovic and R. Adzic, “Kinetic analysis of oxygen reduction on Pt (111) in acid solutions: intrinsic kinetic parameters and anion adsorption effects,” *The Journal of Physical Chemistry B*, vol. 108, no. 13, pp. 4127–4133, 2004.
- [207] Y. Wang, H. Yuan, A. Martinez, P. Hong, H. Xu and F. R. Bockmiller, “Polymer electrolyte membrane fuel cell and hydrogen station networks for automobiles: Status, technology, and perspectives,” *Advances in Applied Energy*, vol. 2, p. 100 011, 2021.
- [208] L. Zhang *et al.*, “Ti₄O₇ supported Ru@Pt core-shell catalyst for CO-tolerance in PEM fuel cell hydrogen oxidation reaction,” *Applied energy*, vol. 103, pp. 507–513, 2013.
- [209] F. Bortoloti, A. Garcia and A. Angelo, “Electronic effect in intermetallic electrocatalysts with low susceptibility to CO poisoning during hydrogen oxidation,” *international journal of hydrogen energy*, vol. 40, no. 34, pp. 10 816–10 824, 2015.
- [210] S. Lee, S. Mukerjee, E. Ticianelli and J. McBreen, “Electrocatalysis of CO tolerance in hydrogen oxidation reaction in PEM fuel cells,” *Electrochimica Acta*, vol. 44, no. 19, pp. 3283–3293, 1999.
- [211] W. M. Haynes, D. R. Lide and T. J. Bruno, *CRC handbook of chemistry and physics*. CRC press, 2016.
- [212] S. Bhattacharjee, *Molar enthalpy of formation of various substances*. [Online]. Available: https://www.ohio.edu/mechanical/thermo/property_tables/combustion/Enth_Formation.html (visited on 01/11/2022).
- [213] M. Blal, A. Benatiallah, A. NeÇaibia, S. Lachtar, N. Sahouane and A. Belasri, “Contribution and investigation to compare models parameters of (PEMFC), comprehensives review of fuel cell models and their degradation,” *Energy*, vol. 168, pp. 182–199, 2019.
- [214] M. Butori, B. Eriksson, N. Nikolić, C. Lagergren, G. Lindbergh and R. W. Lindström, “The effect of oxygen partial pressure and humidification in proton exchange membrane fuel cells at intermediate temperature (80–120° C),” *Journal of Power Sources*, vol. 563, p. 232 803, 2023.
- [215] S. Stariha *et al.*, “Recent advances in catalyst accelerated stress tests for polymer electrolyte membrane fuel cells,” *Journal of The Electrochemical Society*, vol. 165, no. 7, F492, 2018.
- [216] K. Kodama, T. Nagai, A. Kuwaki, R. Jinnouchi and Y. Morimoto, “Challenges in applying highly active Pt-based nanostructured catalysts for oxygen reduction reactions to fuel cell vehicles,” *Nature nanotechnology*, vol. 16, no. 2, pp. 140–147, 2021.

- [217] G. S. Harzer, J. N. Schwämmlein, A. M. Damjanović, S. Ghosh and H. A. Gasteiger, “Cathode loading impact on voltage cycling induced pemfc degradation: A voltage loss analysis,” *Journal of The Electrochemical Society*, vol. 165, no. 6, F3118–F3131, 2018.
- [218] R. Petrone, D. Hissel, M. Péra, D. Chamagne and R. Gouriveau, “Accelerated stress test procedures for pem fuel cells under actual load constraints: State-of-art and proposals,” *International Journal of Hydrogen Energy*, vol. 40, no. 36, pp. 12 489–12 505, 2015.
- [219] J. Wu *et al.*, “A review of pem fuel cell durability: Degradation mechanisms and mitigation strategies,” *Journal of Power Sources*, vol. 184, no. 1, pp. 104–119, 2008.
- [220] M. Khorshidian and M. Sedighi, “A review of the main mechanisms of catalyst layer degradation in polymer electrolyte membrane fuel cell (pemfc) and different performance recovery methods,” *Hydrogen, Fuel Cell & Energy Storage*, vol. 6, no. 2, pp. 91–115, 2019.
- [221] S. Gottesfeld and J. Pafford, “A new approach to the problem of carbon monoxide poisoning in fuel cells operating at low temperatures,” *J. Electrochem. Soc.*, vol. 135, no. 10, pp. 2651–2652, 1988.
- [222] L. Dubau *et al.*, “A review of pem fuel cell durability: Materials degradation, local heterogeneities of aging and possible mitigation strategies,” *Wiley Interdisciplinary Reviews: Energy and Environment*, vol. 3, no. 6, pp. 540–560, 2014.
- [223] Y. Yu, H. Li, H. Wang, X.-Z. Yuan, G. Wang and M. Pan, “A review on performance degradation of proton exchange membrane fuel cells during startup and shutdown processes: Causes, consequences, and mitigation strategies,” *Journal of Power Sources*, vol. 205, pp. 10–23, 2012.
- [224] L. Liu, H. Li and G. Avgouropoulos, “A review of porous polytetrafluoroethylene reinforced sulfonic acid-based proton exchange membranes for fuel cells,” *International Journal of Hydrogen Energy*, vol. 50, pp. 501–527, 2024.
- [225] G. Li, W. Kujawski and E. Rynkowska, “Advancements in proton exchange membranes for high-performance high-temperature proton exchange membrane fuel cells (ht-pemfc),” *Reviews in Chemical Engineering*, vol. 38, no. 3, pp. 327–346, 2022.
- [226] J. Park, H. Oh, T. Ha, Y. I. Lee and K. Min, “A review of the gas diffusion layer in proton exchange membrane fuel cells: Durability and degradation,” *Applied Energy*, vol. 155, pp. 866–880, 2015.
- [227] N. F. Asri, T. Husaini, A. B. Sulong, E. H. Majlan and W. R. W. Daud, “Coating of stainless steel and titanium bipolar plates for anticorrosion in pemfc: A review,” *International Journal of Hydrogen Energy*, vol. 42, no. 14, pp. 9135–9148, 2017.
- [228] B. Sompalli, B. A. Litteer, W. Gu and H. A. Gasteiger, “Membrane degradation at catalyst layer edges in PEMFC MEAs,” *Journal of The Electrochemical Society*, vol. 154, no. 12, B1349, 2007.

- [229] J. Tan, Y. Chao, J. Van Zee and W. Lee, "Degradation of elastomeric gasket materials in PEM fuel cells," *Materials Science and Engineering: A*, vol. 445, pp. 669–675, 2007.
- [230] F. N. Büchi, M. Inaba and T. J. Schmidt, *Polymer electrolyte fuel cell durability*. Springer, 2009, vol. 1.
- [231] H. Pourrahmani *et al.*, "A review on the long-term performance of proton exchange membrane fuel cells: From degradation modeling to the effects of bipolar plates, sealings, and contaminants," *Energies*, vol. 15, no. 14, p. 5081, 2022.
- [232] A. L. Dicks and D. A. Rand, *Fuel cell systems explained*. John Wiley & Sons, 2018.
- [233] C. M. Sanchez-Sanchez and A. J. Bard, "Hydrogen peroxide production in the oxygen reduction reaction at different electrocatalysts as quantified by scanning electrochemical microscopy," *Analytical chemistry*, vol. 81, no. 19, pp. 8094–8100, 2009.
- [234] O Antoine and R Durand, "RRDE study of oxygen reduction on Pt nanoparticles inside Nafion®: H₂O₂ production in PEMFC cathode conditions," *Journal of Applied Electrochemistry*, vol. 30, no. 7, pp. 839–844, 2000.
- [235] A. A. Topalov *et al.*, "Dissolution of platinum: Limits for the deployment of electrochemical energy conversion?" *Angewandte Chemie International Edition*, vol. 51, no. 50, pp. 12 613–12 615, 2012.
- [236] A. A. Topalov, S. Cherevko, A. R. Zeradjanin, J. C. Meier, I. Katsounaros and K. J. Mayrhofer, "Towards a comprehensive understanding of platinum dissolution in acidic media," *Chemical Science*, vol. 5, no. 2, pp. 631–638, 2014.
- [237] A. Pavlišič, P. Jovanovič, V. S. Šelih, M. Šala, N. Hodnik and M. Gaberšček, "Platinum dissolution and redeposition from pt/c fuel cell electrocatalyst at potential cycling," *Journal of The Electrochemical Society*, vol. 165, no. 6, F3161–F3165, 2018.
- [238] F. J. Perez-Alonso *et al.*, "The effect of size on the oxygen electroreduction activity of mass-selected platinum nanoparticles," *Angewandte Chemie International Edition*, vol. 51, no. 19, pp. 4641–4643, 2012.
- [239] W. Bi, G. E. Gray and T. F. Fuller, "PEM fuel cell Pt/C dissolution and deposition in nafion electrolyte," *Electrochemical and solid-state letters*, vol. 10, no. 5, B101, 2007.
- [240] Y. Zhu, Z. Qu, G. Zhang and B. Yu, "A one-dimensional model for Pt degradation and precipitation in proton exchange membrane fuel cell considering Pt nucleation, particle size growth, and band formation," *Electrochimica Acta*, vol. 475, p. 143 590, 2024.
- [241] Z. Zheng, L. Luo, S. Shen, G. Wei and J. Zhang, "Insight into the potential strategies for mitigating pt degradation in proton exchange membrane fuel cells (pemfcs): From the perspective of pt ion transport," *Journal of Power Sources*, vol. 522, p. 230 999, 2022.

- [242] P. Schneider, C. Sadeler, A.-C. Scherzer, N. Zamel and D. Gerteisen, "Fast and reliable state-of-health model of a pem cathode catalyst layer," *Journal of The Electrochemical Society*, vol. 166, no. 4, F322, 2019.
- [243] R. L. Borup, J. R. Davey, F. H. Garzon, D. L. Wood and M. A. Inbody, "PEM fuel cell electrocatalyst durability measurements," *Journal of Power Sources*, vol. 163, no. 1, pp. 76–81, 2006.
- [244] C. A. Reiser *et al.*, "A reverse-current decay mechanism for fuel cells," *Electrochemical and Solid-State Letters*, vol. 8, no. 6, A273, 2005.
- [245] J. Zhao, Z. Tu and S. H. Chan, "Carbon corrosion mechanism and mitigation strategies in a proton exchange membrane fuel cell (PEMFC): A review," *Journal of Power Sources*, vol. 488, p. 229 434, 2021.
- [246] Q. Shen *et al.*, "Study on the processes of start-up and shutdown in proton exchange membrane fuel cells," *Journal of Power Sources*, vol. 189, no. 2, pp. 1114–1119, 2009.
- [247] K. Kinoshita, "Carbon: Electrochemical and physicochemical properties," 1988.
- [248] L. Roen, C. Paik and T. Jarvi, "Electrocatalytic corrosion of carbon support in PEMFC cathodes," *Electrochemical and solid-state letters*, vol. 7, no. 1, A19, 2003.
- [249] A. Perego *et al.*, "Investigation of cathode catalyst layer interfaces evolution during accelerated stress tests for polymer electrolyte fuel cells," *Applied Catalysis B: Environmental*, vol. 301, p. 120 810, 2022.
- [250] Y. Luo and K. Jiao, "Cold start of proton exchange membrane fuel cell," *Progress in Energy and Combustion Science*, vol. 64, pp. 29–61, 2018.
- [251] R. Mukundan *et al.*, *V.D.3 Accelerated Testing Validation*. United States Department of Energy, 2013.
- [252] Z. Wan, H. Chang, S. Shu, Y. Wang and H. Tang, "A review on cold start of proton exchange membrane fuel cells," *Energies*, vol. 7, no. 5, pp. 3179–3203, 2014.
- [253] C. Song *et al.*, "Pem fuel cell reaction kinetics in the temperature range of 23–120 c," *Electrochimica Acta*, vol. 52, no. 7, pp. 2552–2561, 2007.
- [254] M. Butori, B. Eriksson, N. Nikolić, C. Lagergren, G. Lindbergh and R. W. Lindström, "Ionic conductivity and hydrogen crossover for it-pemfcs: Influence of pressure, temperature, relative humidity and reinforcement," *International Journal of Hydrogen Energy*, vol. 95, pp. 1158–1170, 2024.
- [255] B.-T. Huang *et al.*, "Experimental investigation of air relative humidity (RH) cycling tests on MEA/cell aging in PEMFC part I: study of high RH cycling test with air RH at 62%/100%," *Fuel Cells*, vol. 12, no. 3, pp. 335–346, 2012.
- [256] M. Hu and G. Cao, "Research on the long-term stability of a pemfc stack: Analysis of pinhole evolution," *international journal of hydrogen energy*, vol. 39, no. 15, pp. 7940–7954, 2014.

- [257] H. Lee *et al.*, “Pinhole formation in pemfc membrane after electrochemical degradation and wet/dry cycling test,” *Korean Journal of Chemical Engineering*, vol. 28, pp. 487–491, 2011.
- [258] J.-H. Choi, H. E. Kang, D.-J. Kim and Y. S. Yoon, “A comprehensive review of stainless-steel bipolar plate coatings and their role in mitigating corrosion in aggressive proton-exchange membrane fuel cells environments,” *Chemical Engineering Journal*, p. 152 662, 2024.
- [259] J.-H. Wee and K.-Y. Lee, “Overview of the development of CO-tolerant anode electrocatalysts for proton-exchange membrane fuel cells,” *Journal of Power Sources*, vol. 157, no. 1, pp. 128–135, 2006.
- [260] Q. Li, R. He, J.-A. Gao, J. O. Jensen and N. J. Bjerrum, “The CO poisoning effect in PEMFCs operational at temperatures up to 200 °C,” *Journal of the Electrochemical Society*, vol. 150, no. 12, A1599, 2003.
- [261] S. Cherevko, G. P. Keeley, N. Kulyk and K. J. Mayrhofer, “Pt submonolayer on Au: System stability and insights into platinum electrochemical dissolution,” *Journal of The Electrochemical Society*, vol. 163, no. 3, H228, 2016.
- [262] G. Sauerbrey, “Verwendung von schwingquarzen zur wägung dünner schichten und zur mikrowägung,” *Zeitschrift für physik*, vol. 155, no. 2, pp. 206–222, 1959.
- [263] J. Kankare, “Sauerbrey equation of quartz crystal microbalance in liquid medium,” *Langmuir*, vol. 18, no. 18, pp. 7092–7094, 2002.
- [264] Biologic. “QCM: When is the Sauerbrey equation valid?” (2024), [Online]. Available: [https://www.biologic.net/topics/bluqcm-when-is-the-sauerbrey-equation-valid/#:~:text=Equation%20\(1\)%20is%20called%20the%20without%20any%20energy%20loss.](https://www.biologic.net/topics/bluqcm-when-is-the-sauerbrey-equation-valid/#:~:text=Equation%20(1)%20is%20called%20the%20without%20any%20energy%20loss.) (visited on 11/03/2025).
- [265] J. A. Gilbert *et al.*, “In-operando anomalous small-angle x-ray scattering investigation of pt3co catalyst degradation in aqueous and fuel cell environments,” *Journal of The Electrochemical Society*, vol. 162, no. 14, F1487, 2015.
- [266] T. Lazaridis, B. M. Stühmeier, H. A. Gasteiger and H. A. El-Sayed, “Capabilities and limitations of rotating disk electrodes versus membrane electrode assemblies in the investigation of electrocatalysts,” *Nature Catalysis*, vol. 5, no. 5, pp. 363–373, 2022.
- [267] T. Imhof, R. K. Della Bella, B. M. Stühmeier, H. A. Gasteiger and M. Ledendecker, “Towards a realistic prediction of catalyst durability from liquid half-cell tests,” *Physical Chemistry Chemical Physics*, vol. 25, no. 30, pp. 20 533–20 545, 2023.
- [268] H. Yu *et al.*, “Recreating fuel cell catalyst degradation in aqueous environments for identical-location scanning transmission electron microscopy studies,” *ACS applied materials & interfaces*, vol. 14, no. 18, pp. 20 418–20 429, 2022.

- [269] P. A. L. Torres *et al.*, “ORR Activity and Voltage-Cycling Stability of a Carbon-Supported PtxY Alloy Catalyst Evaluated in a PEM Fuel Cell,” *Journal of The Electrochemical Society*, vol. 170, no. 12, p. 124 503, 2023.
- [270] W. Sheng, Z. Zhuang, M. Gao, J. Zheng, J. G. Chen and Y. Yan, “Correlating hydrogen oxidation and evolution activity on platinum at different pH with measured hydrogen binding energy,” *Nature communications*, vol. 6, no. 1, pp. 1–6, 2015.
- [271] G. Karlberg, T. Jaramillo, E. Skulason, J. Rossmeisl, T. Bligaard and J. K. Nørskov, “Cyclic voltammograms for H on Pt (111) and Pt (100) from first principles,” *Physical review letters*, vol. 99, no. 12, p. 126 101, 2007.
- [272] T. Biegler, D. Rand and R. Woods, “Limiting oxygen coverage on platinized platinum; relevance to determination of real platinum area by hydrogen adsorption,” *Journal of Electroanalytical Chemistry and Interfacial Electrochemistry*, vol. 29, no. 2, pp. 269–277, 1971.
- [273] S. Brummer, “The use of large anodic galvanostatic transients to evaluate the maximum adsorption on platinum from formic acid solutions,” *The Journal of Physical Chemistry*, vol. 69, no. 2, pp. 562–571, 1965.
- [274] S. Trasatti and O. Petrii, “Real surface area measurements in electrochemistry,” *Pure and applied chemistry*, vol. 63, no. 5, pp. 711–734, 1991.
- [275] M. Inaba, T. Kinumoto, M. Kiriake, R. Umebayashi, A. Tasaka and Z. Ogumi, “Gas crossover and membrane degradation in polymer electrolyte fuel cells,” *Electrochimica Acta*, vol. 51, no. 26, pp. 5746–5753, 2006.
- [276] W. Mérida, D. Harrington, J. Le Canut and G McLean, “Characterisation of proton exchange membrane fuel cell (pemfc) failures via electrochemical impedance spectroscopy,” *Journal of power sources*, vol. 161, no. 1, pp. 264–274, 2006.
- [277] T. Springer, T. Zawodzinski, M. Wilson and S Gottesfeld, “Characterization of polymer electrolyte fuel cells using ac impedance spectroscopy,” *Journal of the Electrochemical Society*, vol. 143, no. 2, p. 587, 1996.
- [278] A. Kulikovskiy, “A fast low-current model for impedance of a pem fuel cell cathode at low air stoichiometry,” *Journal of The Electrochemical Society*, vol. 164, no. 9, F911, 2017.
- [279] Z. Wan *et al.*, “Determination of oxygen transport resistance in gas diffusion layer for polymer electrolyte fuel cells,” *International Journal of Energy Research*, vol. 42, no. 6, pp. 2225–2233, 2018.
- [280] V. B. Silva and A. Rouboa, “Hydrogen-fed PEMFC: Overvoltage analysis during an activation procedure,” *Journal of Electroanalytical Chemistry*, vol. 671, pp. 58–66, 2012.
- [281] T. W. Lim, S. H. Kim, S. Y. Ahn, B. K. Hong and B. K. Ahn, *System and method for activating fuel cell*, US Patent 8,455,121, 2013.

- [282] P. Pei, X. Fu, Z. Zhu, P. Ren and D. Chen, "Activation of polymer electrolyte membrane fuel cells: Mechanisms, procedures, and evaluation," *International Journal of Hydrogen Energy*, vol. 47, no. 59, pp. 24 897–24 915, 2022.
- [283] F. Van Der Linden, E. Pahon, S. Morando and D. Bouquain, "A review on the proton-exchange membrane fuel cell break-in physical principles, activation procedures, and characterization methods," *Journal of Power Sources*, vol. 575, p. 233 168, 2023.
- [284] M Zhiani, S Majidi and M. Taghiabadi, "Comparative study of on-line membrane electrode assembly activation procedures in proton exchange membrane fuel cell," *Fuel cells*, vol. 13, no. 5, pp. 946–955, 2013.
- [285] M. Uchimura and S. S. Kocha, "The impact of cycle profile on pemfc durability," *Ecs Transactions*, vol. 11, no. 1, p. 1215, 2007.
- [286] L. I. Astudillo and H. A. Gasteiger, "Degradation of Pt-Based Cathode Catalysts Upon Voltage Cycling in Single-Cell PEM Fuel Cells Under Air or N₂ at Different Relative Humidities," *Journal of The Electrochemical Society*, vol. 170, no. 12, p. 124 512, 2023.
- [287] G. Tsotridis, A. Pilenga, G. De Marco, T. Malkow *et al.*, "EU harmonised test protocols for PEMFC MEA testing in single cell configuration for automotive applications," *JRC Science for Policy report*, vol. 27632, 2015.
- [288] US DRIVE Fuel Cell TechTeam, "Appendix A: FCTT AST and polarization curve protocols for PEMFCs," *US Department of Energy*, 2013.
- [289] R. Mukundan *et al.*, "Vh 5 accelerated testing validation," *Target*, vol. 40, no. 12,600, pp. 22–200,
- [290] K. Akhtar, S. A. Khan, S. B. Khan and A. M. Asiri, "Scanning electron microscopy: Principle and applications in nanomaterials characterization," *Handbook of materials characterization*, pp. 113–145, 2018.
- [291] K. J. Mayrhofer, S. J. Ashton, J. C. Meier, G. K. Wiberg, M. Hanzlik and M. Arenz, "Non-destructive transmission electron microscopy study of catalyst degradation under electrochemical treatment," *Journal of Power Sources*, vol. 185, no. 2, pp. 734–739, 2008.
- [292] K. J. Mayrhofer *et al.*, "Fuel cell catalyst degradation on the nanoscale," *Electrochemistry Communications*, vol. 10, no. 8, pp. 1144–1147, 2008.
- [293] K. J. Mayrhofer, M. Hanzlik and M. Arenz, "The influence of electrochemical annealing in co saturated solution on the catalytic activity of pt nanoparticles," *Electrochimica acta*, vol. 54, no. 22, pp. 5018–5022, 2009.
- [294] K. Yu, C. Li, J. Xie and P. J. Ferreira, "Understanding the degradation mechanisms of pt electrocatalysts in pemfcs by combining 2d and 3d identical location tem," *Nano Letters*, vol. 23, no. 5, pp. 1858–1864, 2023.

- [295] Y. Yu *et al.*, “Three-dimensional tracking and visualization of hundreds of pt-co fuel cell nanocatalysts during electrochemical aging,” *Nano letters*, vol. 12, no. 9, pp. 4417–4423, 2012.
- [296] F. J. Perez-Alonso, C. F. Elkjær, S. S. Shim, B. L. Abrams, I. E. Stephens and I. Chorkendorff, “Identical locations transmission electron microscopy study of pt/c electrocatalyst degradation during oxygen reduction reaction,” *Journal of Power Sources*, vol. 196, no. 15, pp. 6085–6091, 2011.
- [297] J. C. Meier *et al.*, “Degradation mechanisms of pt/c fuel cell catalysts under simulated start–stop conditions,” *Acs Catalysis*, vol. 2, no. 5, pp. 832–843, 2012.
- [298] N. Hodnik *et al.*, “Severe accelerated degradation of pemfc platinum catalyst: A thin film il-sem study,” *Electrochemistry Communications*, vol. 30, pp. 75–78, 2013.
- [299] G. Jerkiewicz, G. Vatankhah, S.-i. Tanaka and J. Lessard, “Discovery of the potential of minimum mass for platinum electrodes,” *Langmuir*, vol. 27, no. 7, pp. 4220–4226, 2011.
- [300] S. Yu, X. Li, S. Liu, J. Hao, Z. Shao and B. Yi, “Study on hydrophobicity loss of the gas diffusion layer in PEMFCs by electrochemical oxidation,” *Rsc Advances*, vol. 4, no. 8, pp. 3852–3856, 2014.
- [301] X. Zhang, Y. Yang, L. Guo and H. Liu, “Effects of carbon corrosion on mass transfer losses in proton exchange membrane fuel cells,” *International journal of hydrogen energy*, vol. 42, no. 7, pp. 4699–4705, 2017.
- [302] D. Schonvogel *et al.*, “Stability of pt nanoparticles on alternative carbon supports for oxygen reduction reaction,” *Journal of the Electrochemical Society*, vol. 164, no. 9, F995, 2017.
- [303] Y. Kim *et al.*, “Highly durable fuel cell electrodes based on ionomers dispersed in glycerol,” *Physical Chemistry Chemical Physics*, vol. 16, no. 13, pp. 5927–5932, 2014.